UNIVERSITY OF
LIVERPOOL

Techniques of Efficient Power Transfer in Wireless Communication Systems

by

Yuan Zhuang

B.Eng.

A thesis submitted in accordance with the requirements for the award of
the degree of *Doctor of Philosophy* of the University of Liverpool

September 2018

I would like to dedicate this thesis to my loving girlfriend and my parents

Declaration

I hereby declare that except where specific reference is made to the work of others, the contents of this dissertation are original and have not been submitted in whole or in part for consideration for any other degree or qualification in this, or any other University. This dissertation is the result of my own work and includes nothing which is the outcome of work done in collaboration, except where specifically indicated in the text.

Yuan Zhuang

2018

Acknowledgements

First and foremost, I would like to express my deepest gratitude to my main supervisor Dr. Zhou Jiafeng for granting me the precious opportunity to test myself at the highest level. You have encouraged and helped me to grow up from a fresh graduate student to a professional researcher. I learned so much from you both academically and personally. Thank you for the invaluable comments and advice on my research as well as my life and career. It is a great honour for me to be one of your PhD students, and I hope I have repaid the faith you showed in me. Secondly, I would also like to thank my second supervisor Dr. Zhu Xu and Prof. Yi Huang, for the generous support and academic guidance you have provided to me. I will always treasure your support, encouragement and guidance.

I would also like to thank my parents, especially my mother. You have always supported me with no expectation of a reward. Your continuous help and understanding have made my life full of love and I am grateful for everything you have done. I would also like to express my appreciation to my girlfriend and colleague Chen Anqi. I would never have succeeded without her love, tolerance, support, encouragement and patience. This work is dedicated to you.

Special thanks are also paid to my brilliant and lovely colleagues and friends; in particular to Dr. Qian Xu, Dr. Lei Xing, Dr. Sheng Yuan, Dr. Saqer S. Alja'afreh, Dr. Muayad Kod, Dr. Chaoyun Song, Dr. Zhihao Tian, Dr. Zhouxiang Fei, Dr. Muaad Hussein, Dr. Abed Pour Sohrab, Anqi Chen, Yuan Zhuang, Manoj Stanley, Wenzhang Zhang, Chen Xu, Tianyuan Jia, Dr. Dajun Lei, Rui Pei, Zhenzhen Jiang, Jingchen Wang and Umniyyah Ulfa for many fruitful discussions and enjoyable moments. Particular thanks should also be paid to Mark Norman, John Owens, Gareth Blacoe and John Gillmore from the Electrical Workshop for always being very kind to me and fabricating my circuits very quickly and beautifully.

Last but not the least, the support from the Electrical Engineering and Electronics Department of the University of Liverpool is gratefully acknowledged.

Table of Contents

List of Figures

Acronyms

AC	Alternating Current
ADS	Advanced Design System
BPF	Band-Pass Filter
BW	Bandwidth
CAD	Computer Aided Design
CDMA	Code Division Multiple Access
CT	Current Transformer
CW	Continuous Wave
DA	Distributed Amplifier
DC	Direct Current
DE	Drain Efficiency
DPD	Digital Pre-Distortion
EH	Energy Harvesting
EM	Electromagnetic
EV	Electrical Vehicle
FBW	Fractional Bandwidth
FET	Field Effect Transistor
FSC	Flux-Shaping Capacitor
GaAs	Gallium Arsenide
GaN	Gallium Nitride

GNSS	Global Navigation Satellite System
GSM	Global System for Mobile communication
HEMT	High Electron Mobility Transistor
HSPA	High-Speed Packet Access
ID	Inner Diameter
IEEE	Institute of Electrical and Electronics Engineers
IMN	Input Matching Network
InP	Indium Phosphide
IPT	Inductive Power Transfer
IRC	Identical Resonant Coil
KCL	Kirchhoff's Current Law
KVL	Kirchhoff's Voltage Law
LM	Load Modulation
LMBA	Load Modulation Balanced Amplifier
LPF	Low-Pass Filter
LTE	Long Term Evolution
MC	Monte Carlo
MN	Matching Network
MIMO	Multiple Input Multiple Output
MRC	Magnetic Resonant Coupling
NIRC	Non-Identical Resonant Coil
OD	Outer Diameter
OFDM	Orthogonal Frequency-Division Multiplexing

OMN	Output Matching Network
PA	Power Amplifier
PAE	Power Added Efficiency
PCB	Printed Circuit Board
PSU	Power Supply Unit
PTE	Power Transfer Efficiency
RF	Radio Frequency
RMS	Root Mean Square
Rx	Receiver
SMD	Surface-Mount Device
SPICE	Simulation Program with Integrated Circuit Emphasis
SROM	Stochastic Reduced Order Model
TBW	Transition Bandwidth
TDMA	Time-Division Multiple Access
TPN	Two Port Network
TWA	Transfer Window Alignment
TX	Transmitter
VNA	Vector Network Analyser
VSWR	Voltage Standing Wave Ratio
WiMAX	Worldwide Interoperability for Microwave Access
WPT	Wireless Power Transfer

List of Publications

First Author Publications

[1] **Y. Zhuang**, Zhouxiang. Fei, Anqi. Chen, Yi. Huang, K. Rabbi and Jiafeng. Zhou, "Design of multiovtave high-efficiency power amplifier using stochastic reduced order models,", *IEEE Transactions on Microwave Theory and Techniques*., vol. 66, No.2, pp.1015-1023, Feb, 2018.

[2] **Y. Zhuang,** C. Xu, C. Song, A. Chen, W. Lee, Y. Huang and J. Zhou, "A novel method of improving current transformer-based energy extraction from AC power lines under magnetic saturation," *IEEE Transactions on Industrial Electronics*, 2018 (under review).

[3] **Y. Zhuang,** A. Chen, C. Xu, C. Song, Y. Huang and J. Zhou, "Range-adaptive high efficiency wireless power transfer using multiple bi-directional sub-coils Transmitter," *Nature Scientific Reports*, 2018 (submitting).

[4] **Y. Zhuang,** J. Zhou, Y. Huang and A. Chen, "Design of a broadband high efficiency GaN power amplifier for GNSS applications," *IEEE MTT-S International Wireless Symposium,* Shanghai, China, 2016.

[5] **Y. Zhuang**, J. Zhou, Y. Huang, R. Rayit and R. Khondker, "Design of Ultra broadband highly efficient GaN power amplifier with Voronoi Diagram," *Automated RF & Microwave Measurement Society Conference*, Oxford, April, 2017.

[6] **Y. Zhuang**, C. Xu, S. Yuan, C. He, J. Zhou, Y. Huang, A. Chen and W. W. Lee, "Design of an Energy Harvesting System on Power Transmission Lines," *IEEE MTT-S Wireless Power Transfer Conference*, Taipei, Taiwan, May, 2017.

[7] **Y. Zhuang,** C. Xu, S. Yuan, C. He, A. Chen, W. Lee, Y. Huang and J. Zhou, "An improved energy harvesting system on power transmission lines," *IEEE Wireless Power Transfer Conference*, June, 2017.

[8] **Y. Zhuang,** C. Xu, C. Song, A. Chen, W. Lee, Y. Huang and J. Zhou, "Using control coil to improve magnetic energy extraction from AC power line under magnetic saturation," *Asian Wireless Power Transfer Workshop*. Dec, 2017.

[9] **Y. Zhuang,** C. Xu, A. Chen, W. Lee, Y. Huang and J. Zhou, "Distributed Matching Network design for broadband power amplifiers," *IEEE Electrical Design of Advanced Packaging and System Symposium*, Dec, 2017. (**Best Paper**)

[10] **Y. Zhuang**, A. Chen, C. Xu, Y. Huang and J. Zhou, "Wireless power transfer system with constant inductive coupling over a wide range of distances," *Progress in Electromagnetics Research Symposium*, Toyama, Japan, Aug. 2018. (**invited talk**)

[11] **Y. Zhuang**, A. Chen, C. Xu, Y. Huang and J. Zhou, "Range-adaptive wireless power transfer system using multi-antiparallel loops," *IEEE Asian Pacific Conference on Antenna Propagation*, Auckland, New Zealand, Aug, 2018. (**Best Student Paper First Prize**)

Co-author Publications

[12] A. Chen, **Y. Zhuang**, J. Zhou, Y. Huang and L. Xing, "Design of a broadband Wilkinson power divider with wide range tuanable bandwidths by adding a pair of capacitors," *IEEE Transactions on Circuit and Systems II: Briefs* (early access), DOI: 10.1109/TCSII.2018.2803076, Feb, 2018.

[13] A. Chen, **Y. Zhuang**, Yi. Huang and J. Zhou, "A horst-type power divider with wide frequency tuning range using varactors," *IEEE Transactions on Circuit and Systems I: Regular Papers*, Sep, 2018 (submitted).

[14] Q. Xu, Y, Huang, L. Xing, Z. Tian, J. Zhou, A. Chen and **Y. Zhuang**, "Average Absorption Coefficient Measurement of Arbitrarily Shaped Electrically Large Objects in a Reverberation Chamer," *IEEE Transactions on Electromagnetic Compatibility*, vol. 58, No.6, pp. 1776-1779, doi. 10.1109/TEMC.2016.2587679, 2016.

[15] Song, A. Lopez, Y. Huang, D. Segovia, **Y. Zhuang**, Y. Wang and J. Zhou, "Novel quartz clock with integrated wireless energy harvesting and sensing functions," *IEEE Transactions on Industrial Electronics*, 2018.

[16] Chen, A. B. Mousa, **Y. Zhuang**, Y. Huang and J. Zhou, "Compact Ka-band substrate-integrated waveguide filter with spurlines for satellite communication systems," *2016 IEEE 9th UK-Europe-China Workshop on Millimetre Waves and Terahertz Technologies (UCMMT)*, Qingdao, China, 2017.

[17] K. Rabbi, J. Zhou, Y. Huang, **Y. Zhuang**, E. McEwan, A. Rayit and R. Rayit, "Highly efficiently wideband harmonic-tuned power amplifier using low-pass matching network,"*47th European Microwave Conference*, Sep 2017.

[18] C. Xu, **Y. Zhuang**, W. Lee, Y. Huang and J. Zhou, "High efficiency wireless power transfer system robust against misalignment," *IEEE MTT-S International Symposium on Electromagnetic Compatibility and 2018 IEEE Asia-Pacific Symposium on Electromagnetic Compatibility, EMC/APEMC, Singapore*, Jun, 2018.

[19] C. Xu, **Y. Zhuang**, H. Han. C. Song, Y. Huang and J. Zhou, "Multi-coil high efficiency wireless power transfer system against misalignment," *IEEE MTT-S International Wireless Symposium*, *IWS 2018-Proceedings*, Jun, 2018.

[20] W. Zhang, **Y. Zhuang**, C. Song, Y. Huang and J. Zhou, "A dual band quasi-yagi wearable antenna with high directivity," *IEEE MTT-S International Wireless Symposium*, *IWS 2018-Proceedings*. Jun, 2018.

Award

Best Symposium Paper, IEEE Electrical Design of Advanced Packaging and System Symposium, Dec, 2017.

Best Student Paper First Prize, IEEE Asian Pacific Conference on Antenna Propagation, Aug, 2018.

Reviewer

IEEE Transaction on Industrial Electronics

IEEE Transactions on Microwave Theory and Techniques

Abstract

Efficient power transfer in wireless communication system is engineering the electronic signal propagation path to maximize the transfer power and efficiency to the load or minimize the signal reflection from the load. The modern wireless communication systems require not only reliable signal and power transmission but also high-efficiency propagation as well for both the cost-effective and environmental friendly purpose. The purpose of this thesis is to conduct a comprehensive research into the efficient power transfer of systems. The main contributions of this thesis are laid in three areas: The first area focuses on improving the efficiency of a power amplifier (PA) over an ultra-wide bandwidth. Two designs are presented in this part. In the first design, an optimal impedance contour is designed considering both frequency band and desired output power rather than an optimal impedance point of the traditional method. The second design presents a novel general design method of frequency varying impedance matching using stochastic reduced order models and Voronoi partition. The performance of the presented PAs outperforms existing PAs which demonstrates the excellence of the proposed method. The second area focusses on the impedance variation caused by the magnetic saturation in the magnetic energy harvesting of an AC power line. This design introduces a novel artificial magnetic field to manipulate the dominant magnetic field of power lines to compress the saturation for higher harvested power. The last area concentrates on improving the transfer efficiency of the wireless power transfer system operating in various transfer positions. The impedance matching problem of a WPT systems is usually caused by the misalignment of the transmitter and receiver both vertically and horizontally which alternating the mutual inductance between coils. This part will solve the problem by compress the impedance variations rather than matching the various optimal impedance for different transfer position using differential coupling method.

This thesis has successfully demonstrated several novel design methods and techniques for efficient power transfer in wireless communication systems. The most challenging issues such as the nonlinear effect and low conversion efficiency have been significantly overcome by using these presented technologies. The research and knowledge in this thesis should be of great significance to the future development and have increased the boundary of this topic to a new level.

Chapter 1 **Introduction**

1.1 Motivation

With the rapid development of the modern wireless communication technologies, we are getting more and more dependent on wireless devices on the daily life (see Fig. 1-1). Wireless communication techniques change people's life. We can receive news from any corner of the earth every second, live chat with anyone you want to and charge your devices wirelessly. However, our world has been facing a series of major energy-related challenging issues such as the incredibly high demand of energy-related accessories. Barack Obama, the former president of the United of States discussed the climate change, weather patterns disruption, and ocean acidification of our world caused by a continued and expanded industrialization as well as a seemingly endless emission of carbon dioxide (CO_2) and other greenhouse gases. This thesis is aiming to develop new technologies that enable the highly efficient operation of our electronic devices and reduce the unnecessary power consumptions, contributing to the global environment protection.

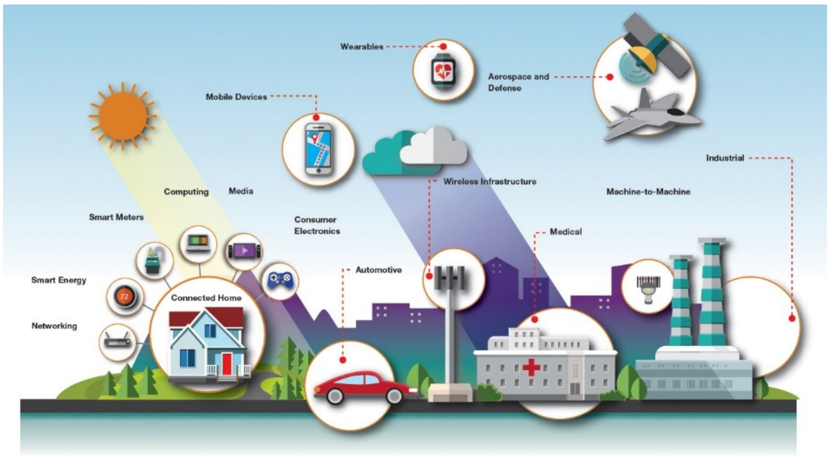

Fig. 1-1. Wireless communication linked world.

In a wireless communication system, the main power consumption occurred in power amplification stage and signal propagating procedure. Firstly, the power amplifiers (PA) are core components in communication systems. Half of the electricity consumption [1] by the world's mobile networks could be saved by enhancing the efficiency of PA-related components in the networks. On the other hand, efficient PA is environment-friendly. It is reported that by applying efficient PA globally, it would reduce carbon emissions by 36 million tons each year, which is equivalent to the number of 7 million cars' emissions. Thus, developing techniques to improve the power amplification efficiency will contribute to the green wireless communication systems [2].

From a wireless communication device designer's point of view, one important key to improve the energy usage efficiency is impedance matching. A typical wireless communication device can be modelled as a two-port network as shown in Fig. 1-2:

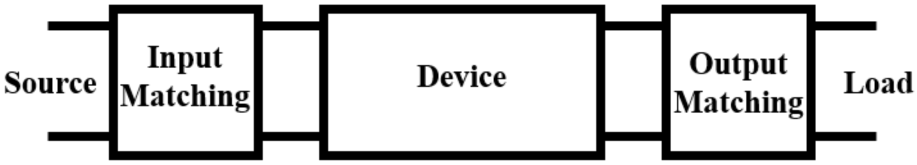

Fig. 1-2. General two-port network with matching units.

The input and output matching networks should conjugately match the impedance of the device to the source and load respectively to achieve the maximum power transfer. Whenever a source with a fixed output impedance such as an electric signal source, a radio transmitter or a mechanical sound (e.g., a loudspeaker) operates into a load, the maximum possible power is delivered to the load when the impedance of the load is equal to the complex conjugate of the impedance of the source (that is, its internal impedance or output impedance). For two impedances to be complex conjugates their resistances must be equal, and their reactance must be equal in magnitude but of opposite signs. In low-frequency or DC systems (or systems with purely resistive sources and loads) the reactance is zero, or small enough to be ignored. In this case, maximum power transfer occurs when the resistance of the load is equal to the resistance of the source. However, in the wireless communication systems, the device will not always have a constant impedance, which will usually vary with parameters such as frequency, conducted power level (for PAs or diodes), transfer position or coupling conditions (for WPT devices) and magnetic or electric field strength (for EH devices). Therefore, the devices' impedance variation will introduce a challenge of impedance matching in realising efficient PAs.

The target of this work is to overcome the variable impedance matching challenges and problems, especially in the following aspects:

i. To develop an **Radio Frequency (RF) PA that can operate in a multi-octave bandwidth** with high output power, stable power gain and high efficiency. The input and output matching networks of the PA should be able to maintain vert good matching condition passively regardless the impedance variation caused by nonlinear effects of the transistor, in terms of frequency sweeping, output power level change, to keep the PA operating with a high-efficiency feature.
ii. To develop **a range-adaptive magnetic resonant coupling wireless power transfer system (MRC-WPT)** that can transfer the desired power level with desired high efficiency in a large adaptive position range. The transmitter and receiver of the system should be able to provide a relatively smooth mutual inductance passively regardless of the transfer position in terms of transfer height and horizontal misalignment.
iii. To develop **a magnetic energy harvester for AC power transmission lines** which can deliver high power with the existence of the magnetic core saturation. The matching network of the energy harvester should be able to manipulate the dominant magnetic field of an AC power line to an optimal level to mitigate the magnetic core saturation phenomenon, achieving a high output power.

1.2 Dissertation Outline

This work focusses on solving variable impedance matching problems in wireless communications systems especially in RF PA, MRC-WPT, and magnetic energy harvesting (EH). The dissertation consists of seven chapters and the structure is organized as follows:

Chapter 1 introduces the main challenges to be solved for this study, and the background of this work including the motivation and objectives of the research.

Chapter 2 reviews the state-of-the-art variable impedance matching techniques in several specific device designs including broadband high-efficiency PAs. Reported methods of adaptive matching with impedance variation and techniques of constrained impedance matching are discussed in detail.

Chapter 3 discusses the methodology to design wideband PAs using an optimal impedance contour covering the required impedance over a wide bandwidth. The variation of the optimal impedances is limited by setting a contour containing the impedances leading to high efficiency for different frequencies. A bandpass matching network is adapted to realize both input and output matching networks to present the transistor proper impedances. The fabricated PA demonstrates a high-efficiency and high output power over a broad frequency band.

Chapter 4 introduces a PA design methodology that dealing with optimal impedance varying over a multi-octave frequency range. In this case, the variation cannot be constrained without major performance trade-off. Thus, the proposed method using a statistic analysis-based algorithm to design matching networks that can adaptively match the variable impedances for the PA. A detailed procedure is presented including defining optimal impedance contours and matching network synthesis. The realized PA demonstrates state-of-the-art performance in terms of efficiency, in-band gain flatness and output power level.

Chapter 5 focuses on matching impedances that variate in the time-domain caused by magnetic core saturation in EH devices. The novel method used in this work constrains the variation of the impedance by manipulating the dominant magnetic field that saturates the core. The realized system demonstrates the highest harvested power compared to other reported works in the literature. A completely self-sustainable EH system was realized. The experimental results validate the contribution of the novel impedance constraining method for improving the harvested power.

Chapter 6 solves the impedance matching problem caused by the variation of the transfer position in a WPT system. Conventional designs match the source and load based on a certain transfer position or distance to achieve high efficiency. Once the optimal position cannot be maintained, the input impedance will change leading to mismatch and degrading the transfer efficiency. This work proposes a novel structure using bi-directional resonant coils to maintain a relatively constant impedance regardless of the transfer position within a large region. Therefore, the variation of impedance is significantly reduced, and a range-adaptive WPT can be achieved.

Chapter 7. draws a summary of the main contributions of this dissertation. Future works of this research are suggested.

1.3 References

[1] C. Han, T. Harrold, S. Armour, "Green radio: Radio techniques to enable energy-efficient wireless network," *IEEE Communication Magazine*, vol. 46, pp. 46-54.

[2] J. M. Golio, ‘RF and microwave circuits, measurements, and modelling,’ CRC, Boca Raton,London, 2008.

Chapter 2 **Review of Efficient Broadband Power Amplifiers**

In the past few decades, wireless communication technology was undergoing a veritable explosion of growth, reforming people's daily life in business, education, health and everywhere. Power amplifiers (PA) are the last amplification stage in the transmitting chain of wireless communication systems, whose job is to produce enough output power of the signal for an antenna. The PA is a crucial component since its performance have substantial effects on the overall system features regarding bandwidth, efficiency and output power of the transmitter [1].

PAs are core components in communication systems. Half of the electricity consumption by the world's mobile networks could be saved by enhancing the efficiency of the PA related components in the networks [2]. On the other hand, an efficient PA is environment-friendly. By applying efficient PAs globally, it would reduce carbon emissions by 36 million tons each year, which is equivalent to that of 7 million cars [3].

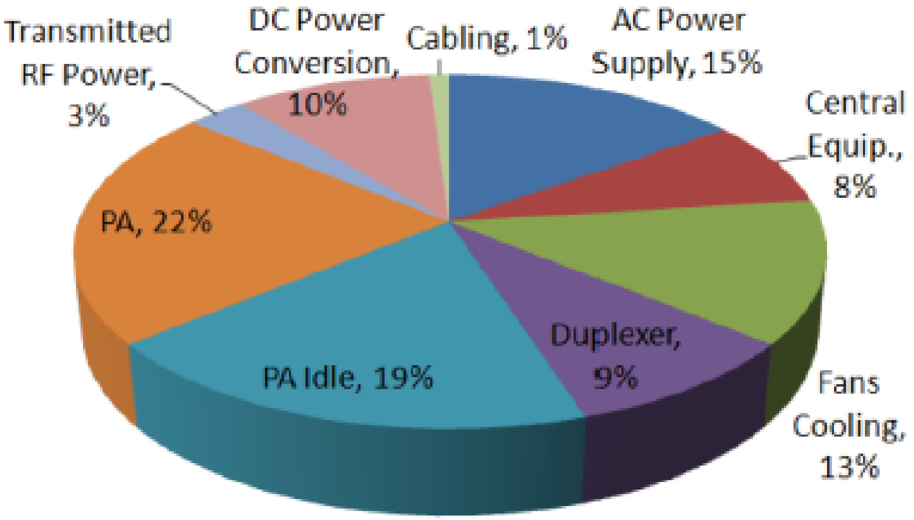

Fig. 2-1. Energy consumption in a typical base station [1].

In a highly efficient PA, increases in efficiency which at first might appear to be minor can be essential. For example, an increase of drain efficiency from 80% to 90% will halve the drain power dissipation from 20% to 10%. This will result in a reduction in the heat sink volume and weight by a factor of 2.8 [2]. Alternatively, it will halve the junction temperature rise and therefore decrease the transistor failure rate, contributing to extending the working life of the device.

On the other hand, the ever-increasing number of frequency bands and spectrum fragmentation demand wireless communication systems have broadband features. The modern wireless communication system is evolving and involves a multiplicity of communication standards such as high-speed packet access (HSPA), long-term evolution (LTE) and worldwide interoperability for microwave access (WiMAX). These standards require communication systems operating at different centre frequencies, with different bandwidths and modulation schemes [3]. Wireless service providers have to offer a large number of radios for these standards resulting in a costly network infrastructure.

Driven by the demands of consumers for wireless portable devices, the industry and academia have responded and offered improved services and standards. For example, the first generation named 1G cellular was introduced in the early 80s, based on analogue networks operated at 900MHz. Then, the 2G cellular system was announced ten years later, which provided much-improved data rate. Till now, the 4G system using OFDM technology is operated around the world offering high quality and enhanced functionality services. Nowadays, the idea of 5G networks has been proposed, which is designed to deliver higher data rate services, and it will demand broader bandwidth and higher efficiency with lower cost and smaller size devices. Therefore, the aims and objectives of the first research area of this thesis are:

- To improve the efficiency of RF PAs
- To extend the operational bandwidth of RF PAs
- To propose novel design methods of wideband high-efficiency PAs

2.1 PA Classification

The PAs can be categorized into several operating classes based on the voltage and current waveforms. Conventionally, these classes can be classified into two modes named current mode and transconductance mode PAs. PAs can be operated as a controlled current source by the DC gate voltage or in a switching mode in which case the transistor will behave like an on/off switch. Different classes PAs will have different efficiencies. To evaluate the efficiency of a PA, the time domain voltage and current waveforms on the drain of a transistor can be represented by:

$$v(t) = V_P \sin(\omega t) + V_{DC} \tag{2.1}$$

$$i(t) = I_P \sin(\omega t + \varphi) + I_{DC} \tag{2.2}$$

where V_P and I_P are the magnitudes of the AC voltage and current, V_{DC} and I_{DC} are the amplitude offset of the DC voltage and current, and φ is the phase offset. Then the power dissipated by the transistor, delivered to the load and the power provided by the DC source can be calculated as:

$$P_{Dissipated} = \frac{1}{T}\int_0^T v(t) * i(t)dt \tag{2.3}$$

$$P_{Delivered} = \frac{1}{T}\int_0^T [v(t) - V_{DC}] * [i(t) - I_{DC}]dt \tag{2.4}$$

$$P_{DC} = V_{DC} I_{DC} \tag{2.5}$$

To evaluate the performance of a PA converting DC power to RF power, the efficiency of a PA is an important feature. Conventionally, the efficiency of a PA can be calculated in two ways, namely, drain efficiency (DE) and power added efficiency (PAE). DE is a measure of how much DC power is converted to RF power at the terminal where the DC power is supplied. The DE is usually used for high gain devices due to the incident RF power that goes into the device is not taken into consideration. Therefore, the drain efficiency of the PA can be represented by:

$$\eta = \frac{P_{Delivered}}{P_{DC}} \tag{2.6}$$

Usually, for RF PA designs, the power gain is relatively low around 10 – 20 dB. Therefore, the input RF power should be considered to calculate the efficiency of a PA. PAE is similar to DE, however it takes into account the RF power added to the device. Hence, the PAE is used to evaluate the PA performance as:

$$PAE = \frac{P_{Delivered} - P_{RF,in}}{P_{DC}} \tag{2.7}$$

2.1.1 Current Mode PAs

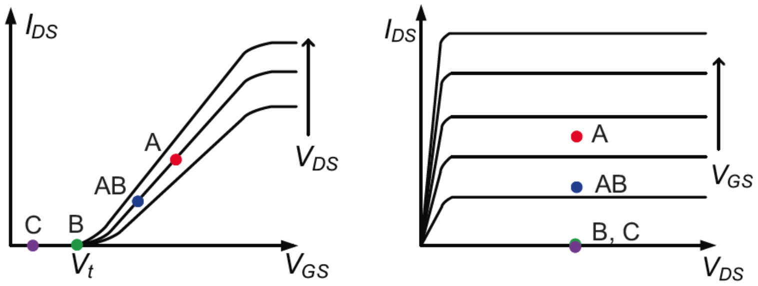

Fig. 2-2. The DC bias conditions for the current mode PAs.

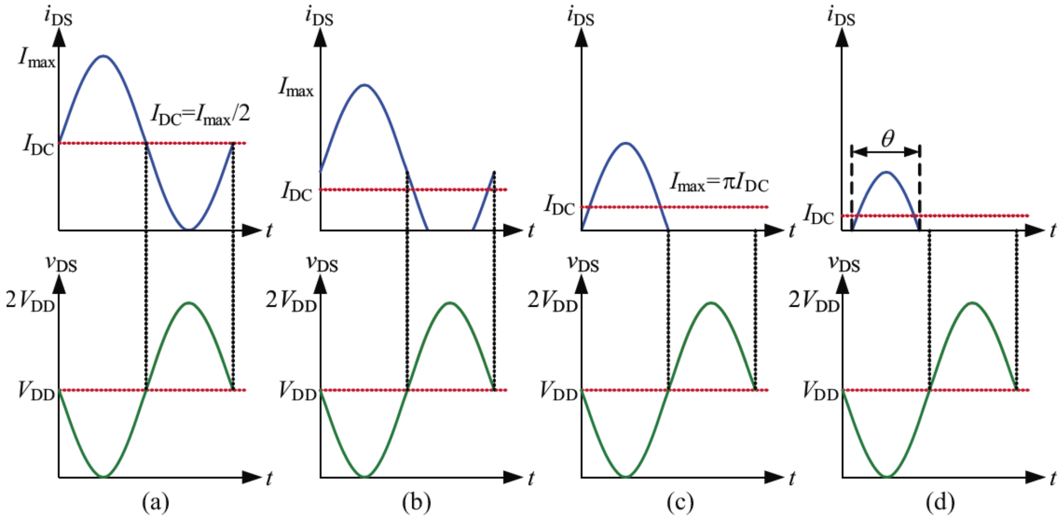

Fig. 2-3. Typical drain waveforms of the current mode PAs (a) Class-A, (b) Class-AB, (c) Class-B, (d) Class-C.

For current mode PAs, the most important parameter is the DC bias condition. The DC bias conditions for different classes of current mode PAs are illustrated in Fig. 2-2. The typical drain waveforms of the current mode PAs are shown in Fig. 2-3. A PA operates in Class-A is biased at the middle of the load line between the saturation and pinch-off point. It will have a 360° conduction angle due to the transistor is turned on by the DC bias. The typical voltage and current waveforms of a Class-A PA are shown in Fig. 2-3(a). Due to the large overlap area of the current and voltage waveform, at least half of the DC power is consumed by the transistor, resulting in a maximum efficiency of 50% for the ideal case. Because the transistor is turned on by the DC bias, both positive and negative excursions deliver power. The PA will have a 360° conduction angle, achieving a high gain and very little harmonics. Therefore, Class-A PAs are desired for applications require high linearity and high gain. Herein, if a higher efficiency is desired, the DC bias current can be reduced to decrease the voltage and current overlap.

A Class-AB PA is biased between the pinch-off point and middle of the load line. Typical voltage and current waveforms of a Class-AB PA are shown in Fig. 2-3(b). As the magnitude of the current is reduced, the power dissipated by the transistor can be decreased accordingly. The efficiency of a Class-AB PA can be 50% - 78.5%. However, for *t* from 0.1 – 0.4, the transistor will not be conducting. The conducting angle is sacrificed for higher efficiency. If the quiescent current is further reduced to zero, the PA will be operating at Class-B mode. Typical voltage and current waveforms of a Class-B PA are shown in Fig. 2-3(c).

Class-B PA provides a linear amplification due to that the amplitude of the drain current increases proportionally with a fixed half sinusoidal signal to the amplitude of the input driver [8]. The theoretical efficiency of Class-B is improved to 78.5% compared with Class-A, with a sacrifice of conducting angle and gain.

Class-C PAs are biased in a portion that is less than half of the RF cycle. The typical waveforms of the Class-C PA are shown in Fig. 2-4:

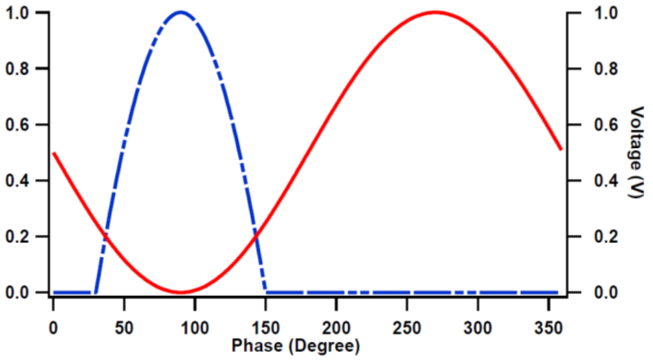

Fig. 2-4. Typical voltage and current waveforms of a Class-C PA.

The following figures illustrate the different bias conditions of the Classes above and the typical drain voltage waveforms:

For the Class-B PA, if the impedance at the odd harmonics is tuned to be an open circuit, and the impedance at the even harmonics tuned to be a short circuit as shown in Fig. 2-5:

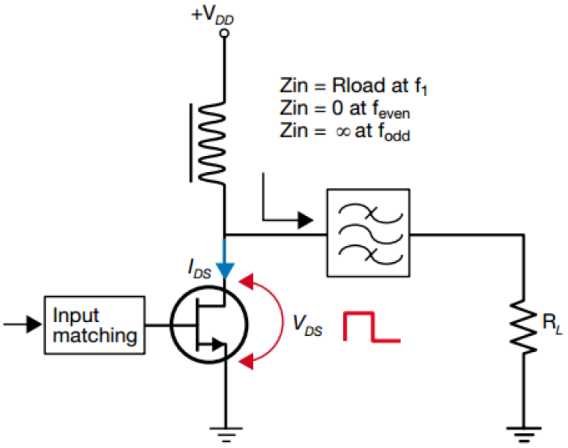

Fig. 2-5. The ideal structure of a Class-F PA.

Now Class-B is converted to be Class-F where the waveform is transformed into a square wave by terminating the odd harmonics open, and the even harmonics shorted [4]. For an ideal Class-F PA, the drain voltage is a square wave, and the current is a half-sinusoidal [5]. In reality, a portion of the RF cycle will be driven into the saturation region to satisfy the requirement of a square voltage waveform. Based on the Trigonometric Fourier Series, the periodic signal can be expressed as a sum of sinusoids [6], the perfect square waveform can be achieved by using infinite harmonics. However, it is not possible in practice since the circuit will be complicated. The waveforms in Fig. 2-6 are constructed only using the third harmonic:

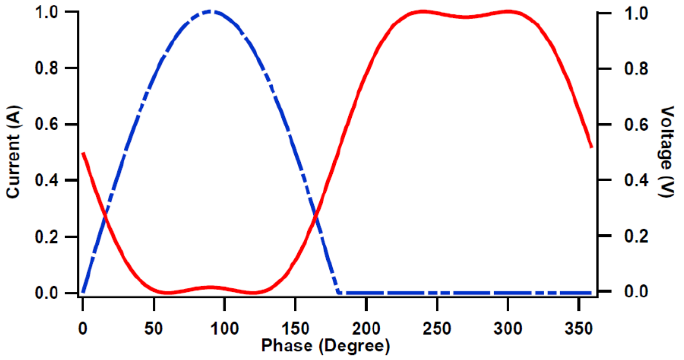

Fig. 2-6. Typical voltage and the current waveforms of a Class-F PA.

Once the voltage waveform is a perfect square wave, the overlap of the current and voltage on the transistor will be zero, leading a 100% efficiency [7]. The main obstacle to the Class-F design is the realisation of harmonic terminations at high frequencies. Hence, it is a trade-off between the complexity of the circuit and the required performance of the device [8].

2.1.2 Switching Mode PAs

For switching mode PAs, the transistors will only work in the saturation region. The voltage and current are determined by the output network rather than the input drive, different from the current mode PAs. Switching mode PAs such as Class-D and Class-E utilise the transistor as a switch that either the current passing through the transistor or the voltage across the device [9].

The Class-D PAs are categorised into two modes, namely, voltage mode Class-D with serial resonator circuits and current mode Class-D with parallel resonator circuits. Each type of Class-D has a topology with two resonators. The typical architectures and waveforms of the are shown in Fig. 2-7:

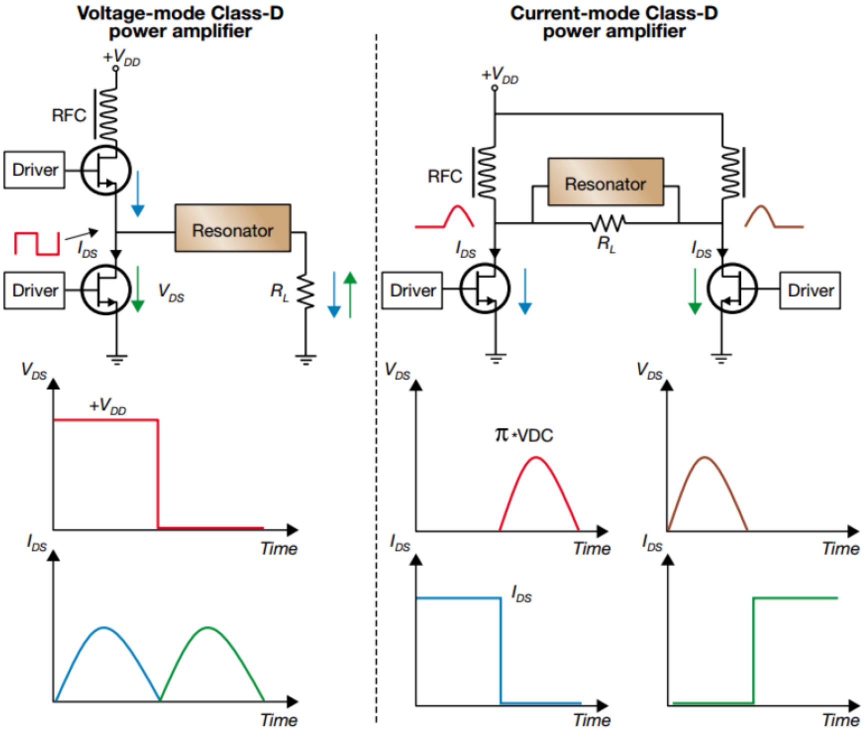

Fig. 2-7. Typical architectures and voltage and current waveforms of the Class-D PAs [10].

The left shows a typical voltage mode Class-D PA, where the voltage is a square waveform. The output resonator forms the current to be sinusoidal. This type of PA makes a high-efficiency solution for audio applications. However, voltage mode Class-D is not proper for the gigahertz frequency range due to the transistor output capacitance will become majority loss factor at the high-frequency band. The right shows a typical current mode Class-D PA, where the current is a square waveform. The output resonator makes the voltage to be a pure sine wave. The topology of a current mode Class-D PA is balanced where both the transistors are grounded, and the output capacitors can be utilised in the output filter. Therefore, the current mode Class-D PA will achieve a high efficiency in the gigahertz range [10].

As opposed to the conventional classes PAs, switching mode PAs use a transistor as like an on/off switch. So, when the switch is closed, the current flows into the switch, and when the switch is open, the current flows into the load which causes the voltage as shown in Fig. 2-8:

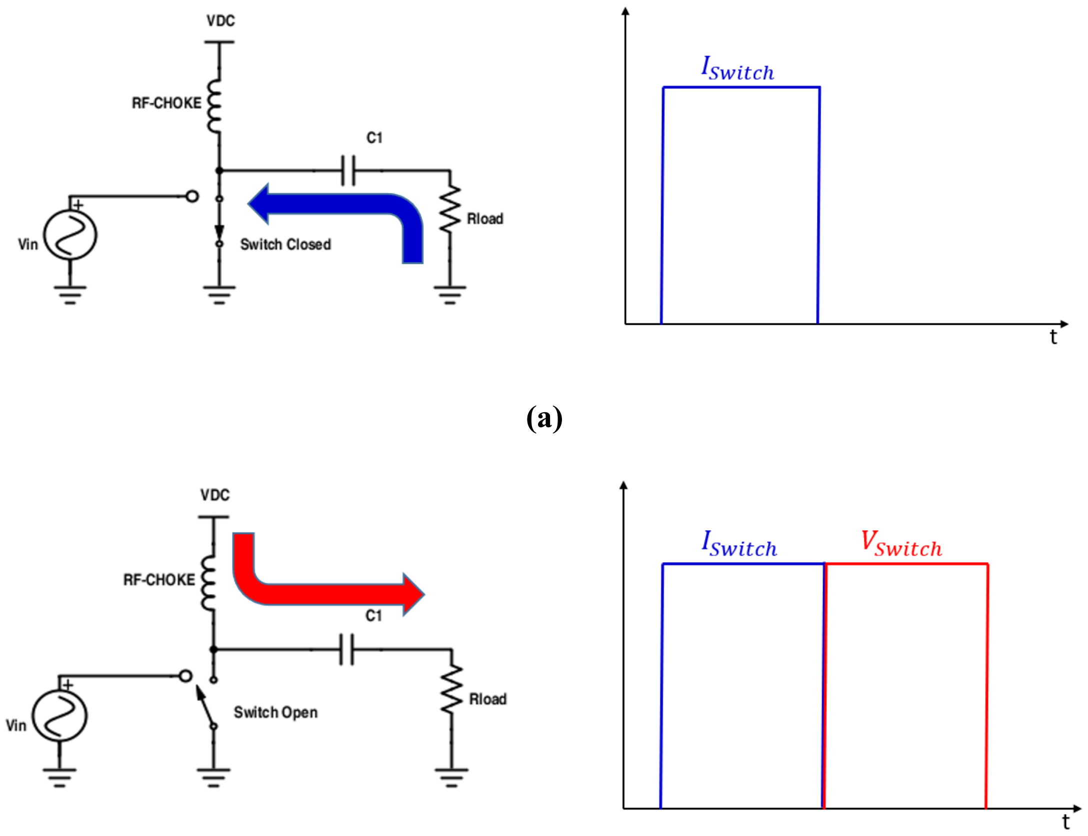

(a)

(b)

Fig. 2-8. Switching mode PAs operating waveform, (a) switch closed, (b) switch open.

Ideally, this will result in square voltage and current waveforms with almost no overlap. Hence, almost no power will be dissipated by the transistor, yielding a maximum drain efficiency. To control the harmonics, a resonator can be added into the output of the transistor. The circuit will be shorted at the fundamental and open at all the harmonics. So, the action of opening and closing the switch will force the sinusoidal current flow through the circuit. When the switch is closed, the current will flow out of the resonator into the switch as shown in Fig. 2-9:

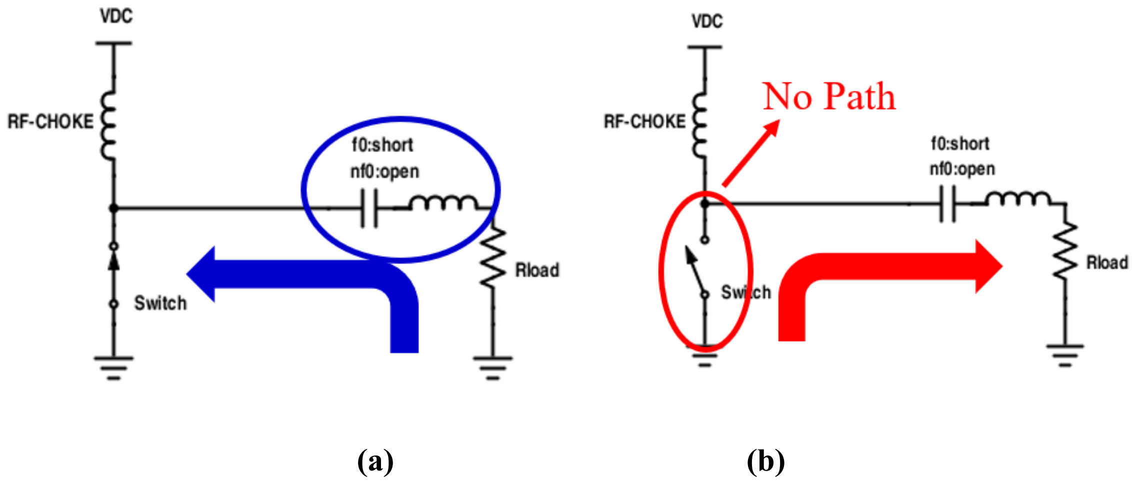

Fig. 2-9. Switching mode PAs operation (a) switch closed, (b) switch open.

However, when the switch is open, the resonator will try to pull back the current from the switch to form a sinewave, but there is no path for the current to return as the switch is an open circuit. Hence, a capacitor can be added into the circuit to form a return path for the current to the resonator as shown in Fig. 2-10:

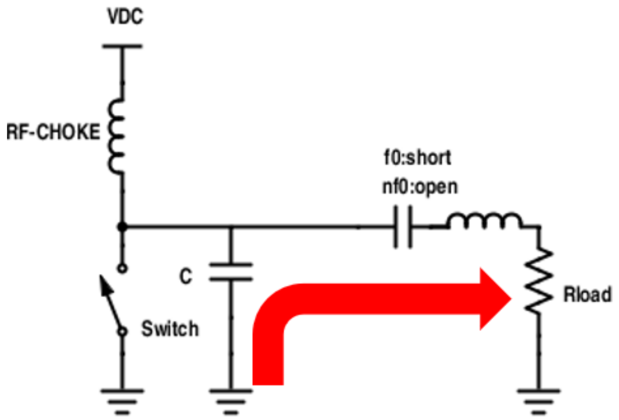

Fig. 2-10. Switching mode current path with a parallel capacitor.

The idea of achieving the highest efficiency of the PA is to avoid the current and voltage exists at the transistor at the same time. Although with a parallel capacitor, the current will flow back to the resonator when the switch is open, the current waveform of the switch closing time will have a DC offset as shown in Fig. 2-11:

Fig. 2-11. A switching mode current waveform with a parallel capacitor.

Therefore, to reduce the power dissipated on the transistor, the current can be delayed by a series-connected inductor and then the structure will form a typical Class-E PA. The structure, operating principle and waveform are shown as in Fig. 2-12:

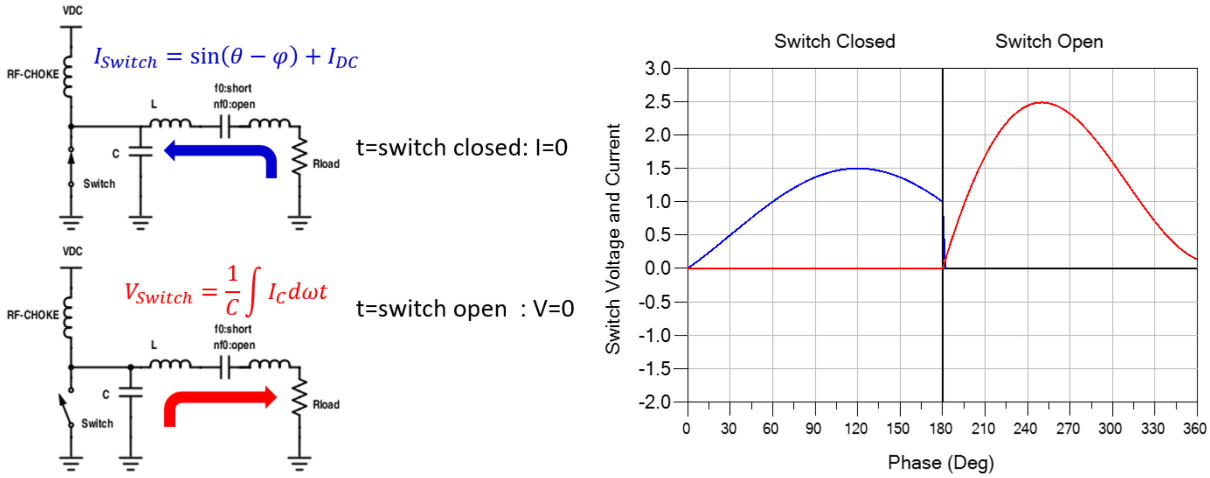

Fig. 2-12. Typical structure and waveforms of a Class-E PA.

2.2 Overview of Efficient Broadband PA Matching Techniques

Broadband high-power and high-efficiency PAs are very important for modern wireless communication systems to achieve low-cost and reliable features. However, the conventional methods to achieve high-efficiency performance such as Class-D [11], [12], Class-E [13] – [19], Class-F [20] – [24] and Doherty structure [25] – [29] need a high saturation level of the transistor. Nevertheless, the accurate harmonics control will also be demanded. These requirements need the input/output matching network (IMN/OMN) of the PAs provide the precise impedances to the transistor at the desired frequencies and power levels [9]. But the transistors are non-linear devices which will require different optimal impedances at different frequencies and power levels. Therefore, the broadband feature is difficult to maintain with the high-power and high-efficiency performance [10]. Herein, the primary challenge to realize an efficient broadband PA is assigning the optimal impedances at the desired frequencies with the required power level. Some popular solutions to extend the operating frequency band of the PAs are introduced below.

Distributed PA

William. S. Percival formulated the first distributed amplifier (DA) in 1936 using vacuum tube technology [30]. Recently, the GaAs, GaN and InP have been applied to the semiconductor technology [31] – [33]. The DA architecture introduces delay lines to achieve the broadband characteristics. For a DA the input is fed in series into the transistors and parallel out of them. A delay line combines the outputs. An example of the DA using GaN technology is shown in Fig. 2-13 [34]:

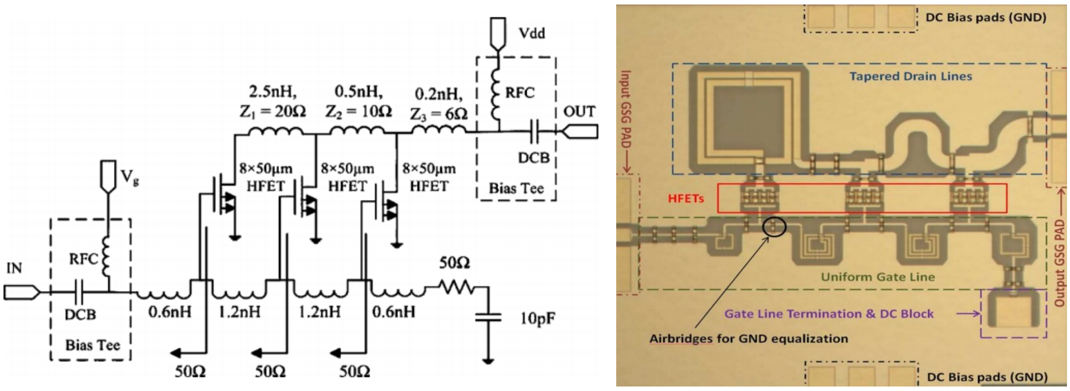

Fig. 2-13. An example of DA using GaN technology [34].

Although the DA structure will significantly improve the operating bandwidth, there exist several limitations in realising the high-efficiency performance. Each transistor used in the DA will contribute an unequal output power, which means some of the devices may not be working in the high-efficiency mode. On the other hand, the optimal impedance for each transistor may not be identical. Moreover, this structure needs multiple devices which will introduce more losses for the system and increase the circuit size. Overall, the DA structure is more suitable for broadband applications rather than the high-efficiency PA designs.

Load Modulation

As discussed before, due to the non-linearity of the transistors, the optimal impedances should be presented to the transistor for different operating frequencies and power levels to achieve the high-efficiency and high-power performance. Load modulation (LM) technique will provide the transistor with the optimal impedance yielding the maximum efficiency by alternating the effective load impedance both resistively and reactively [35]. Under the LM scheme, the drain voltage of the transistor will be kept at the same level for all different output powers by alternating the output current only. For high-efficiency switch mode amplifiers which work in the saturation or pinch-off condition, the above statement will be significant since it is the hard switching that gives the high efficiency. To reach fast switching with the very high power and bandwidth necessary for modern RF PAs, tunable elements or varactors with high power capability and good tunability are needed [7].

D. J. Shepphard *et al.* presented a load modulated balanced PA (LMBA) which can modulate the impedance seen by a pair of RF power transistors in a quadrature balanced configuration via varying the amplitude and phase with an external control signal [36]. The LMBA schematic and a fabricated demonstration broad are shown in Fig. 2-14:

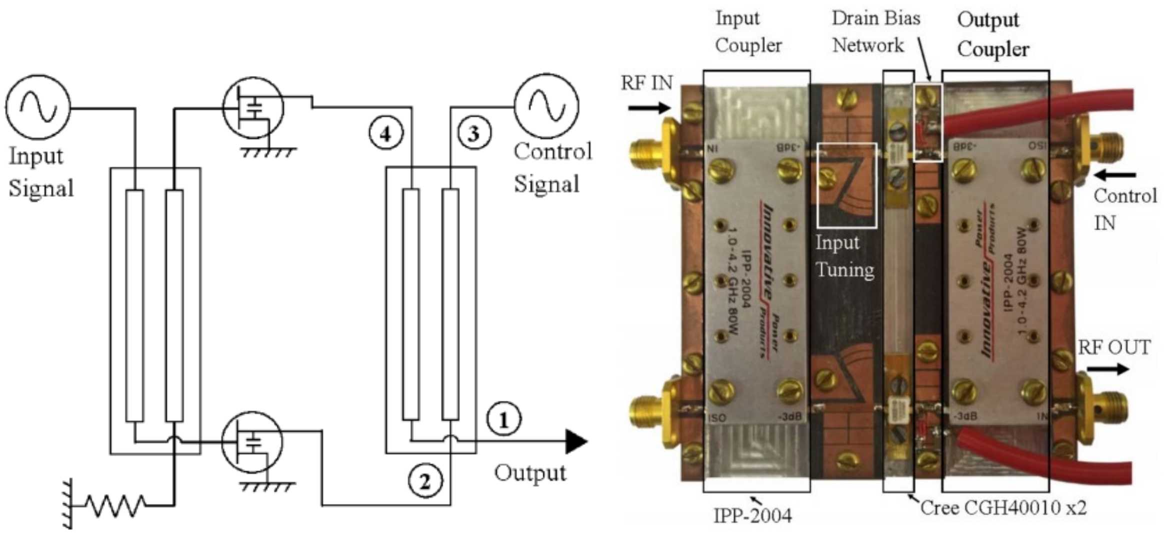

Fig. 2-14. The schematic and fabricated demo broad of LMBA [36].

This method will dynamically optimise frequency, efficiency and power performance by adjusting the externally applied control signal [37]. The control signal can modulate the impedance presented to the balanced transistors, both in magnitude and phase. Therefore, the function of the conventional passive matching networks can be complemented, or even replaced, by using dynamic adjustments to the external control signal. The control signal power is shown theoretically to add directly to the output power, regardless of its phase setting. In practice, this power conservation may be imperfect but is substantially realized under most conditions of control signal settings. The measured results show an efficiency better than 70% over an octave bandwidth from 0.8 GHz to 2 GHz with 30 dBm output power.

R. Amirpouer *et al.* presented a Class-J PA with varactor-based dynamic load modulation (DLM). The schematic and a fabricated PA are shown in Fig. 2-15:

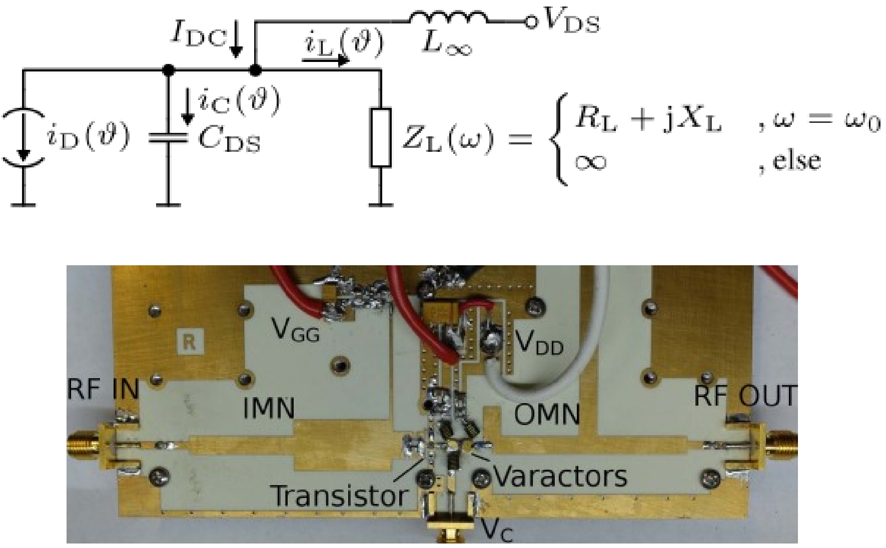

Fig. 2-15. The schematic and fabricated demo broad of Class-J PA with DLM [37].

This work shows a PAE of 40% - 50% in an operating band from 1.7 GHz to 2.3 GHz. Although the optimal impedances required by the transistor are provided accurately by the LM scheme, the overall efficiency is relatively low as the active modulation unit will be energy consuming. Also, the design method requires the impedance tracking to optimise the load impedance actively, which will increase the complexity and cost of the system.

Continuous Mode-Transferring PAs

As discussed in the PA Classification section, some PA modes such as Class-E, Class-F and the continues modes will enhance the efficiency performance significantly by reducing the overlap of the drain current and voltage. However, suffering from the strict impedance requirements for both fundamental and harmonics frequencies, the operating frequency bandwidth is limited. Therefore, to expand the bandwidth, continuous mode concept has been proposed such as Class-B to Class-J [38], [39] and continuous Class-F [40], where the PA modes can be switched between different high-efficiency modes for different frequencies.

K. Chen *et al.* presented a broadband harmonic-tuned PA with in-band mode transferring feature in [41] which is developed from a dual-band PA design [42]. This concept extends the mode-transferring between Class-F and inverse Class-F to a more general case of continuous Class-F and continuous inverse Class-F with the circuit schematic shown in Fig. 2-16:

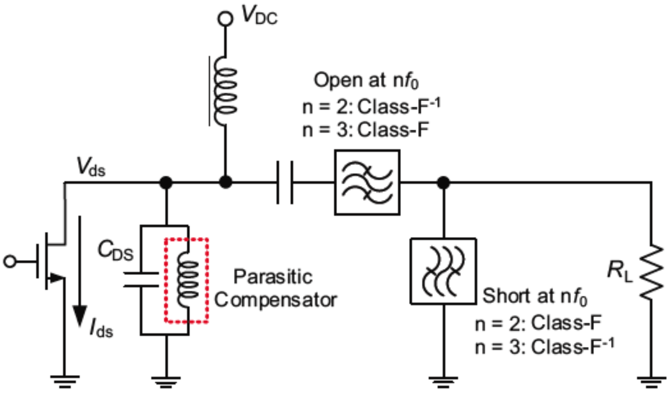

Fig. 2-16. The schematic of Class-F and inverse Class-F PA topology with ideal second and third harmonic terminations [41].

The OMN will provide open-circuit at odd harmonics and short-circuit at even harmonics when the PA is operating in inverse Class-F mode at the lower-half band. The OMN will provide short-circuit at odd harmonics and open-circuit at even harmonics when the PA is operating in Class-F mode at the upper-half band. The ideal frequency response and the matching scheme are shown in Fig. 2-17 and Fig. 2-18:

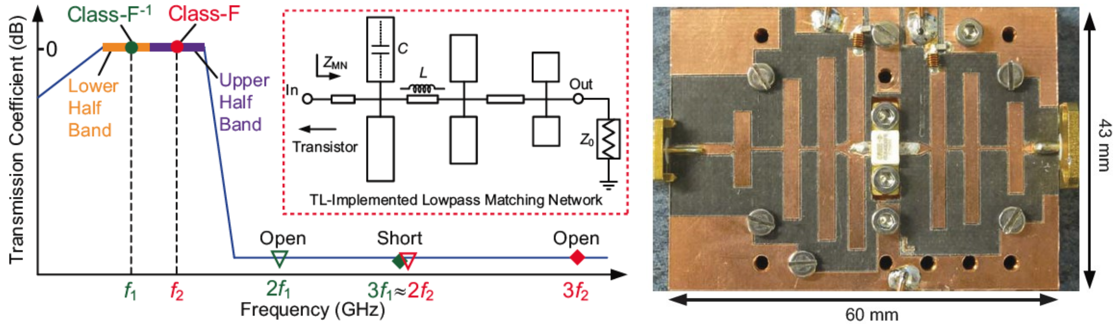

Fig. 2-17. The ideal frequency response of the mode-transferring PA, matching scheme and fabricated PA [41].

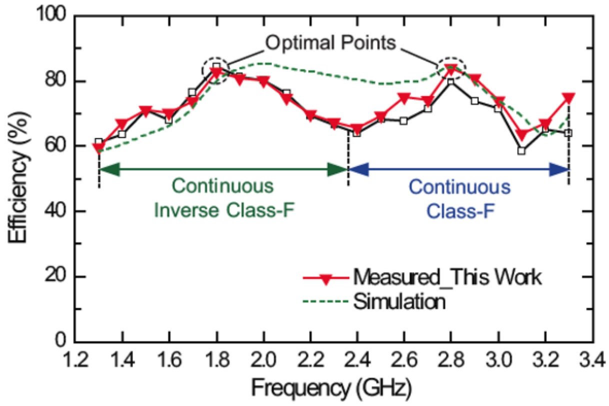

Fig. 2-18. Measured results of the mode-transferring PA [41].

This method will automatically transfer the PA operating mode when the frequency changes, leading to a broadband high-efficiency performance. The measured results show a PAE of 56% - 78% from 1.3 GHz to 3.3 GHz.

C. Huang *et al.* demonstrated a hybrid continuous mode PA with phase shift parameters [43]. The PA will operate between Class-J and continuous Class-F with a phase shift parameter introduced in the voltage waveform to generate the complex fundamental and harmonic load impedances, further extending the bandwidth with high-efficiency. The measured results and a fabricated circuit are shown in Fig. 2-19:

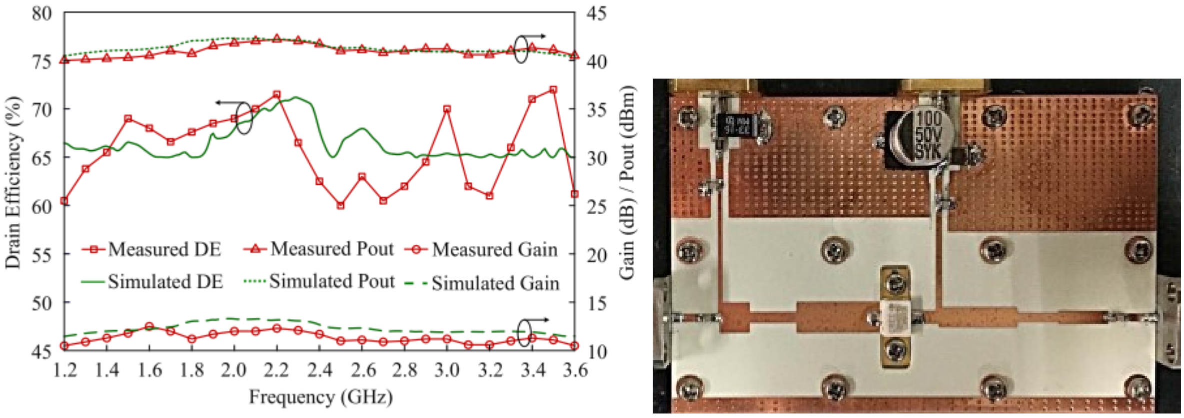

Fig. 2-19. Measured results and a fabricated circuit of the hybrid modes PA [43].

The results show a DE of 65% - 72% when delivering 40.5 – 42.3 dBm output power over a bandwidth of 1.2 GHz – 3.6 GHz.

The continuous mode PA is a promising candidate in achieving high-efficiency broadband performance. However, the bandwidth is still limited by the impedance required to form a specific waveform to realize the desired Class modes. Moreover, the in-band efficiency is also degraded from the optimal design frequency point due to the desired waveform cannot be held when the frequency swept as shown in Fig.2-21 that there are two PAE peaks and multiple efficiency peaks in Fig.2-22. The operation modes are designed based on the optimal frequency points. Therefore, when the frequency shifts from its optimal one, the efficiency decreases. Also, the continuous mode method will not suit for wideband PAs with an octave or multi-octave bandwidth due to the harmonics tuning approach cannot be applied, as the harmonics fall inside the required bandwidth.

Broadband Filter-Type Matching Network

The filter-type matching network is found to be useful in PA design as they can provide the accurate optimal impedances and filter the harmonics simultaneously. Furthermore, the filter-type MN can realize the optimal impedances for an infinite bandwidth theoretically with a relative smooth in-band response. The filter-type MN can transfer the desired impedance to the industrial standard termination value for the desired bandwidth, and then the high-efficiency can be achieved with a relatively stable in-band response.

M. Yang *et al.* presented a continuous inverse Class-F PA using a modified elliptic low-pass filtering MN [44]. Class-F PA requires a short-circuit at the even harmonics and an optimal impedance at the fundamental. Therefore, the impedance transition bandwidth (TBW) from the fundamental frequency to the second harmonics will limit the operating bandwidth of the PA as shown in Fig. 2-20.

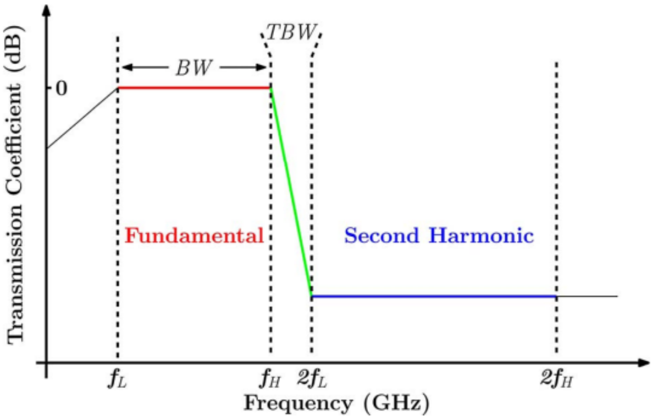

Fig. 2-20. The ideal frequency response of a broadband continuous Class-F PA [44].

The modified elliptic LPF MN will provide a very sharp impedance transition, minimising the TBW to increase the operating bandwidth. The realized MN, measured impedance and measured PA performance are shown in Fig. 2-21 and Fig. 2-22:

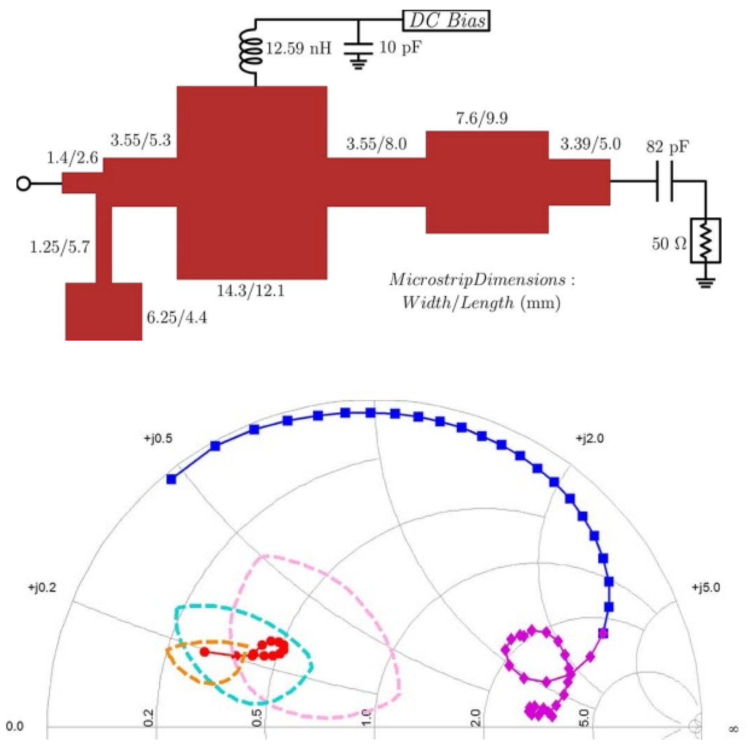

Fig. 2-21. Realized OMN and the measured OMN impedance [44].

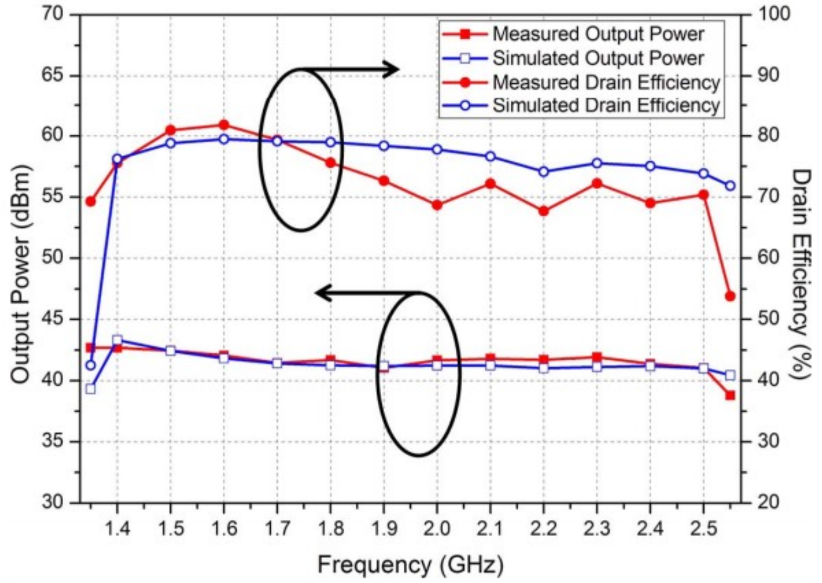

Fig. 2-22. The measured PA performance [44].

The measured results show a DE of 68% - 82% across 1.35 GHz to 2.5 GHz. Different from the mode-transferring PAs, the efficiency performance of the filter-type MN PA is much more flat and stable. However, the bandwidth is still limited by an octave due to the second harmonics must be shorted to form an ideal waveform to achieve the high-efficiency.

P. Saad *et al.* presented a highly efficient octave bandwidth PA using a bandpass filter-type MN based on a source–pull/ load–pull simulation [1]. This method divides the desired bandwidth into several small frequency bands and then performs the source/load pull simulations to find out the optimal impedance yielding the maximum PAE for each frequency band. Due to the optimal impedances are close to each other, the optimal impedance at the centre frequency is selected for the whole frequency bands. A distributed OMN is designed to realize the optimal impedance. The topology and the fabricated circuit are shown in Fig. 2-23 and Fig. 2-24:

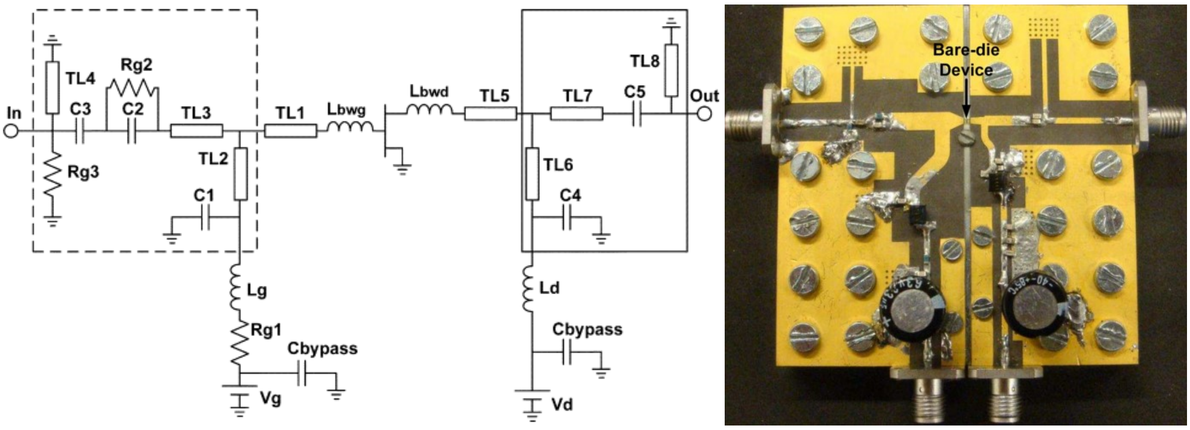

Fig. 2-23. The topology of the octave bandwidth PA and a photo of the PA [1].

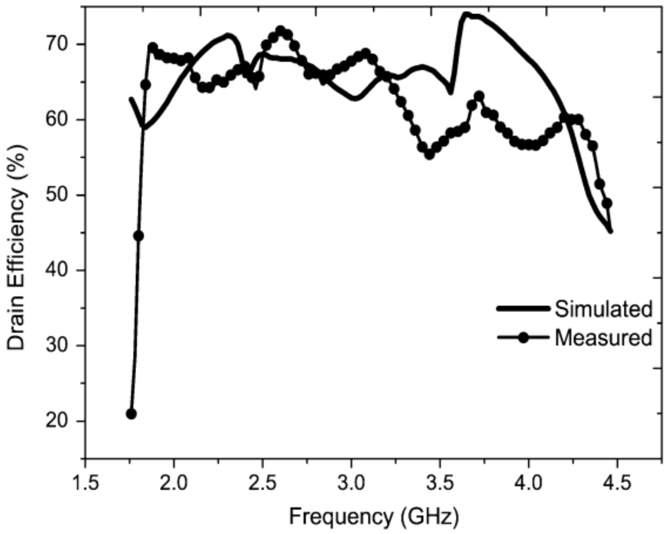

Fig. 2-24. Comparison of the measured and simulated DE performance of the PA [1].

The measured results in Fig. 2-27 indicate a DE of 57% -72% across 1.9 GHz to 4.3 GHz. For a PA with bandwidth better than an octave, the efficiency is very high. However, it should be mentioned that in the filter-type design, the optimal impedances over the whole bandwidth should be close to each other, which means a small impedance variation along the frequency. Otherwise, once the bandwidth is further extended where the optimal impedances are not close to each other anymore, the traditional filter-type design will be no longer suitable.

In summary, the PA classifications with their bias conditions and characteristics have been introduced and analysed. Several broadband high-efficiency PA techniques such as DA, LM based methods, mode-transferring and filter-type MN have been introduced. The pros and cons of these methods have been analysed. The key to realising high-efficiency broadband PAs is assigning the optimal impedance over the whole operating bandwidth. Due to the optimal impedance at different frequencies varies a lot from each other, it is very challenging to present the perfect impedance for a very wide bandwidth. There are mainly two concepts to overcome the challenge. One is matching the various impedances as accurate as possible such as DA and load modulation methods, which will increase the system complexity and sacrifice the overall system efficiency. The other way is minimising the variation of the optimal impedances as used in filter-type MN design by trading off the efficiency performance or the bandwidth.

2.3 References

[1] P. Saad, C. Fager, H. Cao, H. Zirath and K. Andersson, “Design of a highly efficient 2-4ghz octave bandwidth GaN-HEMT power amplifier," *IEEE Trans. Microwave Theory and Techniques*, vol. 58, pp. 1677-1685, Jul.2010.

[2] N. O. Sokal and A. D. Sokal, "Class e-a new class of high-efficiency tunes single-ended switching power amplifiers," *IEEE J. Solid-State Circuits*, vol. SC-10, pp. 168-176, 1975.

[3] C. Han, T. Harrold, S. Armour, "Green radio: Radio techniques to enable energy-efficient wireless network," *IEEE Communication Magazine*, vol. 46, pp. 46-54.

[4] F. J. Ortega-Gonzalez, D. Tena-Ramos, M. Patino-Gomez, J. M. Pardo-Martin, and D. Madueno-Pulido, “High-power wideband L-band suboptimum class-E power amplifier,” *IEEE Trans. Microwave Theory and Techniques.*, vol. 61, no. 10, pp. 3712–3720, Oct. 2013.

[5] J. H. Kim, G. D. Jo, J. H. Oh, Y. H. Kim, K. C. Lee and J. Jung, “Modeling and design methodology of high-efficiency class-F and class-F-1 power amplifier,” *IEEE Trans. Microwave Theory and Techniques*, vol. 59, no. 1, pp. 153–165, Jan. 2011.

[6] R. Tong, S. He, B. Zhang, Z. Jiang, X. Hou, and F. You, “A novel topology of matching network for realizing broadband high efficiency continuous class-F power amplifiers,” in *Eur. Microw. Integr. Circuits Conf.*, pp. 504–507, Oct. 2013.

[7] Steve C. Cripps., RF Power Amplifier for Wireless Communications, Artech House, 2006.

[8] Abdullah A. Almuhaisen, A Novel Approach for Wide Band High-Efficiency Power Amplifier Design, Cardiff University.

[9] B. Berglund, J. Johansson and T. Lejon, "High efficiency power amplifiers," *Ericsson Review*, vol. 3, pp. 92-96, 2006.

[10] J. M. Golio, ‘RF and microwave circuits, measurements, and modelling,’ CRC, Boca Raton,London, 2008.

[11] H. Ma, R. van der Zee, B. Nauta, "Design and analysis of a high-efficiency high-voltage class-D power output stage", *IEEE J. Solid-State Circuits*, vol. 49, no. 7, pp. 1514-1524, Jul. 2014.

[12] L. Guo, T. Ge, J. S. Chang, "A 101 dB PSRR 0.0027% THD + N and 94% power-efficiency filterless Class D amplifier", *IEEE J. Solid-State Circuits*, vol. 49, no. 11, pp. 2608-2617, Nov. 2014.

[13] J. Zhou, K. A. Morris, G. T. Watkins and K. Yamaguchi, “Improved reactance-compensation technique for the design of wideband suboptimum class-E power amplifiers,” *IEEE Trans. Microwave Theory and Techniques.*, vol. 63, no. 9, pp. 2793–2801, Sep. 2015.

[14] F. H. Raab, “Broadband class-E power amplifier for HF and VHF,” in *IEEE MTT-S Int. Microw. Symp. Dig.*, Jun. 11–16, 2006, pp. 902–905.

[15] K. Narendra and Y. K. Tee, “Optimized high-efficiency class E RF power amplifier for wide bandwidth and high harmonics suppression,” *IET Circuits, Devices, Syst.*, vol. 60, no. 10, pp. 1–13, Feb. 2014.

[16] F. J. Ortega-Gonzalez, D. Tena-Ramos, M. Patino-Gomez, J. M. Pardo-Martin, and D. Madueno-Pulido, “High-power wideband L-band suboptimum class-E power amplifier,” *IEEE Trans. Microwave Theory and Techniques.*, vol. 61, no. 10, pp. 3712–3720, Oct. 2013.

[17] K. Chen and D. Peroulis, “Design of highly efficient broadband class-E power amplifier using synthesized low-pass matching networks,” *IEEE Trans. Microwave Theory and Techniques*, vol. 59, no. 12, pp. 3162–3173, Dec. 2011.

[18] J. Zhou, K. Morris, G. Watkins, and K. Yamaguchi, “Wideband class-E power amplifier covering the whole UHF broadcast band,” in *Eur. Microw. Conf.*, Nuremberg, Germany, 2013, pp. 1307–1310.

[19] A. J. Wilkinson, J. K. A. Everard, “Transmission-line load network topology for class-e power amplifiers,” *IEEE Trans. Microwave Theory and Techniques.*, vol. 49, no. 6, pp. 1202–1210, Jun. 2001.

[20] N. Tuffy, L. Guan, A. Zhu, and T. Brazil, “A simplified broadband design methodology for linearized high-efficiency continuous class-F power amplifiers,” *IEEE Trans. Microwave Theory and Techniques.*, vol. 60, no. 6, pp. 1952–1963, Jun. 2012.

[21] K. Chen and D. Peroulis, “Design of broadband highly efficient harmonic-tuned power amplifier using in-band continuous class-F-1/*f* mode transferring,” *IEEE Trans. Microwave Theory and Techniques.*, vol. 60, no. 12, pp. 4107–4116, Dec. 2012.

[22] M. Yang, J. Xia, Y. Guo and A. Zhu, “Highly efficient broadband continuous inverse class-F power amplifier design using modified elliptic low-pass filtering matching network,” *IEEE Trans. Microwave Theory and Techniques.*, vol. 64, no. 5, pp. 1515–1525, May. 2016.

[23] J. H. Kim, G. D. Jo, J. H. Oh, Y. H. Kim, K. C. Lee and J. Jung, “Modeling and design methodology of high-efficiency class-F and class-F-1 power amplifier,” *IEEE Trans. Microwave Theory and Techniques.*, vol. 59, no. 1, pp. 153–165, Jan. 2011.

[24] A. Sheikhi, M. Hayati and A. Grebennikov, “A design methodology of class-E/F3 power amplifier considering linear external and nonlinear drain-source capacitance,” *IEEE Trans. Microwave Theory and Techniques.*, vol. 65, no. 2, pp. 548–554, Feb. 2017.

[25] G. Sun and R. Jansen, “Broadband Doherty power amplifier via real frequency technique,” *IEEE Trans. Microwave Theory and Techniques.*, vol. 60, no. 1, pp. 99–111, Jan. 2012.

[26] M. Akbarpour, F. M. Ghannouchi and M. Helaoui, “Current biasing of power amplifier transistors and its application for ultra-wideband high efficiency at power back-off,” *IEEE Trans. Microwave Theory and Techniques.*, vol. 65, no. 6, pp. 2192–2200, June. 2017.

[27] A. Barakat, M. Thian, V. Fusco, S. Bulja and L. Guan, “Toward a more generalized Doherty power amplifier design for broadband operation,” *IEEE Trans. Microwave Theory and Techniques.*, vol. 65, no. 3, pp. 846-859, March. 2017.

[28] W. H. Doherty, “A new high efficiency power amplifier for modulated waves,” *Proceedings of the Institute of Radio Engineers*., vol. 29, no. 9, pp.1163–1182, Sep. 1936.

[29] B. Kim, J. Kim, I. Kim and J. Cha, “The Doherty power amplifier,” *IEEE Microwave Magazine.*, vol. 7, no. 5, pp. 1527-3342, Oct. 2006.

[30] W. S. Percival, “Thermionic Valve Circuits,” British Patent Specification no. 460,562, filed 24 July 1936, granted January 1937.

[31] E. W. Strid; K. R. Gleason. "A DC-12 GHz Monolithic GaAs FET Distributed Amplifier". *IEEE Trans. Microwave Theory and Techniques*. Vol. 30, no. 7, pp. 969–975. DOI:10.1109/TMTT.1982.1131185, 1982.

[32] Y. Ayasli; R. L. Mozzi; J. L. Vorhaus; L. D. Reynolds; R. A. Pucel, "A Monolithic GaAs 1-13-GHz Traveling-Wave Amplifier". *IEEE Trans. Microwave Theory and Techniques*. Vol. 30, no. 7, pp.976–981. doi:10.1109/TMTT.1982.1131186, 1982.

[33] K. B. Niclas; W. T. Wilser; T. R. Kritzer; R. R. Pereira. "On Theory and Performance of Solid-State Microwave Distributed Amplifiers". *IEEE Trans. Microwave Theory and Techniques*. Vol, 31, no. 6, pp. 447–456. DOI:10.1109/TMTT.1983.1131524, 1983.

[34] X. Zhou, L. Roy and R. E. Amaya "1W, highly efficient ultra-broadband non-uniform distributed power amplifier in GaN". *IEEE Trans. Microwave and Components Letters*. Vol, 23, no. 4, pp. 208–210, Apr. 2013.

[35] K. Chen and D. Peroulis, “Design of adaptive highly efficient GaN power amplifier for octave-bandwidth application and dynamic load modulation,” *IEEE Microw. Theory Tech*., vol. 60, no. 6, pp. 1829–1839, 2012.

[36] D. J. Shepphard, J. Powell and S. C. Cripps "An efficient broadband reconfigurable power amplifier using active load modulation". *IEEE Trans. Microwave and Components Letters*. Vol, 26, no. 6, pp. 443–445, Jun. 2016.

[37] R. Amirpour, R. Darraji, F. Ghannouchi and R. Quay, "Enhancement of broadband efficiency of a Class-J power amplifier with varactor-based dynamic load modulation". *IEEE Trans. Microwave and Components Letters*. Vol, 27, no. 2, pp. 180–182, Feb. 2017.

[38] P. Wright, J. Lees, J. Benedikt, P. J. Tasker, and S. C. Cripps, "A methodology for realizing high efficiency class-J in a linear broadband PA," *IEEE Trans. Microw. Theory Tech*., vol. 57, no. 12, pp. 3196–3204, Dec. 2009.

[39] J. R. Powell, M. J. Uren, T. Martin, A. McLachlan, P. J. Tasker, J. J. Bell, R. S. Saini, S. P. Woodington, J. Benedikt, and S. C. Cripps, "GaAs X-band high efficiency (65%) broadband (30%) amplifier MMIC based on the Class B to Class J continuum," in *IEEE MTT-S Int. Dig.*, Jun. 2011, pp. 1–4.

[40] V. Carrubba, J. Lees, J. Benedikt, P. J. Tasker, and S. C. Cripps, "A novel highly efficient broadband continuous class-F RFPA delivering 74% average efficiency for an octave bandwidth," in *IEEE MTT-S Int. Dig*., Jun. 5–10, 2011, pp. 1–4.

[41] K. Chen and D. Peroulis, "Design of broadband highly efficient harmonic-tuned power amplifier using in-band continuous Class mode-transferring," *IEEE Trans. Microw. Theory Tech*., vol. 60, no. 12, pp. 4107–4116, Dec. 2012.

[42] Y. Ding, Y. Guo, and F. Liu, "High-efficiency concurrent dual-band class-F and inverse class-F power amplifier," *IET Electronics letters*, vol. 47, no. 15, pp. 847–849, Aug. 2011.

[43] C. Huang, S. B. He, W. Shi and B. Song, "Design of broadband high-efficiency power amplifiers based on the hybrid continuous modes with phase shift parameter". *IEEE Trans. Microwave and Components Letters*. Vol, 28, no. 2, pp. 159–161, Feb. 2018.

[44] M. Yang, Y. Guo and A. Zhu, "Highly efficient broadband continuous inverse Class-F power amplifier design using modified elliptic low-pass filtering matching network," *IEEE Trans. Microwave Theory and Techniques*., vol. 60, no. 12, pp. 4107–4116, Dec. 2012.

Chapter 3 **Design of a Broadband PA with Constrained Optimal Impedance Contours**

This chapter presents the design, implementation and experimental results of a broadband high-efficiency GaN-HEMT power amplifier (PA) with constrained optimal impedance contours. Due to that the optimal impedance for both input and output of a transistor varies with frequency, the impedance variation is constrained by establishing optimal impedance contours covering the required optimal impedance across the desired bandwidth. Source-pull and load-pull simulations were employed to determine the optimum input and output impedances of a GaN transistor over 0.9-1.5 GHz to achieve high power added efficiency (PAE). A low-pass network based on a closed-form solution was applied for impedance matching. Then it was transferred to a band-pass network. Norton Transformation is used to increase the magnitude of impedances without sacrificing bandwidth or matching. Experimental results shown that the PA can achieve a power gain of 9.5-13.5 dB across 0.9-1.5 GHz while the output power is 10-22W. The corresponding PAE is 60%-86%. This PA is suitable for satellite communications systems and particularly GNSS applications.

3.1 Introduction

A PA can be used for transferring DC power into RF power in wireless communications systems. The efficiency of PAs will significantly influence the power consumption of the system. Moreover, the performance of the PA in terms of bandwidth, efficiency, output power and linearity, determines the overall features of the system. It makes the design of broadband PAs with high efficiency an important topic.

The broadband feature of PAs can be realized by several techniques such as distributed amplifier [1] [2]. Although flat gain and high linearity can be achieved through a distributed amplifier, a large number of devices are required, increasing the cost, size and reducing the efficiency. To improve the efficiency, some popular solutions are widely used including class D, class E/E^{-1}, class F/F^{-1}, and Doherty. Those switched-mode or harmonically tuning PAs have high efficiency over a narrow bandwidth. There are many broadband high-efficiency PAs using switched-mode reported in the literature [3]-[5]. Designing a PA with wide bandwidth and high efficiency simultaneously is an attractive research area.

In this chapter, the design of a GaN PA operating over the frequency range of 0.9-1.5 GHz (50% fractional bandwidth) with 60%-86% PAE is presented. The PA covers the majority of the Global Navigation Satellite System (GNSS) frequency bands from 1164 MHz to 1591 MHz. This design employed source/load-pull simulation to find the optimal source and load impedances. A low-pass network was designed first to match the optimum impedances and transferred to a band-pass network. Then a PI-type Norton transformation was applied to scale the load of the band-pass network to 50 Ω. A general method for the design of a broadband matching network is presented in this chapter.

3.2 Design of the Power Amplifier

To realize a broadband efficient PA, bandpass filters were selected as the approach to design input and output matching networks to match the optimum source and load impedances to 50 Ω. The topology is shown in Fig. 3-1. A 25-W Cree GaN-HEMT CGH40025F sealed in the Cree 440166 package was chosen to realize the broadband high-efficiency PA, due to its high breakdown voltage and low output capacitance [6]. In this case, the PA works in the switched-mode for maximum PAE. Care should be taken in the design not to damage the device as the peak drain voltage is much higher than the DC supply voltage [7].

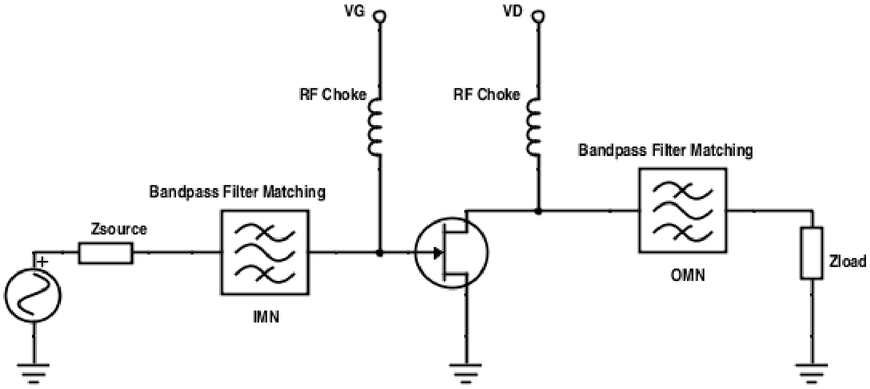

Fig. 3-1. Typical broadband PA topology.

3.2.1 Source-Pull and Load/Pull Simulations

Source-pull and load-pull simulations have been performed using the large signal model by Advanced Design System (ADS) to find the optimum input and output impedances of the transistor in terms of maximum power added efficiency (PAE) across 0.9-1.5 GHz. Due to the nonlinearity of the transistor, the source and load impedances vary with frequency. The matching network has to match those impedances at each frequency to deliver RF power efficiently over the desired bandwidth. To minimize the effects of packaging, the intrinsic parasitic values are modelled via [6] and the datasheet from the manufacturer. The extrinsic parasitic capacitances are calculated according to the Y-parameter frequency responses of the FETs and the linear regression technique provided in [8]. Then, load-pull simulations were conducted at 0.9, 1.1, 1.3, 1.5 GHz. The results of the PAE contours higher than 70% are shown in Fig. 3-2.

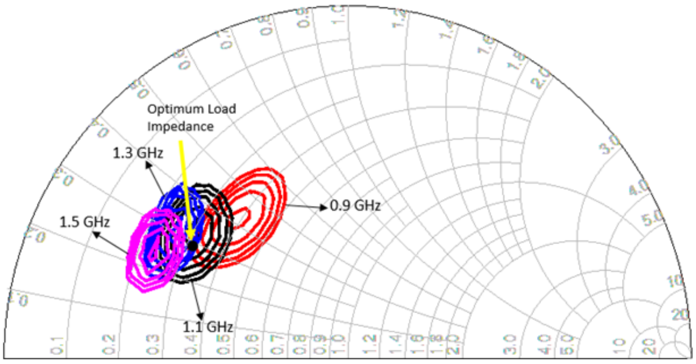

Fig. 3-2. Contours with optimal impedance leading to higher than 70% PAE.

Design reported in [3] - [5], [9] focused on the impedances of maximum PAE and then determine the optimum impedance at the centre frequency. This work analyses not only the maximum PAE but also the PAE contours higher than 70%. It can be seen that the PAE contours have an interaction point at $16+j13.5\ \Omega$. With this impedance, the PAE at 0.9, 1.1, 1.3, 1.5 GHz are 70%, 83.2%, 80% and 69% respectively. Hence, the optimum load impedance was chosen as $Z_{L,Opt}=16+j13.5\ \Omega$. Similarly, the optimum source impedance can be determined with the same procedure. It was chosen to be $Z_{S,Opt}=7.2+j5\ \Omega$. In this case, the matching network only needs to match $Z_{S,Opt}$ and $Z_{L,Opt}$ at the input and output to 50 Ω across 0.9-1.5 GHz.

3.2.2 Matching Network Design

The optimal impedances of the source and load have been obtained as described in the previous section. Then, the output of the transistor can be modelled as an ideal current source with a shunt R-C network [9]. The optimum output impedance $Z_{L,Opt}$ can be realized by an output resistance of $R_{out} = 27.4\ \Omega$ and an output capacitance of $C_{out} = 4.1\ pF$ in parallel as shown in Fig. 3-3. Therefore, the task becomes to design an output matching network (OMN) that matches the shunt R-C network to a 50 Ω load across 0.9-1.5 GHz. Firstly, a lumped low-pass network can be designed using the method extracted from [10]. To realize the desired bandwidth, a third-order low-pass network is used. The normalized g-elements are shown in Fig. 3-3(a). The low-pass network can be transferred to a band-pass network as shown in Fig. 3-3(b). Since the load of the matching network is not 50 Ω, an ideal transformer with a ratio of n=1.36 can be applied to upscale the load to 50 Ω. The two series-shunt capacitors C_1 and C_2 are transformed to a PI network using Norton transformation with the inductor and resistor scaled up by a ratio of $n^2 = 1.845$ [11].

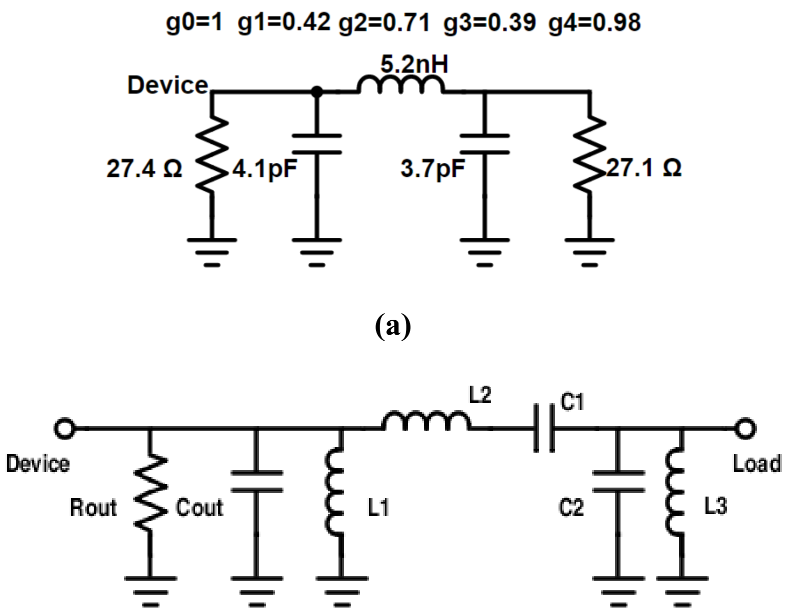

(a)

(b)

Fig. 3-3. Output matching network (a) Low-pass, (b) Band-pass.

The lumped network is converted to the distributed network as shown in Fig. 3-3. The TL_1 was added as a tapper to connect the output pin of the transistor as shown in Fig. 3-7. L_1 was replaced by a transmission line TL_2 left open at the far end with the line impedance equal to 4/π times the reactance of the inductor. Similarly, L_2 was transformed to TL_3. The DC-blocking capacitor C_1 was realized by a lumped element. The grounded parallel L_3 and C_2 can be approximated by a shorted transmission line [12]. The layout of the distributed OMN is shown in Fig. 3-4.

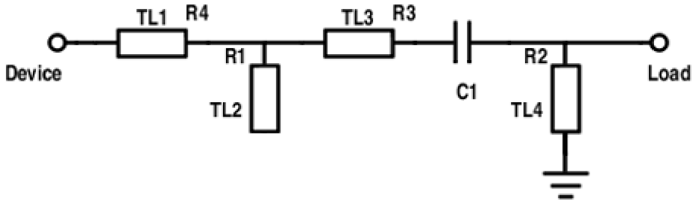

Fig. 3-4. Layout of the distributed-element OMN.

The resistors in the bias network are used to ensure the amplifier is unconditional stable across the desired bandwidth. Two inductors are added in the bias circuit to prevent the RF signal from leaking to DC supply. The same procedure presented above can be used to design the input matching network (IMN). Tuning has been made using computer-aided-design tool to maximize the efficiency and overcome the effects of bending the transmission lines. The completed circuit schematic of the designed PA is shown in Fig. 3-5.

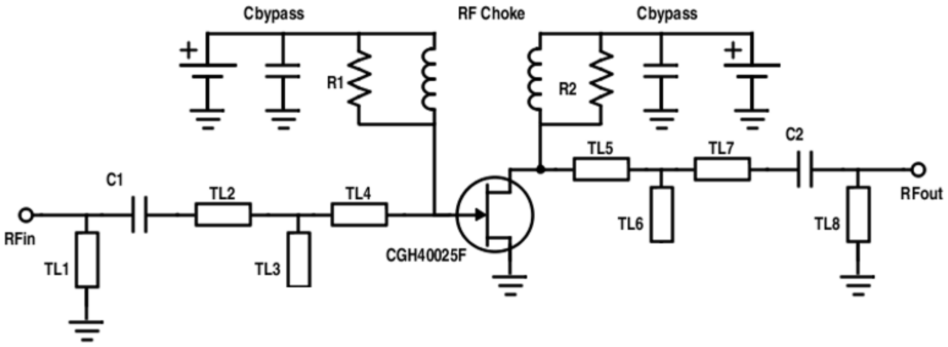

Fig. 3-5. Circuit diagram of designed broadband PA.

The PA was biased at *Vg = -3.5 V* and *Vd = 30 V*. The simulated drain voltage and current waveforms of the designed PA at 1 GHz and 1.4 GHz are shown in Fig. 3-6. Simulated results from (Advanced Design System 2016 with transistor model provided by Cree) indicate that the amplifier was working at the switched mode. The duration of the overlap of current and voltage waveform is reduced to enable the amplifier to achieve high efficiency.

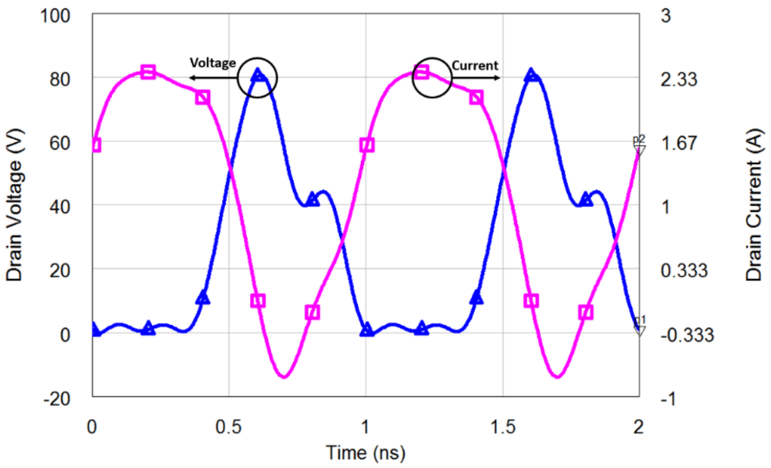

(a)

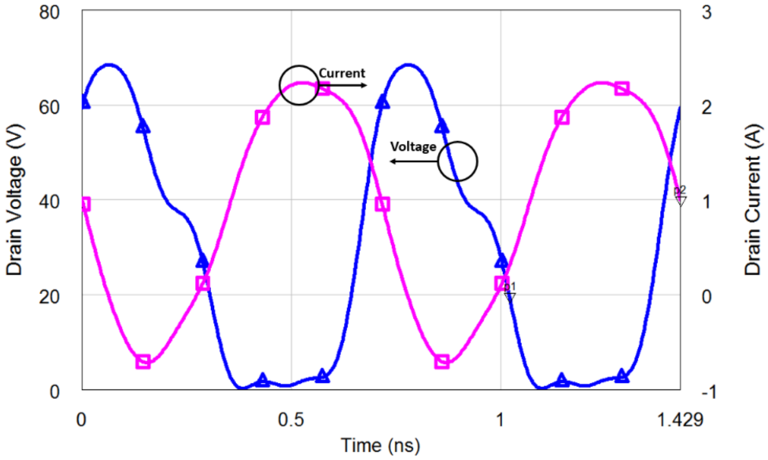

(b)

Fig. 3-6. Simulated drain voltage and current waveforms of the broadband PA at: (a) 1 GHz (b) 1.4 GHz.

3.3 Measurement Results and Discussion

3.3.1 Fabrication of the broadband PA

The fabricated broadband PA is shown in Fig. 3-7. A 25-W Cree GaN-HEMT (CGH40025F) was chosen to realize the design. The high breakdown voltage will ensure safe operation of the transistor in the switched-mode operation [7]. The PA was implemented on a 1.52 mm thick Rogers 4350B substrate with $\varepsilon_r = 3.48$ and 1 oz/sqft copper.

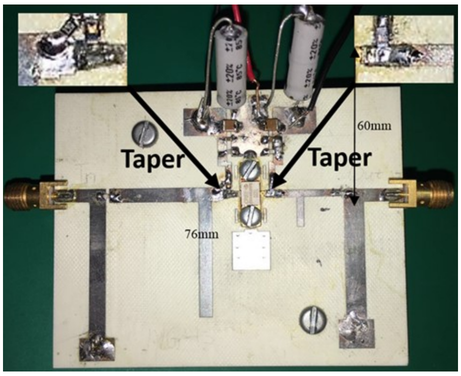

Fig. 3-7. A photo of the fabricated broadband PA.

3.3.2 Measured Results

The fabricated broadband PA was characterized by large signal measurement to investigate its performance. The PA is tested with a single-tone CW input signal from 0.8 to 1.6 GHz generated by a KEITHLEY 2920 RF Signal Generator. A commercial general-purpose wideband PA ZHL42 from Mini Circuits was used as a buffer amplifier to provide a 30 dBm input signal to the designed PA. The output power level was measured by a power meter from Rohde & Schwarz (NRP-Z85). The gate of the transistor was biased at -3.5 V and the drain voltage was 30 V. The measured PAE, gain, output power and simulated PAE at fixed 30 dBm input power are shown in the Fig. 3-8. The broadband PA has a PAE higher than 60% over the desired bandwidth along with 9.5-13.5 dB gain. The corresponding output power varies from 40 dBm to 43.5 dBm. The results show the PAE are relatively high at around 1.1-1.2 GHz and falls down to 60% and 63% at 0.9 and 1.5 GHz, respectively. This is mainly due to that the matching network was designed to match the same impedance rather than the optimum impedances at each frequency point.

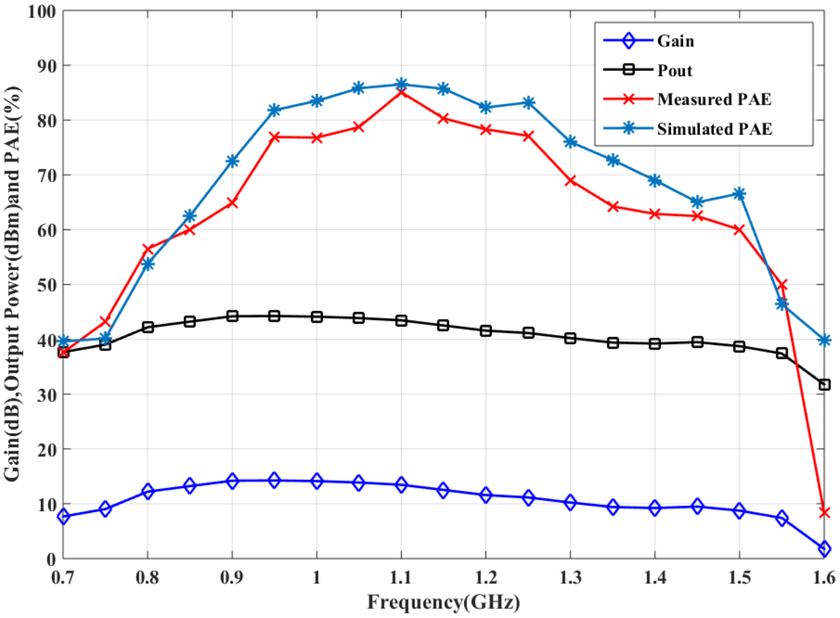

Fig. 3-8. Measured Gain, output power, PAE and simulated PAE versus frequency at fixed 30 dBm input power.

The PA exhibits excellent efficiency at the lower L-band from 1.15 GHz to 1.3 GHz for GNSS applications and very high efficiency for the upper L-band. If desired, the PA can be further tuned by shifting the operating frequency slightly higher to cover the full L-band for GNSS applications.

3.4 Conclusion

In this chapter, the detailed design methodology, implementation procedure and measurement results of a broadband high-efficiency PA are presented. Source-pull and load-pull simulations were applied to find the optimum input and output impedances of the transistor. A low-pass network was designed first to match the optimum impedances and it was transferred to a band-pass network. Then a PI-type Norton transformation was applied to scale up the load of the band-pass network to the 50 Ω. The designed PA achieved a PAE of 60%-86% across 0.9-1.5 GHz (50%) with a relatively flat gain around 11 dB and high output power of 10 to 22 W. The measured performance shows that the PA is a good candidate for satellite communications and GNSS applications.

3.5 References

[1] J. Gassmann, P. Waston, L.Kehias, and G. Henry, “Wideband, high- efficiency GaN power amplifiers utilizing a non-uniform distributed topology,” in *IEEE MTT-S Int. Microw. Symp. Dig.*, pp. 615-618, Jun. 2007,

[2] K. Entesari, A. R Tavakoli, and A. Helmy, “CMOS distributed amplifiers with extended flat bandwidth and improved input matching using gate line with coupled inductors,” *IEEE Trans. Microw. Theory Tech.,* vol. 57, no. 2, pp. 2868-2871, Dec. 2009.

[3] H. Wu, Q. Cheng, “A high efficiency and high linearity two-stage power amplifier,” in *IEEE MTT-S Int. Microw. Symp.*, pp.1-4, Jul. 2015.

[4] K. Narendra and Y. K. Tee, “Optimized high-efficiency class E RF power amplifier for wide bandwidth and high harmonics supperssion,” *IET Circuits, Devices, Syst.*, vol. 60,no. 10, pp. 1-13, Feb. 2014.

[5] J. Zhou, K. A. Morris, G. T. Watkins, and K. Yamaguchi, “Improved reactance-compensation technique for the design of wideband suboptimum class e power amplifier,” *IEEE Trans. Microw. Theory Tech.,* vol. 63, no. 9, pp.2793-2801, Sep. 2015.

[6] R. Pengelly, B. Millon, D. Farrell, B. Pribble, and S. Wood, “Application of non-linear models in a range of challenging GaN HEMT power amplifier designs,” presented at the *IEEE MTT-S Int. Microw. Symp. Workshop,* Jun. 2008.

[7] N. O. Sokal and A. D. Sokal, “Class-E- A new class of high-efficiency tunes single-ended switching power amplifiers,” *IEEE J. Soild-State Circuits,,* vol. SC-10, no. 3, pp.168-176, Jun. 1975.

[8] Y. Lai, and K. Hsu, “A new pinched-off cold-FET method to determine parasitic capacitances of FET equivalent circuits,” *IEEE Trans. Microw. Theory Tech.,* vol. 49, no. 8, pp.1410-1418, Aug. 2001.

[9] P. Saad, C. Fager, H. Cao, H. Zirath, and K. Andersson, “Design of a highly efficient 2-4 GHz octvae bandwidth GaN-HEMT power amplifier,” *IEEE Trans. Microw. Theory Tech.,* vol. 58, no. 7, pp. 1677-1685, Jul. 2010.

[10] D. Dawson, “Closed-form solutions for the design of optimum matching networks,” *IEEE Trans. Microw. Theory Tech.,* vol. 57, no. 1, pp.121-129, Jan. 2009.

[11] T. T. Ha, *Solid-State Microwave Amplifier Design*. New York: Wiley, 1981.

[12] P. L. D. Abrie, *The Design of Impedance-Matching Networks for Radio-Frequency and Microwave Amplifiers,* Dedham, MA: Artech House, 1985.

Chapter 4 Adaptive Impedance Matching of a Multioctave High-Efficiency Power Amplifier Using Stochastic Reduced Order Models

This chapter presents a novel general design method of frequency varying impedance matching. Due to the optimal impedance required for a multi-octave PA vary in a large range, variation constraining method cannot be applied. The method introduced in this chapter will be focusing on adaptively matching the variable optimal impedances required by the PA over a wide bandwidth. The proposed method defines the optimal impedance regions of a PA at several frequency sections over the operational frequency band. These regions contain impedances with which a PA can achieve high output power and high power added efficiency (PAE) simultaneously. An LC-ladder circuit is selected as the matching network (MN). The element values of the MN can be obtained using a synthesizing method based on stochastic reduced order models and Voronoi partition. The MN provides a desired impedance in the predefined optimal region at each frequency section. Thus, optimal output power and PAE of the PA can be achieved. To validate the proposed method, two eighth-order low-pass LC-ladder networks are designed as the input and output matching networks, respectively. A GaN HEMT from Cree is employed as the active device. Packaging parasitic of the transistor has been taken into account. A PA is designed, fabricated and measured. The measurement results show that the PA can achieve P1dB PAE of better than 60% over a fractional bandwidth of 160% (0.2-1.8 GHz). The output power is 42-45dBm (16-32 W) and the gain is 12 -15 dB. The performance of the PA outperforms existing broadband high-efficiency PAs in many aspects which demonstrates the excellence of the proposed method.

4.1 Introduction

Power amplifiers (PAs) are essential devices of many communication systems. The features of a PA regarding the bandwidth, power gain, linearity, output power and power added efficiency (PAE) could significantly affect the overall performance of the system. A high-power, high-efficiency broadband PA is in high demand by the industry and market. Consequently, a lot of research effort has been made in this area. To achieve a high-efficiency PA, designs reported in the literature have adopted techniques such as Class-E [1] - [9], Class-D [9], [10], Class-F/F-1 [11] – [16] and Doherty structures [17] – [21]. Although these methods enhance the efficiency of a PA, the requirement on accurate waveform engineering would restrict the bandwidth. To broaden the bandwidth of a PA, some designs such as [22] – [25] use a filter-type matching network (MN) to match the fixed optimal impedance at the centre frequency of the PA over a wide bandwidth. This technique achieves the optimal performance at the centre frequency and compromises the performance at other frequencies as the impedance of the matching network will vary from the optimal impedances at other frequencies. However, this method requires the optimal impedances across the band to be relatively close to each other. Therefore, this approach is not applicable to the design where the optimal impedance is not close to each other, which is a usual case for a multi-octave PA.

Conventional computer-aided design (CAD) tools can be used for this kind of problems. However, CAD optimizers require good initial element values to start with [17], [25]. Methods such as the real frequency technique [38] and Bayesian optimization [37] can be applied to solve the problem. A proper initial guess or data training will be required for such optimizers, which can be very time-consuming [39].

This chapter presents a simple and effective method for the design of broadband high-efficiency PAs. This new approach divides the wide frequency band into several frequency sections. At each frequency section, an optimal impedance region will be obtained, where the output power and PAE of the PA can be maintained at a resonably high level. The main advantage of the proposed method is that the MN can be obtained using the Stochastic reduced order model (SROM) method and a Voronoi partition directly. No initial guess or data training is required. The chapter is organized as follows. The design method is detailed and explained in Section 4.2, including how to define the optimal impedance regions and how to match the impedance with a low-pass LC-ladder network. Source-pull/load-pull simulations are performed to obtain the frequency dependent optimal impedance regions for the PA. As an example, the proposed design method is used to design a matching network in Section 4.3, and the MN is fabricated and measured to validate the method. In Section 4.4, A 25-W Cree GaN HEMT CGH40025F is used to design a PA, whose package parasitic is carefully analyzed. The measurement results of the PA are presented and discussed. Conclusions are finally drawn in Section 4.5.

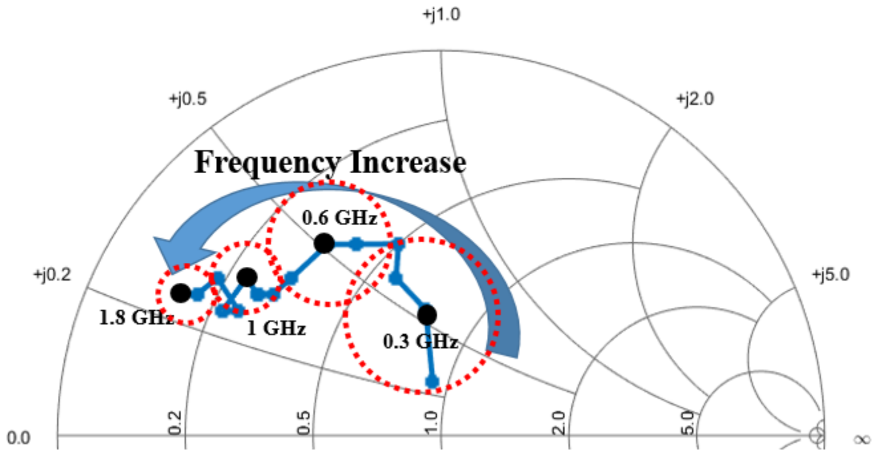

Fig. 4-1. PAE optimal impedance of a CGH40025F transistor at different frequencies (0.3, 0.6, 1 and 1.8 GHz).

4.2 Proposed Matching Network Design Method

4.2.1 Broadband High-Power High-Efficiency PA Analysis

The impedance presented to the gate and drain of a transistor could significantly affect the performance of a PA. Therefore, MNs with desired impedance are required for the transistor to achieve high performance. For broadband PA design, the impedances to achieve high PAE or high output power are usually different at different frequencies. Source-pull and load-pull techniques can be applied to find the optimal impedances for the PAE and output power. Fig. 4-1. shows the PAE contours from 0.2 GHz to 1.8 GHz of a CGH40025F transistor in a Smith Chart. The contours vary with frequency and are quite different from each other. Consequently, to design an efficient high-power PA over an ultra-wide bandwidth, the optimal impedances should be implemented at different frequency regions across the band, instead of at the centre frequency.

It is very common that the output power and PAE contours are not identical as shown in Fig. 4-2. The impedance to maximize the PAE could limit the output power and vice versa. An optimal impedance region at each frequency region should be defined, which contains the impedance values that allows the PA to achieve high performance with a PAE and an output power better than the lowest acceptable levels as shown in Fig. 4-2.

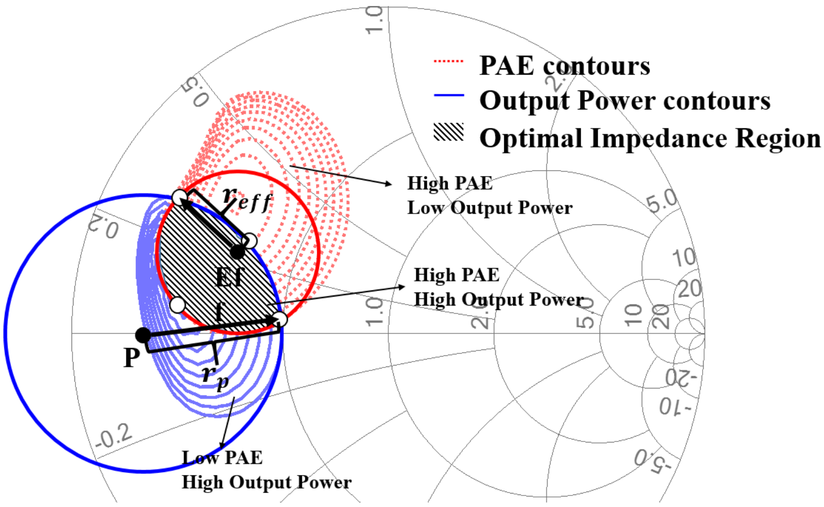

Fig. 4-2. PAE contours, output power contours and the definition of an optimal impedance region at 1 GHz of a CGH40025F.

4.2.2 Frequency-Dependent Optimal Impedance Regions

The design methods reported in [7], [23], [24] that used the optimal impedance at the centre frequency for the whole frequency band may not be the best for a multi-octave PA design. The entire bandwidth can be separated into several frequency sections. The optimal impedance region at the centre frequency of each frequency section can be selected to represent the optimal impedance of this frequency section. In the literature, it is very common that designers simply divide the frequency band into several sections evenly such as [2], [22], [23], [25]. It is very important to notice that for an ultra-wideband design, the variation of the optimal impedance across the band is not uniform. As shown in shown in Fig. 4-1., the PAE optimal impedance of a CGH40025F is simulated by Advanced Design System (ADS) from 0.2 GHz to 1.8 GHz with a step of 0.1 GHz. As Fig. 4-1. shows, the optimal impedances are getting closer at higher frequencies, but in general are very different at different frequencies.

Hence, more frequency sections should be set at lower frequencies to ensure that the optimal impedance at the centre frequency of the section can be representative, for the PA to maintain the desired performance over the corresponding frequency section. Thus, the separation of the frequency band should be based on the variation of the optimal impedances across the bandwidth. The optimal impedance regions can be chosen based on the desired features of a PA such as the power gain, linearity, output power, PAE or any other parameters. In this work, high output power and high PAE are the main design targets. The optimal impedance regions across the band are defined and modelled as follows:

1) Divide the entire operating bandwidth into *k* frequency sections. The number of frequency sections depends on the bandwidth and the variation of optimal impedances at different frequencies.
2) For each frequency section, the output power and PAE contours of the centre frequency of this section can be obtained via source-pull/load-pull simulation. The boundary of the contours is defined by the lowest output power and PAE acceptable for the design. The overlap region of output power and PAE contours is selected to be the optimal impedance region (shaded area in Fig. 4-2.). If the contours do not overlap, a sacrifice is necessary to extend the PAE or output power contours until they have an overlap region (if the output power is the priority concern, the lowest acceptable PAE level should be reduced and vice versa).
3) For mathematical convenience, the optimal impedance region can be approximated by two circles as shown in Fig. 4-2. Any three non-collinear points can define the circumference of one circle, and one circle only. Two intercept points of the PAE and output power contour boundaries and another point on the PAE contour boundary inside the output power contour can define the PAE circle. The circle of output power can be defined likewise. Then the overlap region of the PAE and output power circles is defined as the optimal impedance region. The impedance values of the region can be expressed as a function of frequency as:

$$\begin{cases} d_P(\omega_x) \le r_P(\omega_x) \\ d_{Eff}(\omega_x) \le r_{Eff}(\omega_x) \end{cases} \tag{4.1}$$

where $\omega_x=2\pi f_x$, $x=1, 2,.., k,$ and k is the number of frequency sections. d_P and d_{Eff} are the Euclidean distance from the impedance point to the centre of the PAE and output power circles, r_P and r_{Eff} are the radii of the PAE and output power circles respectively.

The optimal impedance region at each frequency section across the desired bandwidth can be obtained as described above. The input impedance of the MN seen by the transistor at each frequency section should be constrained to the corresponding optimal impedance region. This approach will enable the output power and PAE of a PA to be better than the pre-defined level over the whole operational band. Also, some other features of a PA such as noise figure or gain can be included to define the optimal region as well if required.

4.2.3 Synthesis of the Matching Networks

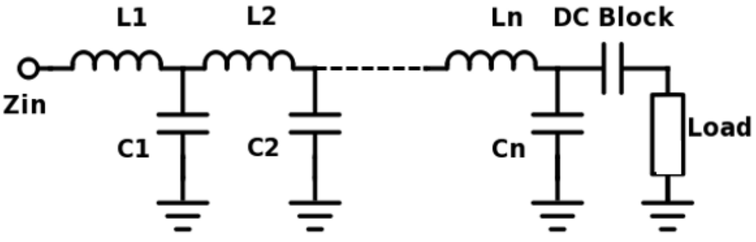

Fig. 4-3. A low-pass LC-ladder matching network with a DC block.

Once the optimal impedance regions across the entire bandwidth are defined, the task resides in realizing the desired impedances using a proper circuit topology. A low-pass LC-ladder matching network with a DC block capacitor as shown in Fig. 4-3. is chosen as the MN due to its desired in-band and out-of-band behaviour as analysed in [6], [27]. The input impedance of the MN can be described as a function of frequency and element values. Firstly, the MN can be treated as a cascaded structure of several LC sections. The ABCD matrix of the MN can be expressed [28] as:

$$\begin{bmatrix} A(\omega_x) & B(\omega_x) \\ C(\omega_x) & D(\omega_x) \end{bmatrix}_{LC} = \prod_{i=1}^{n} \begin{bmatrix} 1-\omega_x{}^2 L_i C_i & j\omega_x L_i \\ j\omega_x C_i & 1 \end{bmatrix} \tag{4.2}$$

where n is the number of LC-ladder sections used in the network, L_i and C_i are the i^{th} inductor and capacitor values. The input impedance Z_{in} of the MN can be described [28] by:

$$Z_{in}(\omega_x) = \frac{Z_{load} * A(\omega_x) + B(\omega_x)}{Z_{load} * C(\omega_x) + D(\omega_x)} \tag{4.3}$$

where A, B, C and D are the values obtained in (4.2) and Z_{load} is the load resistance of the MN, typically 50 Ω for most applications. With the expression of (4.3), the input impedance at each frequency section of the MN can be obtained once the LC values are known.

The problem now resides in choosing proper LC values to ensure Z_{in} of the MN at each frequency section is inside the optimal impedance regions defined by (4.1). The MN should enable the device to achieve optimal performance across the whole bandwidth. Although some commercially available software such as ADS and AWR are useful in broadband impedance matching, the built-in optimizer is limited by high dimensional variables or strict optimization goals. Another solution is to use the Monte Carlo (MC) simulation to search all possible values of the LC components exhaustively, and then select the best LC values fulfilling the design requirements. The MC method requires massive calculation due to many possible LC value combinations to be examined.

Alternatively, the LC values can be obtained in a more efficient way as proposed in this chapter. The idea is inspired by a novel statistical approach referred to as the stochastic reduced order model (SROM) method [36]. Unlike MC, the SROM method only needs to examine a very small number of samples but produces the results almost as accurate as that of the MC method. The SROM method is applied to the Voronoi partition [29] which is a method divides the possible values of variables into several regions based on the statistical properties of the variables. Then, a sample at the centroid of each region is used to represent all the points in this region. An example is shown in Fig. 4-4. illustrating the Voronoi partition of a two-dimension variable. This method only looks at representative samples obtained using the Voronoi partition, but the effect is nearly equivalent to the MC method by checking all the possible samples. Hence, in this work, the Voronoi partition (the nucleus of the SROM method) is used to choose the LC values for MNs efficiently.

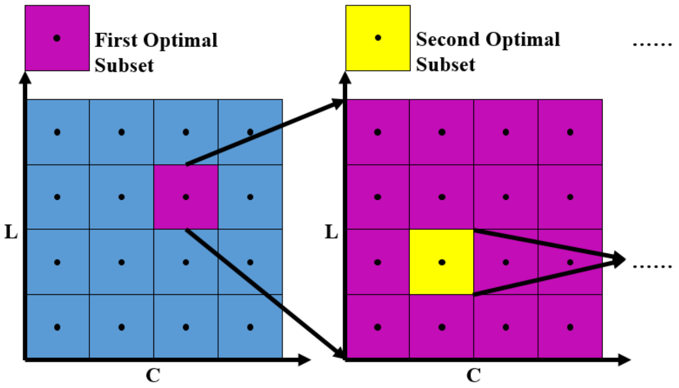

Fig. 4-4. A low-pass LC-ladder matching network with a DC block.

To perform the Voronoi partition, the input variable needs to be known beforehand. The dimension of the input variable is equal to the number of variables, e.g., the number of L and C components in the MN. In this way, each sample in the input variable contains a set of LC values for a possible realization of the MN. The Voronoi partition of the components values for the proposed MN can be realized in the following steps:

1) It can be assumed that the number of LC sections used in the MN is n (i.e., n inductors and n capacitors). Let X be an input variable with a dimension of 2n. Each dimension of X describes a set of component values (either L or C) in the circuit, i.e., $X = [L_1, L_2, \dots, L_n, C_1, C_2, \dots, C_n]$. The Voronoi partition of the input variable *X* with *2n* dimensions can be constructed as shown in Fig. 4-4 (a two-dimension diagram is shown as an example).
2) Divide the range of the possible *L* or *C* component values into m Voronoi regions for each dimension of *X*, based on the distribution in the variation range. Then select one sample at each section as a representative following the distribution of the component value between its upper and lower limits. The value of m can be heuristically chosen depending on the affordable number of trials. Theoretically, a greater value of m yields a higher probability of obtaining the optimum solution. In practice, the solution that meets the design requirement can be obtained even using a small value of *m*.
3) The *m* samples of *X* are obtained as the ith ($1 \le i \le m$) sample of X contains 2n values (i.e., from the ith sample of L_1 to the i^{th} sample of C_n). Each element in sample *(x(1), … , x(m))* should be the centroid of the ith Voronoi region [35]. Now, the infinite number of possible values for *X* is reduced to $2n \times m$ samples.
4) With the LC values in the obtained samples from Voronoi partition, equations (4.2) and (4.3) can be used to calculate the corresponding input impedance Zin (ω x) of each sample. The shortest Euclidean distance from the input impedance to the output power and PAE contour *dP(m)(*ω *x)* and dEff(m) *(*ω *x)* can be calculated. If $d_P^{(m)}(\omega_x)/r_P(\omega_x) \le 1$ and $d_{Eff}^{(m)}(\omega_x)/r_{Eff}(\omega_x) \le 1$, it indicates that the input impedances of the mth sample are in the optimal impedance regions over the desired band. The values in this sample can be used to synthesize the MN.
5) If no subset can meet the requirements, the shortest Euclidean distance from the input impedance to the optimal impedance region should be calculated. The matching quality of the sample can be evaluated by:

$$\Lambda^{(m)} = \sum_{i=1}^{k} \left| d_{in}^{(m)}(\omega_x) \right|^2 \tag{4.4}$$

where the $d_{in}^{(m)}(\omega_x)$ is the shortest Euclidean distance from the input impedance of the m^{th} sample at x^{th} frequency section to the corresponding optimal impedance region. The m^{th} sample that has the minimum $\Lambda^{(m)}$ will be selected as the optimum subset for further optimization. Repeat the Voronoi partition for the optimum subset as shown in Fig. 4-4 until the requirements are satisfied. If the requirements cannot be satisfied after repeating the partition, it indicates that the obligation cannot be met with the current order of the MN. Herein, it will be necessary to increase the order of the MN or decrease the lowest limits of the output power and/or PAE and start again from Step 1. A practical design procedure is shown in Section 4.3.

Using the proposed method, only $2n \times m$ samples need to be checked, which significantly reduces the calculation complexity. The solution of the LC values obtained using this method may not be the best one because the calculation cannot include every single possible combination of LC values. However, it is sufficient to obtain a solution that could ensure the input impedance at each frequency section is inside the corresponding optimal impedance region. An infinitely small separation of the LC value samples and an infinite order of the MN will offer a very accurate result, whereas the implementation will be very computationally intensive [36]. Consequently, the trade-off between accuracy and computation cost should be considered when determining the size of the separation and the number of iterations.

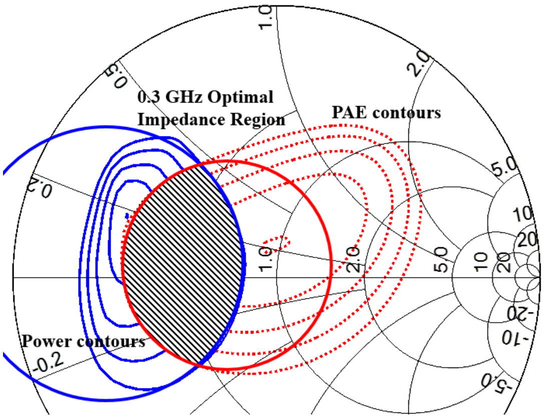
1.0
0.5
2.0
0.3 GHz Optimal
Impedance Region
PAE contours
0.2
5.0
10
20
1.0
2.0
5.0
10
20
-20
-10
Power contours
-0.2
-5.0

(a)

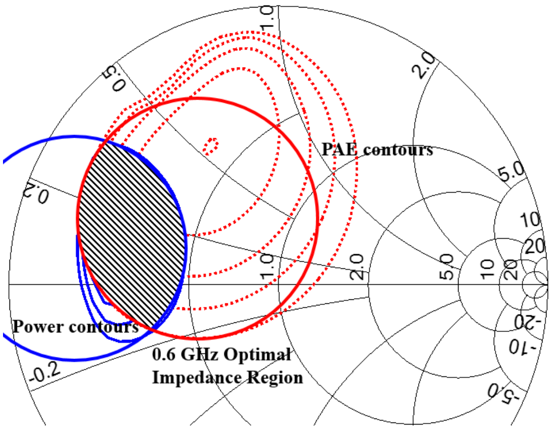
1.0
0.5
2.0
PAE contours
5.0
0.2
10
20
1.0
2.0
5.0
10
20
-20
-10
Power contours
0.6 GHz Optimal
Impedance Region
-0.2
-5.0

(b)

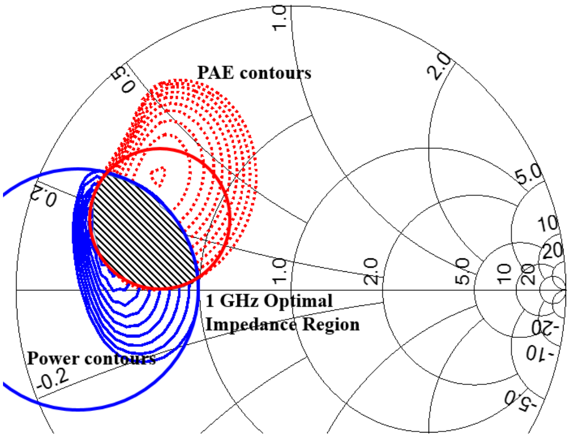
1.0
PAE contours
0.5
2.0
5.0
0.2
10
20
1.0
2.0
5.0
10
20
1 GHz Optimal
Impedance Region
-20
-10
Power contours
-0.2
-5.0

(c)

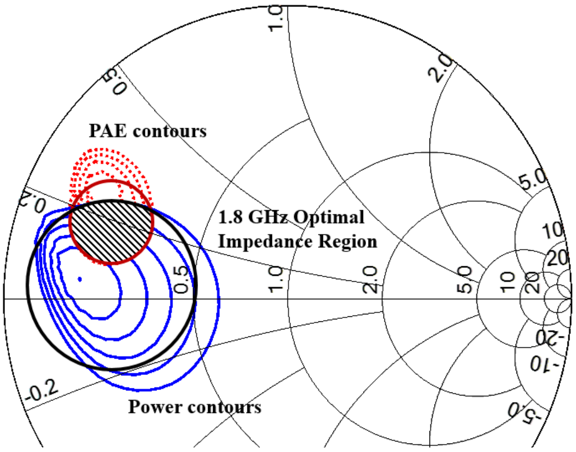

(d)

Fig. 4-5. The simulation results of optimal impedance regions at (a) 0.3 GHz, (b) 0.6 GHz, (c) 1 GHz, (d) 1.8 GHz.

4.3 Design and Implementation of the Matching Networks

In this section, a PA covering the frequency band of 0.2 GHz to 1.8 GHz is designed to verify the proposed method. The output power of the PA is expected to be higher than 42 dBm across the band, and the PAE at the 1 dB compression point is desired to be better than 60%.

4.3.1 Load-Pull Simulation

Gallium nitride (GaN) high electron mobility transistors (HEMTs) have been widely adopted in broadband high-efficiency PA designs [6], [16], [17], [25]. An unmatched 25-W Cree GaN HEMT CGH40025F is chosen for this PA design. This transistor has a breakdown voltage up to 84 V and a saturation drain current of 5.4 A. Intrinsic waveforms of the transistor are simulated by using CAD tools to investigate the operation of the transistor. The transistor is sealed in a Cree 400166 package. To minimize the parasitic effect introduced by the package, the intrinsic and extrinsic elements are calculated using the method provided in [6], [30]. These parasitic effects should be included in source-pull/load-pull simulations to predict the optimal impedance regions of the transistor.

The source-pull/load-pull simulation was carried out to find the optimal impedance. The simulation is performed using ADS with the transistor model provided by the manufacturer.

The device is biased at 28 V drain voltage and -3.2 V gate voltage (I_{DQ}=50mA). The input power is 30 dBm.

The desired operation bandwidth in this work is 0.2 GHz-1.8 GHz. The operational band is divided into 4 frequency sections as discussed and shown in Fig. 4-5. Then load-pull simulation is conducted to obtain the output power and PAE contours. The design goals require an output power higher than 42 dBm and a PAE better than 60% across the band. The optimal impedance regions which satisfy the design goals are defined using the method described in Section 4.2 and then extracted from the load-pull simulation as shown in Fig. 4-5. Then the method described in Section 4.2 was used to design the output matching network (OMN). The input matching network (IMN) can be designed via the same procedure.

4.3.2 OMN Design

This section presents details of the design and implementation of the OMN. Firstly, the order of the LC sections for the OMN should be determined [27]. A wider bandwidth and a greater range of impedance variations usually require higher order designs. On the other hand, a higher order matching network is typically lossier. The design process starts with the number of the LC sections n = 1. Then n is increased until the requirement is satisfied. It was found by calculation [27] that when n = 4 (for an eighth-order LC network), the impedance at each frequency section is inside the corresponding optimal impedance region. A 33-pF capacitor is added as a DC block at the end of the LC-ladder network and considered in the circuit optimization. The matching network circuit is shown in Fig. 4-3.

The Voronoi partition of the LC values are constructed as $\boldsymbol{X} = [L_1, L_2, \dots, L_n, C_1, C_2, \dots, C_n]$. To define the Voronoi partition, the elements of L and C are uniformly divided into several samples from 0 nH to 30 nH and 0 pF to 30 pF into 16 steps, respectively. The greatest values of the inductances and capacitances are high enough for the operational frequency range. The number of samples m is selected to be 16. Then the input impedance at each frequency section for all samples of LC combinations were computed by (4.2) and (4.3). Then an investigation was conducted to check whether the corresponding input impedances of the samples are inside the predefined optimal impedance regions. Since no sample can satisfy the design goal, the matching quality of was calculated by (4.4). The optimal subset with *X= [2 nH, 2 nH, 2 nH, 4 nH, 2 pF, 2 pF, 6 pF, 2 pF]* is found to have the best matching quality and selected for further optimization. The values of the selected optimal subset are divided again. The process was repeated until the matching requirements have been met.

For this design, the optimum subset containing the LC combination that satisfies the design goals has been found in the third-round Voronoi partition. All the three optimal subsets selected by the process are shown in Table I along with the corresponding LC element values. The input impedances realized by each optimal subset and the predefined optimal impedance regions are illustrated in Fig. 4-6 to Fig. 4-8. The input impedances of the second-round subset are inside the optimal impedance regions except for the impedance at 1.8 GHz. With the third-round optimal subset, the input impedance at each frequency section is constrained in the corresponding optimal impedance region, which will ensure that the design goals will be satisfied.

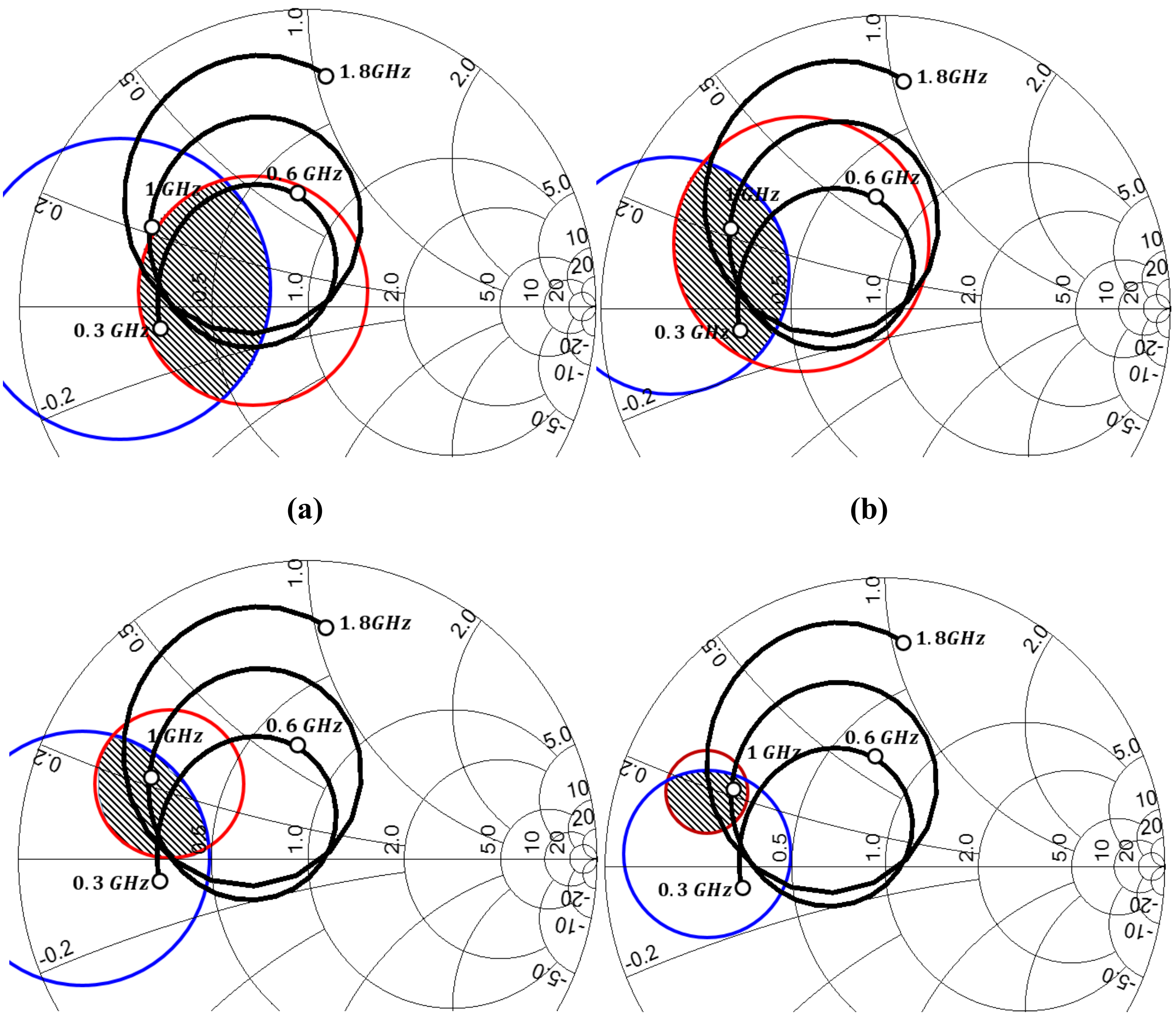

(a) (b)

(c) (d)

Fig. 4-6. The input impedance of the first optimal subset. (a) 0.3 GHz, (b) 0.6 GHz, (c) 1 GHz and (d) 1.8 GHz.

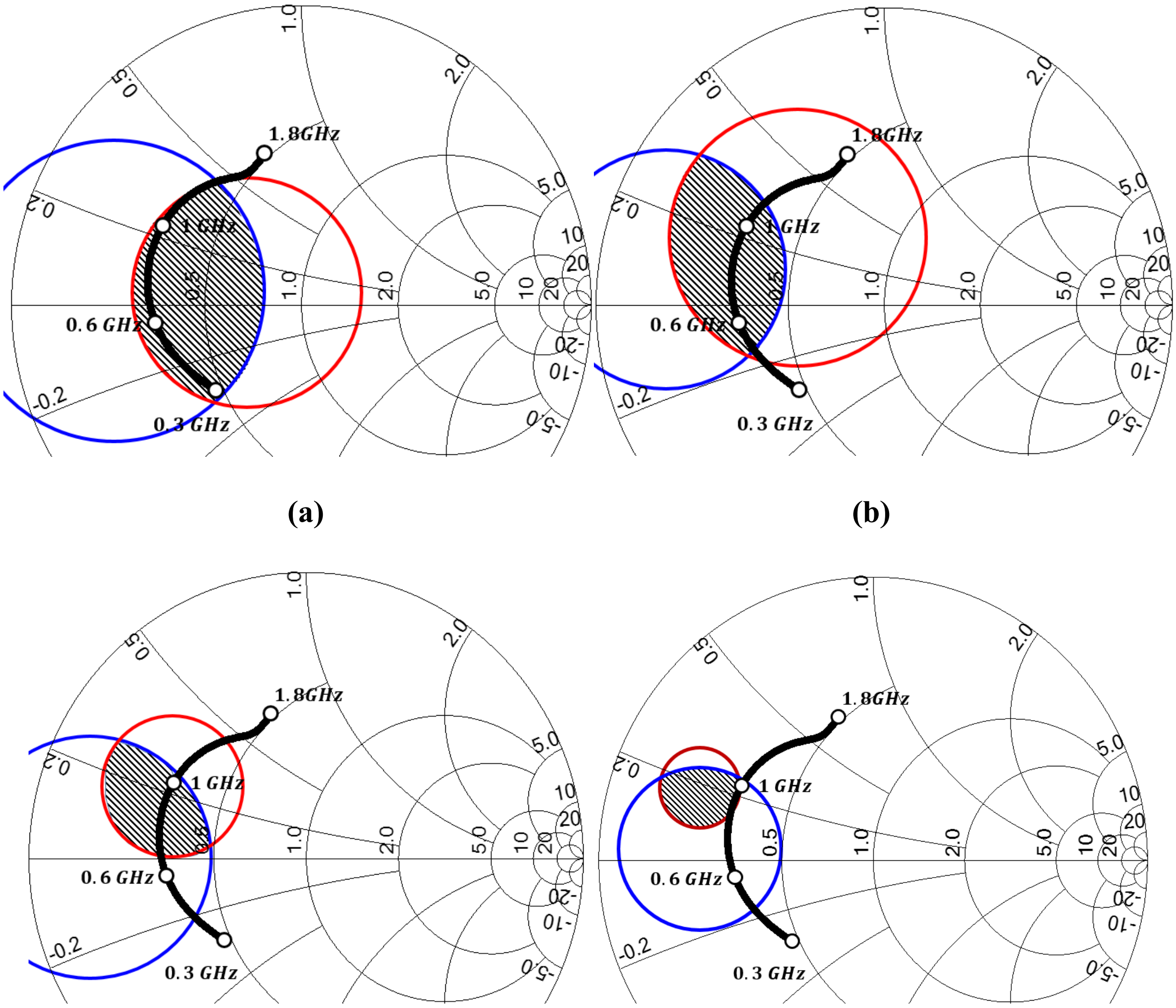

(a) (b)

(c) (d)

Fig. 4-7. The input impedance of the second optimal subset. (a) 0.3 GHz, (b) 0.6 GHz, (c) 1 GHz and (d) 1.8 GHz.

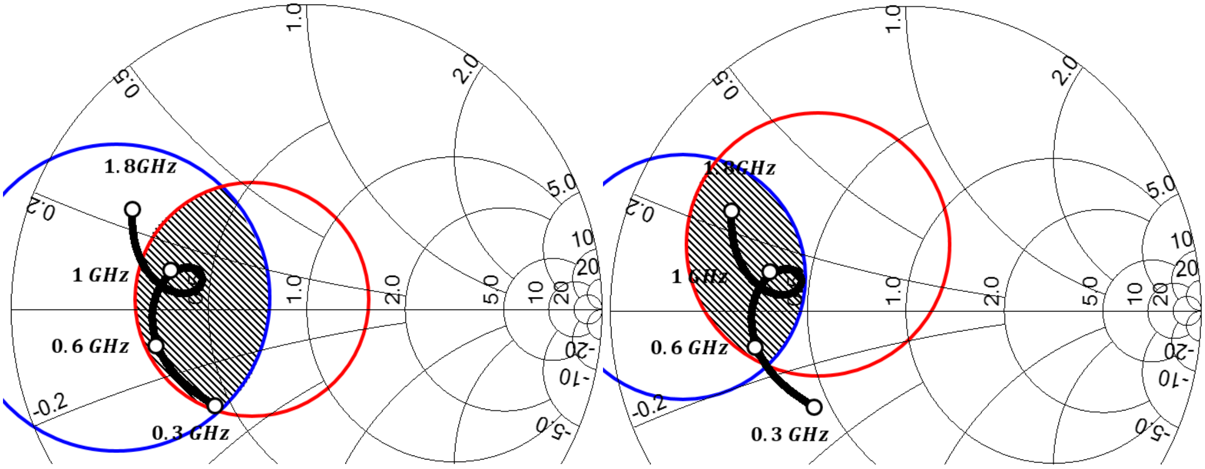

(a) (b)

TABLE I

VALUES OF LC ELEMENTS FOR EACH OPTIMAL SUBSET

Optimal Subset	L (nH)				C (pF)			
	L_1	L_2	L_3	L_4	C_1	C_2	C_3	C_4
1	2	2	2	4	2	2	6	2
2	1	2	2	4	1	2	5	2
3	0.5	1.6	1.9	4.6	1.1	2.6	4.6	2.7

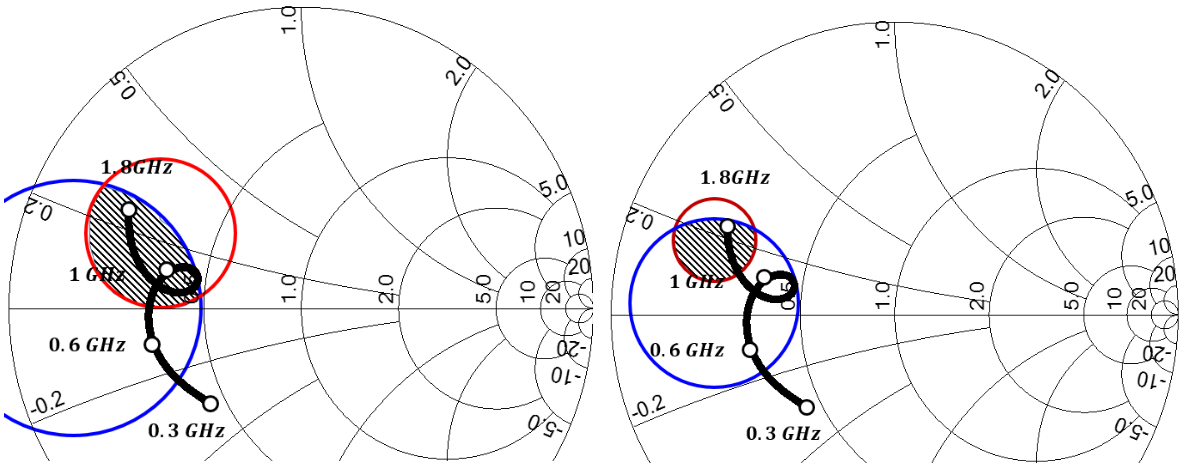

(c) **(d)**

Fig. 4-8. The input impedance of the third optimal subset. (a) 0.3 GHz, (b) 0.6 GHz, (c) 1 GHz and (d) 1.8 GHz.

4.3.3 OMN Implementation

Since the availability of high-quality inductors and capacitors to implement the design is quite limited, a distributed element version of the OMN is designed and fabricated. All the LC components are realized by transmission lines expect the DC block capacitor [28]. The inductors are implemented by high-impedance transmission lines while the capacitors are realized by low-impedance open stubs. It should be mentioned that the effects of shunt susceptance of the high-impedance lines and the series reactance of the low-impedance stubs should also be considered [34]. The lengths of inductive lines and capacitive open stubs should satisfy:

$$\omega L = Z_L \sin\left(\frac{2\pi l_L}{\lambda_{gL}}\right) + Z_C \tan\left(\frac{\pi l_C}{\lambda_{gC}}\right) \tag{4.5}$$

$$\omega C = Z_C \sin\left(\frac{2\pi l_C}{\lambda_{gC}}\right) + \frac{2}{Z_L}\tan\left(\frac{\pi l_L}{\lambda_{gL}}\right) \tag{4.6}$$

where L and C are the lumped element values for inductors and capacitors from Table I, λ_{gL} and λ_{gC} are the guided wavelengths for high-impedance transmission lines and open stubs respectively. They can be calculated by equations provided in [32]. The OMN is implemented on a Rogers 4350B substrate with a thickness of 1.52 mm, $\varepsilon_r = 3.48$ and a copper thickness of 35 µm. The realized distributed-element OMN was further optimized to achieve the pre-defined optimal performance. The implemented OMN layout and corresponding size are illustrated in Fig. 4-9. (a). The fabricated OMN is shown in Fig. 4-9. (b) and the comparison between the measured and simulated OMN input impedance is shown in Fig. 4-9. (c). A 50 Ω transmission line is cascaded to the DC-blocking capacitor to connect it to an SMA connector. For the IMN, the same procedure used to design and implement the OMN was used.

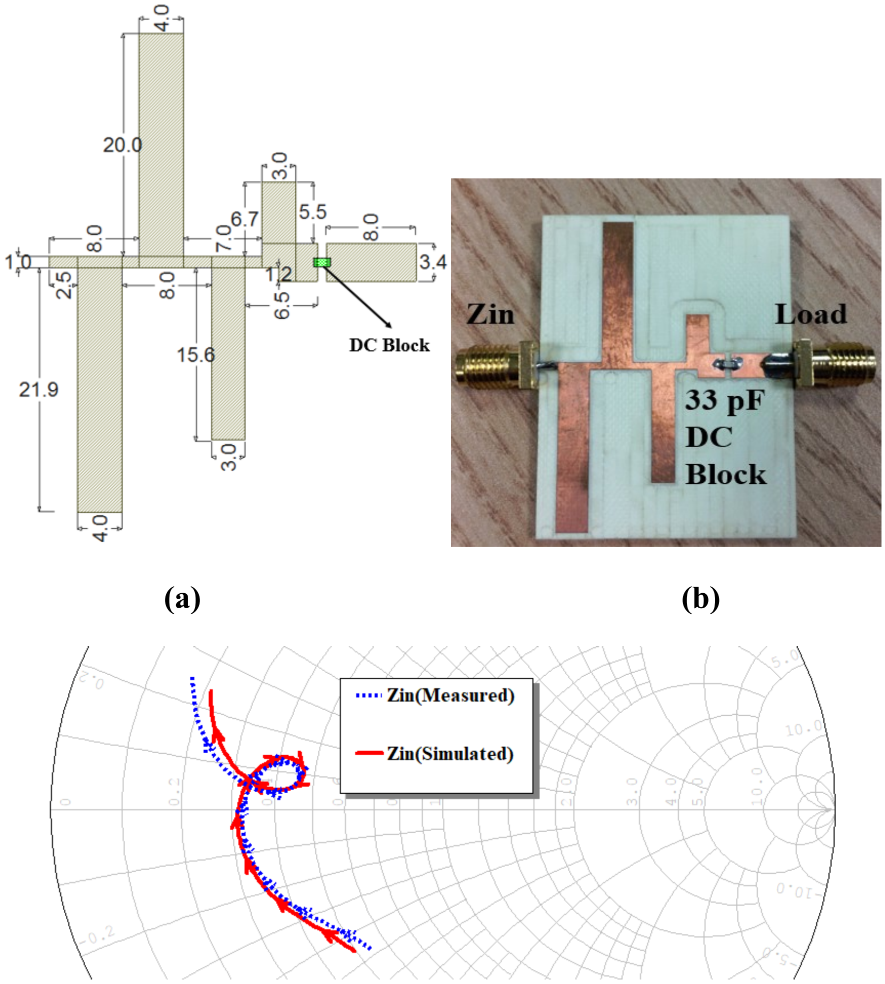

(a) **(b)**

(c)

Fig. 4-9. Output matching network. (a) Implemented OMN (b) fabricated OMN (c) comparison between the measured and simulated OMN input impedance.

4.4 PA Fabrication and Measurement Results

The PA is realized by connecting the IMN and OMN to the gate and the drain of the transistor, respectively. Importantly, the stability of the PA should be taken into consideration. DC power supplies for the gate and the drain of the transistor are connected by 22 nH inductors to prevent the leakage of RF into DC. A 100 Ω resistor is added in parallel with the inductor of the gate DC supply trail to improve the stability of the amplifier. A photograph of the fabricated PA and the measurement setup is shown in Fig. 4-10.

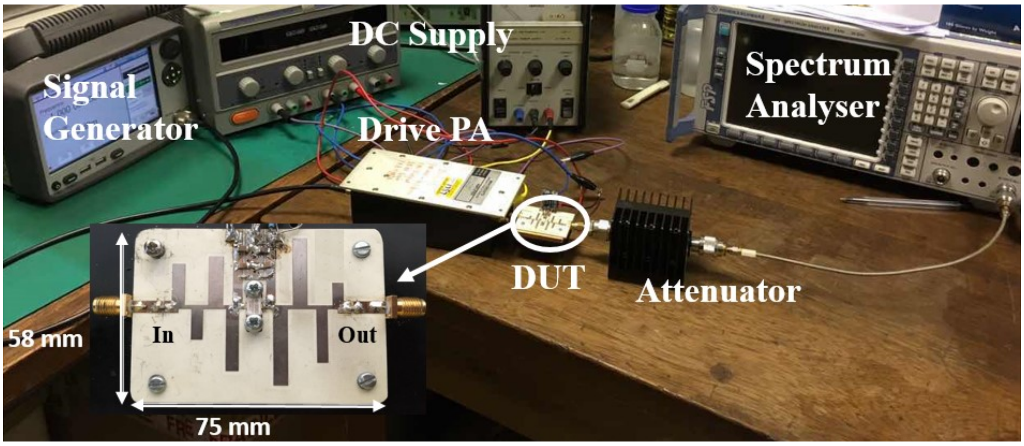

Fig. 4-10. Photo of the fabricated PA and measurement setup.

The simulated voltage and current waveforms on the intrinsic drain at 0.6 GHz and 1.3 GHz are shown in Fig. 4-11. The input power level is 30 dBm. The overlap between the voltage and current is relatively small which indicates that the PA can achieve high-efficiency performance. It can be seen that the operation modes of the PA at different frequency are not identical which may be caused by the harmonic reflection. For 0.6 GHz, the harmonics are still in the band of interest, while the harmonics of 1.3 GHz have been filtered by the MN. Therefore, the waveforms at 0.6 GHz are square wave like, while the waveforms at 1.3 GHz are sinewave.

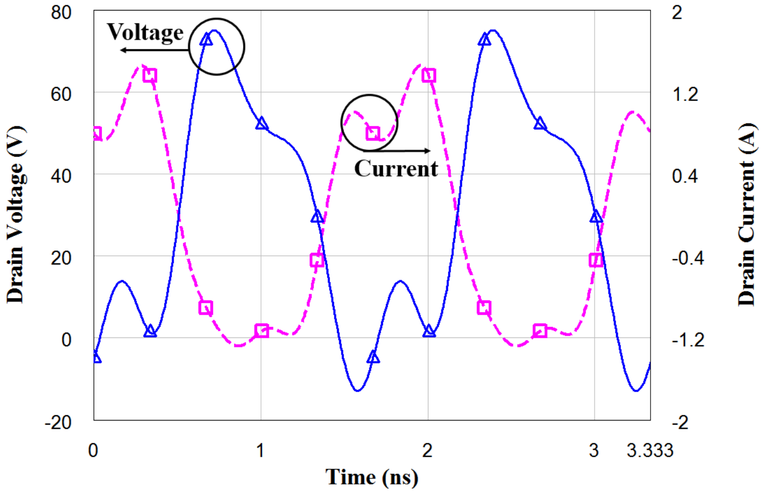

(a)

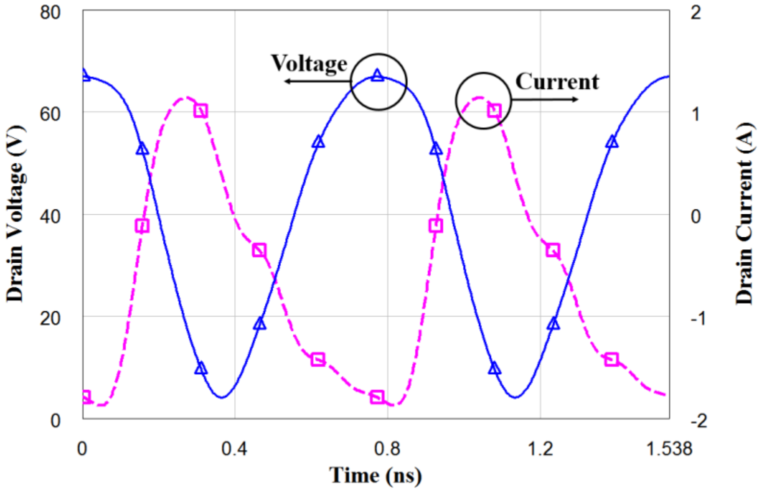

(b)

Fig. 4-11. Simulated voltage and current drain waveform at (a) 0.6 GHz (b) 1.3 GHz.

The fabricated PA has been measured with a continues-wave (CW) signal to examine the large signal performance. A single-tone signal was generated by a Keithley 2920 RF signal generator. Due to that the input power required by the PA is up to 32 dBm, a buffer amplifier was used to boost the input power. The output power of the designed PA was measured using a power meter (Rohde & Schwarz NRP-Z85).

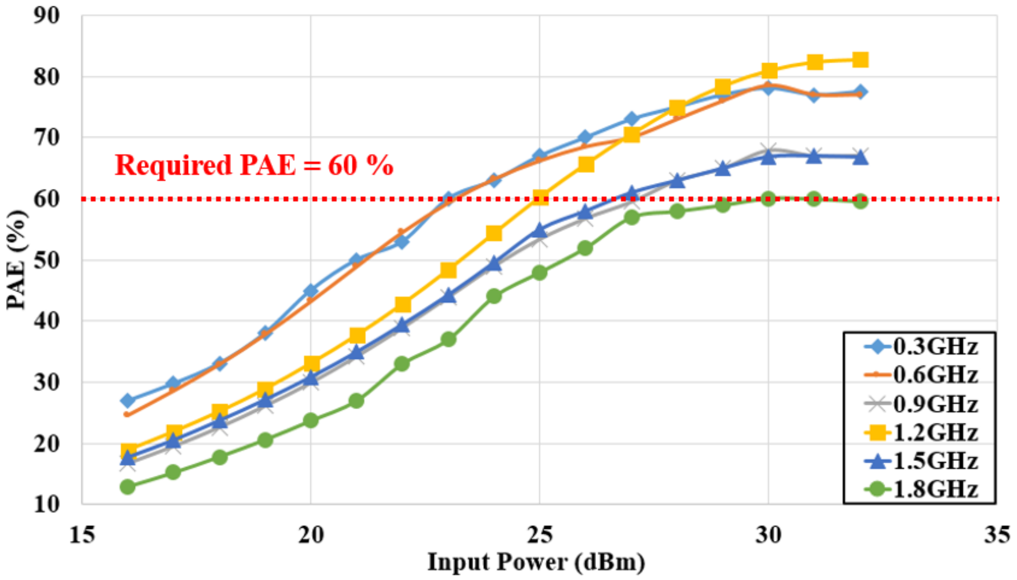

Fig. 4-12. Measured PAE versus input power at 0.3, 0.6, 0.9, 1.2, 1.5 and 1.8 GHz.

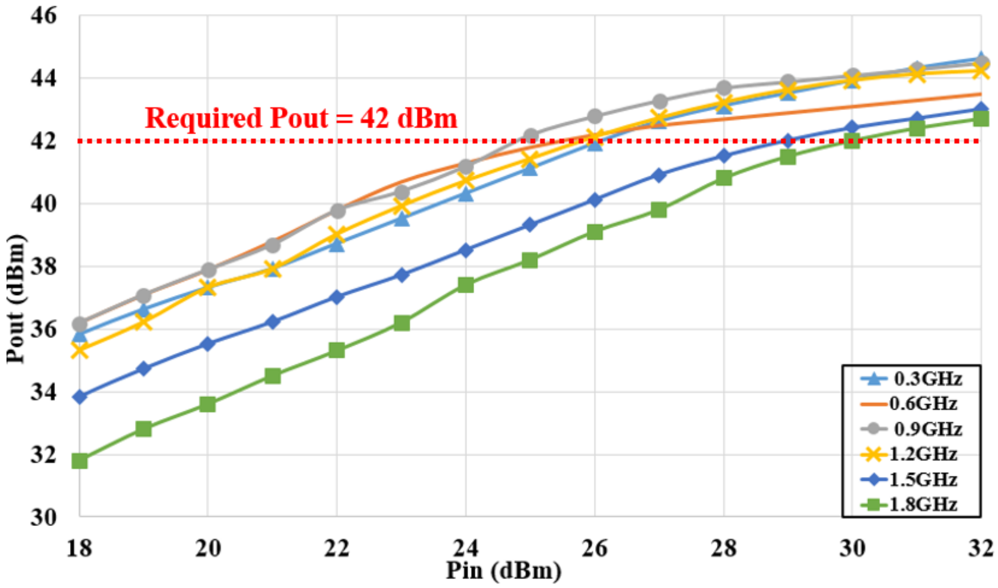

Fig. 4-13. Measured output power versus input power at 0.3, 0.6, 0.9, 1.2, 1.5 and 1.8 GHz.

The PA was designed to achieve a PAE better than 60% and an output power higher than 42 dBm from 0.2 GHz to 1.8 GHz. To verify the proposed design method, the PA is firstly measured across the band with 28 V drain voltage, -3.2 V gate voltage and a sweeping input power. The measured PAE and output power are illustrated versus the input power in Fig. 4-12. and Fig. 4-13. respectively. It can be seen in Fig. 4-13. that the output has a trend of being compressed when the input power is greater than 28 dBm and the corresponding PAE is also saturated as shown in Fig. 4-12. The design requirement of a PAE better than 60% and the output power higher than 42 dBm can be achieved simultaneously with an input power of 30 dBm.

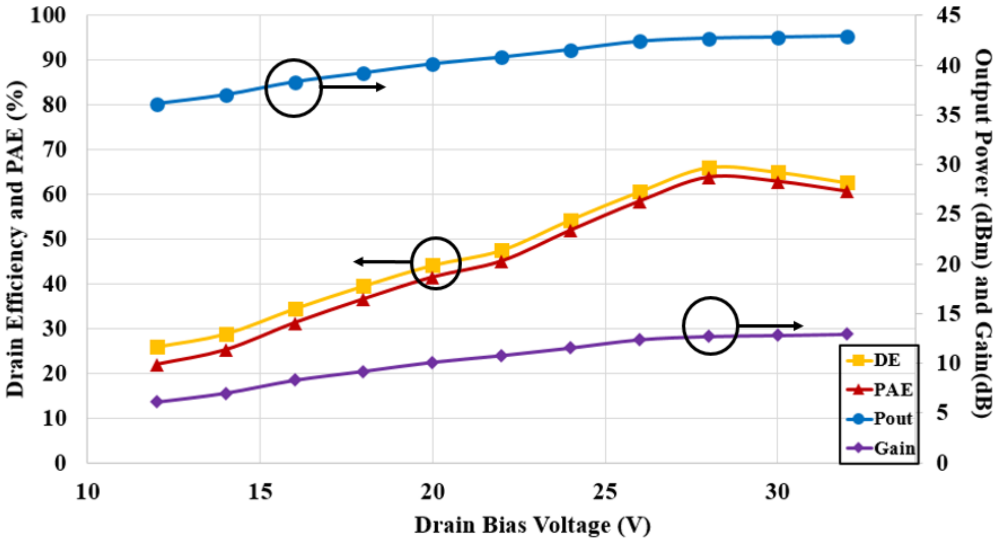

Fig. 4-14. Measured drain efficiency, PAE, output power and gain versus drain voltage at 1.3 GHz.

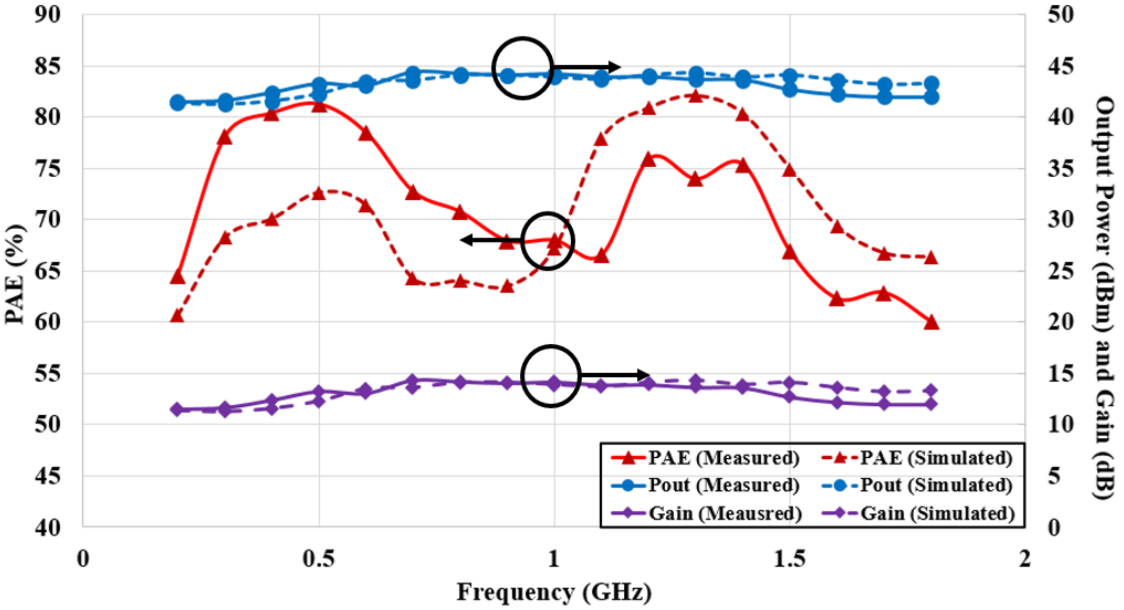

Fig. 4-15. Comparison between the measured and simulated PAE, gain and output power (VDS=28 V, VGS=-3.2 V and PIN=30 dBm).

Then the PA is measured by sweeping the drain voltage while fixing the input power and the gate voltage at 30 dBm and -3.2 V, respectively. Fig. 4-14. shows the measured result of PAE, output power and gain versus drain voltage at 1.3 GHz. The maximum PAE (74%) is achieved at 28 V drain voltage.

The comparison between the measured and simulated gain, PAE and output power is illustrated in Fig. 4-15. It can be observed that the measured PAE has two peaks which agree with the simulation. The measured PAE is higher than that of the simulation at lower frequencies 0.2-0.9 GHz and is lower at higher frequencies 1.1-1.8 GHz. The difference between the measured and simulated PAE over the band is less than 10%. Also, the trend of simulated and measured output power is consistent with a difference of less than 1.5 dB. This work has achieved the state-of-the-art performance in terms of bandwidth and efficiency. The comparison with similar broadband PAs is shown in Table II. This PA has achieved a PAE of 60-82%, an output power of 42-45 dBm (16-32 W) and a gain of 12-15 dB over a frequency band from 0.2-1.8 GHz. This PA has a much wider operational bandwidth compared to those PA with similar efficiency performance, and a higher efficiency compared with those with similar bandwidths. The PA in [6] has achieved a similar efficiency. However the fractional bandwidth is only 84% (f_H:f_L=2.4:1). The proposed work can achieve the same level of efficiency with a bandwidth of 160% (f_H:f_L=9:1). To my best knowledge, no other work has achieved high efficiency with such a wide bandwidth. The achieved operation bandwidth and efficiency of this design are better than all other work reported so far.

TABLE II

PERFORMANCE OF STATE-OF-THE-ART BROADBAND HIGH-EFFICIENCY PAS

Ref.	Frequency (GHz)	FBW, f_H:f_L	Gain (dB)	P_{out} (W)	Efficiency (%)
[23]	1.9-4.3	78%, 2.3:1	9-11	10-15	57-72*
[2]	0.36-0.79	81%, 2.2:1	5-14	10	30-81^
[6]	0.9-2.2	84%, 2.4:1	10-13	10-20	63-89*
[12]	1.3-3.3	87%, 2.5:1	10-13	10-11	59-79^
[25]	0.9-3.2	112%, 3.6:1	10-14	9.1-20.4	52-85^
[26]	0.8-4	133%, 5.0:1	5-7	1-2	40-55*
This work	0.2-1.8	160%, 9.0:1	12-15	16-32	60-82^

*: Drain Efficiency， ^: Power Added Efficiency

The bandwidth is defined based on the lowest PAE achieved in this table.

4.5 Conclusion

Owing to the variation of optimal impedances for high PAE across a wide bandwidth, the design methods of matching networks reported in the literature require an initial guess, data training or complex optimization algorithms which significantly increase the design difficulty. This chapter has presented a general method to design frequency varying impedances matching networks which can be applied to the design of broadband high-efficiency PAs. The wide frequency band has been divided into several frequency sections based on the optimal impedance over the band. The optimal source and load impedances for a transistor have been defined by optimal impedance regions at different frequency sections, instead of a fixed value at the centre of the desired band. A low-pass LC-ladder network has been applied to match the predefined optimal impedance regions. The simplification of the design and optimization of the matching networks have been made possible by using the SROM and Voronoi partition.

The designed PA has been fabricated and measured to validate the proposed method. The large signal experimental results have shown a PAE of 60-82%, a gain of 12-15 dB and an output power between 42-45 dBm (16-32 W) over a 160% fractional bandwidth from 0.2 GHz to 1.8 GHz. The state-of-the-art performance is better than any previously reported work. The results have demonstrated the potential of the proposed method to design high-performance amplifiers for future communication systems.

4.6 References

[1] N. O. Sokal and A. D. Sokal, “Class E—A new class of high-efficiency tuned single-ended switching power amplifiers,” *IEEE J. Solid-State Circuits.*, vol. SSC-10, no. 3, pp. 168–176, Mar. 1975.

[2] J. Zhou, K. A. Morris, G. T. Watkins and K. Yamaguchi, “Improved reactance-compensation technique for the design of wideband suboptimum class-E power amplifiers,” *IEEE Trans. Microw. Theory Techn.*, vol. 63, no. 9, pp. 2793–2801, Sep. 2015.

[3] F. H. Raab, “Broadband class-E power amplifier for HF and VHF,” in *IEEE MTT-S Int. Microw. Symp. Dig.*, Jun. 11–16, 2006, pp. 902–905.

[4] K. Narendra and Y. K. Tee, “Optimized high-efficiency class E RF power amplifier for wide bandwidth and high harmonics suppression,” *IET Circuits, Devices, Syst.*, vol. 60, no. 10, pp. 1–13, Feb. 2014.

[5] F. J. Ortega-Gonzalez, D. Tena-Ramos, M. Patino-Gomez, J. M. Pardo-Martin, and D. Madueno-Pulido, “High-power wideband L-band suboptimum class-E power amplifier,” *IEEE Trans. Microw. Theory Techn.*, vol. 61, no. 10, pp. 3712–3720, Oct. 2013.

[6] K. Chen and D. Peroulis, “Design of highly efficient broadband class-E power amplifier using synthesized low-pass matching networks,” *IEEE Trans. Microw. Theory Techn.*, vol. 59, no. 12, pp. 3162–3173, Dec. 2011.

[7] J. Zhou, K. Morris, G. Watkins, and K. Yamaguchi, “Wideband class-E power amplifier covering the whole UHF broadcast band,” in *Eur. Microw. Conf.*, Nuremberg, Germany, 2013, pp. 1307–1310.

[8] A. J. Wilkinson, J. K. A. Everard, “Transmission-line load network topology for class-e power amplifiers,” *IEEE Trans. Microw. Theory Techn.*, vol. 49, no. 6, pp. 1202–1210, Jun. 2001.

[9] H. Ma, R. van der Zee, B. Nauta, "Design and analysis of a high-efficiency high-voltage class-D power output stage", *IEEE J. Solid-State Circuits*, vol. 49, no. 7, pp. 1514-1524, Jul. 2014.

[10] L. Guo, T. Ge, J. S. Chang, "A 101 dB PSRR 0.0027% THD + N and 94% power-efficiency filterless Class D amplifier", *IEEE J. Solid-State Circuits*, vol. 49, no. 11, pp. 2608-2617, Nov. 2014.

[11] N. Tuffy, L. Guan, A. Zhu, and T. Brazil, “A simplified broadband design methodology for linearized high-efficiency continuous class-F power amplifiers,” *IEEE Trans. Microw. Theory Techn.*, vol. 60, no. 6, pp. 1952–1963, Jun. 2012.

[12] K. Chen and D. Peroulis, “Design of broadband highly efficient harmonic-tuned power amplifier using in-band continuous class-F-1/*f* mode transferring,” *IEEE Trans. Microw. Theory Techn.*, vol. 60, no. 12, pp. 4107–4116, Dec. 2012.

[13] M. Yang, J. Xia, Y. Guo and A. Zhu, "Highly efficient broadband continuous inverse class-F power amplifier design using modified elliptic low-pass filtering matching network," *IEEE Trans. Microw. Theory Techn.*, vol. 64, no. 5, pp. 1515–1525, May. 2016.

[14] J. H. Kim, G. D. Jo, J. H. Oh, Y. H. Kim, K. C. Lee and J. Jung, "Modeling and design methodology of high-efficiency class-F and class-F-1 power amplifier," *IEEE Trans. Microw. Theory Techn.*, vol. 59, no. 1, pp. 153–165, Jan. 2011.

[15] A. Sheikhi, M. Hayati and A. Grebennikov, "A design methodology of class-E/F3 power amplifier considering linear external and nonlinear drain-source capacitance," *IEEE Trans. Microw. Theory Techn.*, vol. 65, no. 2, pp. 548–554, Feb. 2017.

[16] R. Tong, S. He, B. Zhang, Z. Jiang, X. Hou, and F. You, "A novel topology of matching network for realizing broadband high efficiency continuous class-F power amplifiers," in *Eur. Microw. Integr. Circuits Conf.*, pp. 504–507, Oct. 2013.

[17] G. Sun and R. Jansen, "Broadband Doherty power amplifier via real frequency technique," *IEEE Trans. Microw. Theory Techn.*, vol. 60, no. 1, pp. 99–111, Jan. 2012.

[18] M. Akbarpour, F. M. Ghannouchi and M. Helaoui, "Current biasing of power amplifier transistors and its application for ultra-wideband high efficiency at power back-off," *IEEE Trans. Microw. Theory Techn.*, vol. 65, no. 6, pp. 2192–2200, June. 2017.

[19] A. Barakat, M. Thian, V. Fusco, S. Bulja and L. Guan, "Toward a more generalized Doherty power amplifier design for broadband operation," *IEEE Trans. Microw. Theory Techn.*, vol. 65, no. 3, pp. 846-859, March. 2017.

[20] W. H. Doherty, "A new high efficiency power amplifier for modulated waves," *Proceedings of the Institute of Radio Engineers.*, vol. 29, no. 9, pp.1163–1182, Sep. 1936.

[21] B. Kim, J. Kim, I. Kim and J. Cha, "The Doherty power amplifier," *IEEE Microwave Magazine.*, vol. 7, no. 5, pp. 1527-3342, Oct. 2006.

[22] Y. Zhuang, J. Zhou, Y. Huang and A. Chen, "Design of a broadband high efficiency GaN power amplifier for GNSS applications," *IEEE MTT-S International Wireless Symposium,* 2016.

[23] P. Saad, C. Fager, H. Cao, H. Zirath, and K. Andersson, "Design of a highly efficient 2–4-GHz octave bandwidth GaN-HEMT power amplifier," *IEEE Trans. Microw. Theory Tech.*, vol. 58, no. 7, pp. 1677–1685, Jul. 2010.

[24] D. Dawson, "Closed-form solutions for the design of optimum matching networks," *IEEE Trans. Microw. Theory Tech.,* vol. 57, no. 1, pp.121-129, Jan. 2009.

[25] Z. Dai, S. He, F. You, J. Peng, P. Chen and L. Dong, “A New Distributed Parameter Broadband Matching Method for Power Amplifier via Real Frequency Technique,” *IEEE Trans. Microw. Theory Tech*., vol. 63, no. 2, pp. 449–458, Feb. 2015.

[26] P. Colantonio, F. Giannini, R. Giofre, and L. Piazzon, “High-efficiency ultra-wideband power amplifier in GaN technology,” *Electron. Letter.,* vol. 44, no. 2, pp. 130–131, Jan. 2008.

[27] G. L. Matthaei, “Tables of Chebyshev impedance-transformation networks of low-pass filter form,” *Proc. IEEE*, vol. 52, no. 8, pp. 939–963, 1964.

[28] P. L. D. Abrie, *The design of impedance-matching networks for radio-frequency and microwave amplifiers*, Dedham, MA: Artech House, 1985.

[29] Q. Du, V. Faber and M. Gunzburger, “Centroidal voronoi tessellation: applications and algorithms,” *SLAM Review*, vol. 41, no. 4, pp. 637-676. Oct. 1999.

[30] G. Dambrine, A. Cappy, F. Heliodore, and E. Playez, “A new method for determining the FET small-signal equivalent circuit,” *IEEE Trans. Microw. Theory Tech.*, vol. 36, no. 7, pp. 1151–1159, Jul. 1988.

[31] D. C. Fielder, "Numerical determination of cascaded LC network elements from return loss coefficients", *IRE Trans. Circuit Theory.*, vol.CT-5, pp. 356-359, Dec. 1958.

[32] J.S.Hong, “Microstrip filter for RF/microwave applications”. Hoboken, N.J.: Wiley, 2011, ISBN 9780470937280 (e-book)

[33] J. Rollett, “Stability and power-gain invariants of linear twoports,” *IEEE Trans. Circuit Theory*., vol. 9, no. 1, pp. 29–32, Mar. 1962.

[34] S. Sarkar, J. E. Warner, W. Aquino, and M. Grigoriu, “Stochastic reduced order models for uncertainty quantification of intergranular corrosion rates,” *Corrosion Science*, vol. 80, pp. 257-268, Mar. 2014.

[35] Z. Fei, Y. Huang, J. Zhou and C. Song, “Numerical analysis of a transmission line illuminated by a random plane-wave field using stochastic reduced order models,” *IEEE Access.*, vol. PP, no. 99, pp. 1–10, 2011.

[36] M. Grigoriu, “Reduced order models for random functions. Application to stochastic problems,” *Applied Mathematical Modelling*, vol. 33, no. 1, pp. 161-175, Jan. 2009.

[37] P. Chen, B. M. Merrick, and T. J. Brazil, “Bayesian optimization for broadband high-efficiency power amplifier designs.,” *IEEE Trans. Microw. Theory Techn*., vol. 63, no. 12, pp. 4263–4272, Dec. 2015.

[38] B. S. Yarman and H. J. Carlin, “A simplified real frequency technique applied to broadband multistage microwave amplifiers,” *IEEE Trans. Microw. Theory Techn*., vol. MTT-30, no. 12, pp. 2216–2222, Dec. 1982.

[39] B. S. Yarman, Metin Sengul and Ali Kilinc, “Design of practical matching networks with lumped elements via modeling.,” *IEEE Transaction on Circuit and System I: regular papers.*, vol. 54, no. 8, pp. 1829–1837, Aug. 2007.

Chapter 5 **Improving Energy Extraction from AC Power Lines Under Magnetic Saturation**

This chapter presents a novel design method for energy scavenging from AC power lines by using a current transformer-based energy harvester under its magnetic saturation condition. The extracted power level of a conventional magnetic field energy harvester is limited by the maximum flux density of the magnetic core. When the magnetic core is clamped on AC power lines, the flux density of the core is proportional to the magnitude of the magnetic field strength around the power line. The flux density could reach its maximum value when the magnetic field increases. In this scenario, very little energy can be harvested since there is little flux density variation. Here we introduce an artificial magnetic field to manipulate the dominant magnetic field of power lines. The core will not be easily driven into the saturation region, hence more energy can be harvested. An additional control coil is added to the harvester. A power management circuit is employed to store the energy harvested by the control coil and feed it back to the harvester to generate a counter magnetic field. As a result, the magnetic flux density in the core will not be saturated. More energy can then be harvested. Experimental results of the proposed energy harvester prototype show that an average power of 283 mW on a 10 A power line is achieved which is increased by 45% compared with the conventional device. This design could be a promising solution for powering the smart grid monitoring devices and other industrial sensing applications.

5.1 Magnetic Field Energy Harvesting

Energy harvesting (EH) is a technique that capturing the energy stored in the ambient environment that in the form of wind, solar, vibration, electromagnetic waves, etc. The energy can be scavenged and stored to power electronic devices instead of the batteries. Hence, the EH technique has advantages of being maintenance free as the electronic devices can be self-powered to eliminating the battery replacement. EH is also environmentally friendly as the usage of batteries which contain chemicals and metals that are harmful to the environment can be significantly reduced [1] – [3]. For the power transmission and distribution systems, there exist many ambient energy sources such as solar, wind, electrical field and magnetic field especially in electrical substations or under electricity pylons. The wireless sensor nodes used for the power transmission systems monitoring can be powered by harvested energy instead of batteries. Solar power is a good source for harvesting the energy in the daytime with the good weather [4], [5]. Due to the dependency on the weather condition a large energy storage should be used which could be expensive. On the other hand, the wind energy is also relying on the weather conditions. In particular, around the high voltage equipment in power transmission systems, there exist strong electromagnetic fields which are stable as long as the power transmission system is operating. Hence, it will be a consistent and reliable energy source for driving the sensors.

5.1.1 Theory and Impedance Matching Challenges Analysis

The main EH techniques used for power transmission system are the electric field and magnetic field harvesting. The electric field is caused by the voltage of high power equipment (electric charges). Therefore, the electric field energy around the power equipment is stable regardless of the load demand. There is much research dedicated in electric field EH reported in the literature [6] – [12]. However, the electric field energy harvesters are limited because the required capacitance is usually very large to harvest high-power up to mW level [13]. The capacitance of a typical electric field EH circuit is usually in pF level, requiring a Mega Hennery inductor to resonate at 50/60 Hz, which is not commercially available. Hence, the electric field method is only suitable for very low power applications or applicable when the power transmission line is conducting very high voltage up to 100kV [11].

The magnetic field generated by the AC current conducting lines as shown in Fig. 5-1 can be used for EH efficiently.

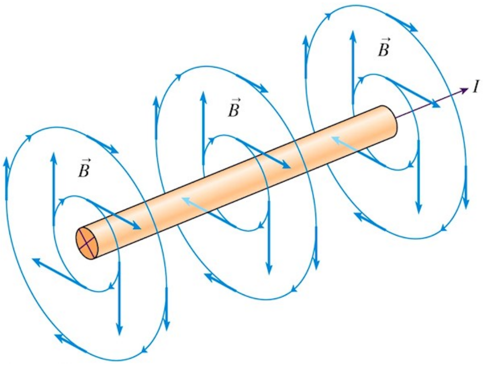

Fig. 5-1. AC current conducting lines and the surrounding magnetic field.

Based on Faraday's Law, a coil with N turns and a cross-section area A enclosed in a time-varying magnetic field with a magnetic flux density B_{core}, the voltage can be induced as:

$$V_{coil} = NA\frac{dB_{core}}{dt} \tag{5.1}$$

where the magnetic flux density can be calculated by the magnetic field strength H_{EX}, permeability of the free space μ_0 and the effective permeability of the core μ_{eff} as:

$$B_{core} = \mu_0 \mu_{eff} H_{EX} \tag{5.2}$$

Thus, the magnetic field energy harvester will extract more energy with higher μ_{eff} and higher H_{EX}. Therefore, lots of works have been reported using a high permeability core to improve the harvested power level [14] – [17]. However, it should be stressed that the bottleneck of improving the magnetic field EH power is that the permeability of the core will change with the magnitude of the magnetic field strength. Thus, the magnetic flux density and the magnetic field strength will have a relationship as shown in Fig. 5-2:

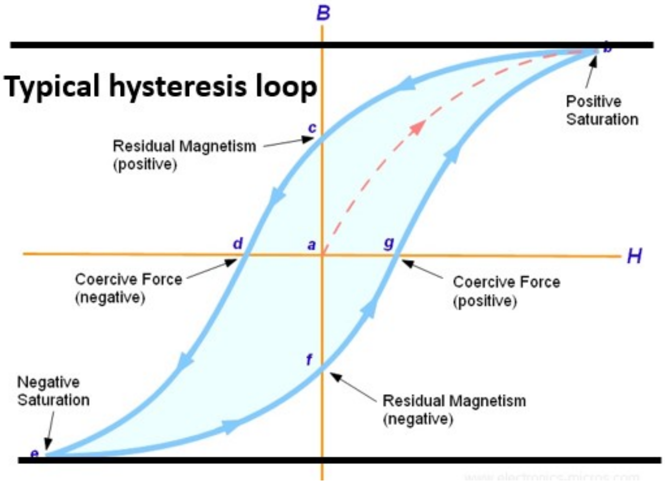

Fig. 5-2. Typical B-H loop.

It can be observed that there are two boundaries which limit the maximum positive and negative magnetic flux density in the core regardless of the magnetic field strength. The boundary of the magnetic flux density *Bsat* is determined by the physical features of the material [15]. For a core clamped on a power line, when the conducting current is zero, each crystal in the core has a magnetic domain which is randomly oriented initially. When the current in the power line increases, a magnetic field is applied to the core which will re-orient the magnetic domains of some crystal in the direction of the external field. A higher *H* will align more domains until the core is magnetic saturated. A large amount of energy can be extracted when a core is in non-saturation region. When the current in the power line keeps increasing, almost all the domains will be aligned with the external *H*. The magnetic flux density will almost keep constant at B_{sat}. The ferromagnetic material is said to be saturated when the magnetic flux density reaches B_{sat}. In the saturation region, there is no more flux change in the core regardless of the magnitude of the current. The magnetic field energy harvester is modelled as a transformer with a resistive load as shown in Fig. 5-3:

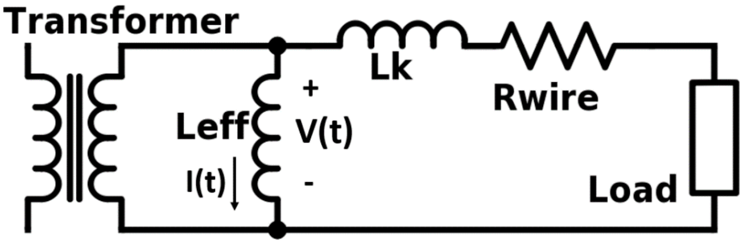

Fig. 5-3. Equivalent circuit model of the magnetic field energy harvester [19].

The voltage on the load can be calculated as:

$$V(t) = \frac{dFlux(t)}{dt} = \frac{d}{dt}[B_{sat} \cdot \frac{2}{\pi} \arctan(\frac{N}{\alpha} I(t))]$$

$$= B_{sat} \cdot \frac{2}{\pi} \cdot (\frac{\alpha N}{\alpha^2 + N^2 I(t)^2}) \frac{dI(t)}{dt} \tag{5.3}$$

The voltage on the load and the power line current in the time domain with magnetic saturation can be plotted as Fig. 5-4:

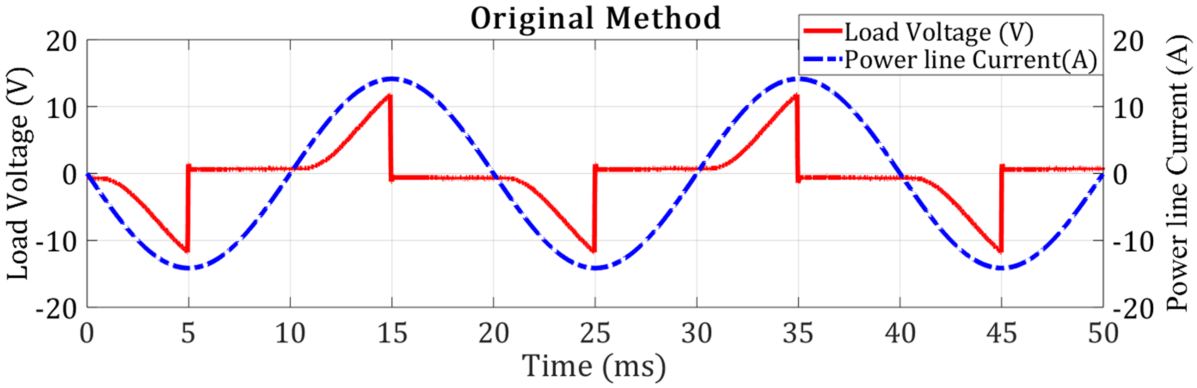

Fig. 5-4. Load voltage and power line current relationship in the time domain [20].

For almost a half of the current cycle, the voltage on the load is near zero. This is caused by the parallel inductance behaves like a short circuit when the current magnitude in the power line is high enough to drive the core into saturation. The effective inductance and the current in power line can be expressed as Fig. 5-5:

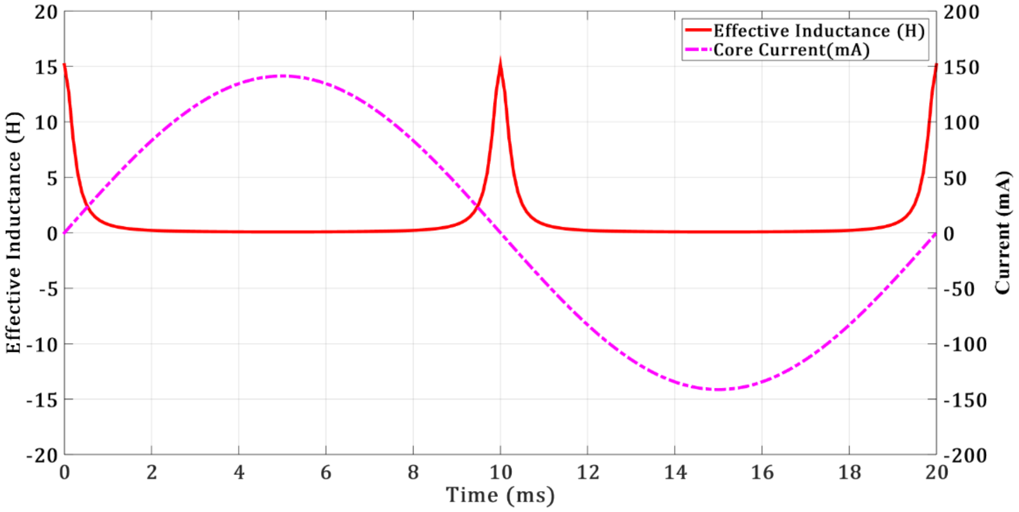

Fig. 5-5. Load voltage and power line current relationship in the time domain [20].

The periodic near-zero behaviour of the inductor will cause a time-domain variation of the impedance seen by the circuit, leading to a mismatch and limiting the harvested power level. Hence, to improve the harvested power of magnetic field energy harvester, the impedance variation caused by the magnetic core saturation should be solved. In the literature, there are mainly two directions in solving this problem, namely techniques for preventing the magnetic core saturation and methods on actively matching the circuit with saturation.

5.1.2 Matching Methods with Magnetic Flux Saturation

In [13], the authors selected three toroid coils with different materials (ferrite, iron powder and nanocrystalline alloy) to clamp on the same current conductor. From the experimental results, they concluded the nanocrystalline alloy was the best material due to its high permeability and high saturation flux density. They used a cylindrical core with the outer diameter *OD* of 33.5 mm, inner diameter *ID* of 27.5 mm and the height *H* of 4 mm. Finally, 9 mW can be collected when it is mounted on a 5 A conductor which gives a power density of 7.8 µW/cm^3. However, their results are based on the experiment without a theoretical analysis of the saturation problem.

Roscoe *et al* [14] used cylindrical ferrite cores (*OD* = 22 mm, *ID* = 17 mm, *H* = 6 mm) to clamp on a conductor which carries a current of 50 A at 50 Hz, through which a power of 170 mW can be collected. They selected the ferrite material with low relative permeability ($\mu_r = 2000$) to avoid the magnetic flux saturation. However, as shown in Fig. 5-6, when the current becomes bigger, the ferrite core will still be saturated, leading to significant energy losses.

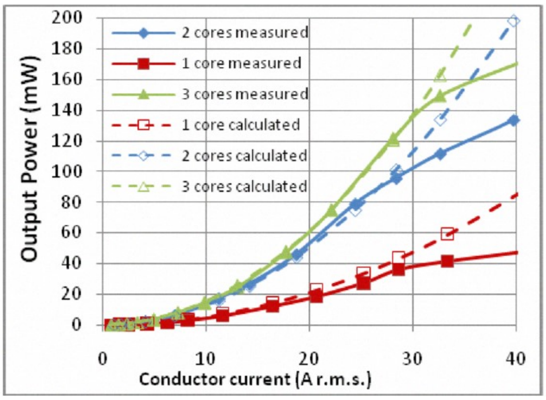

Fig. 5-6. The output power as a function of the conductor current [14].

In [19], a cylindrical core (*OD* = 16.3 mm, *ID* = 14.4 mm, *H* = 50 mm) with an air gap is designed to clamp on a current conductor. To prevent the core from being saturation, an air gap was introduced to the toroid core as shown in Fig. 5-7. The magnetic flux travels through two different mediums. As a result, the flux density in the core may be dramatically reduced compared to an unbroken toroid core, which prevents the core from the saturation.

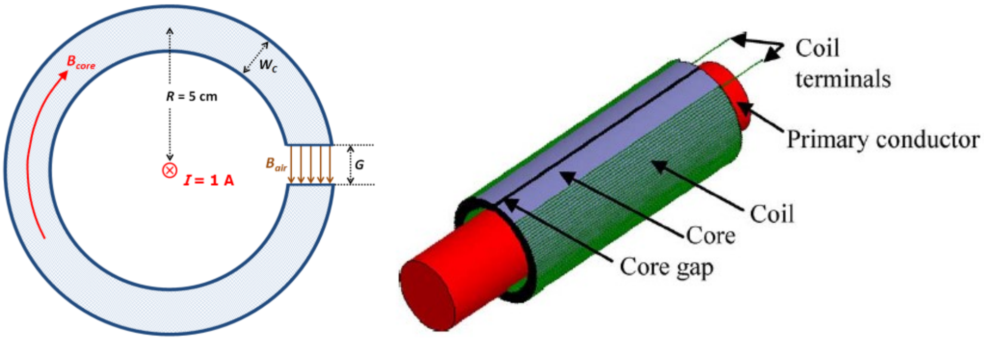

Fig. 5-7. Core with air gap [19].

Mu-metal is selected as the core material due to its high permeability. The air gap prevented the ferromagnetic core from the saturation so that the magnetic flux density in the core is linearly proportional to the current in the conductor. The experimental results show a power of 14.36 mW was collected with a power line current of 13.5 A. Although using the low permeability core or air-gap core can prevent the magnetic saturation successfully, the harvested power is not improved significantly.

On the other hand, some works aim to improve the harvesting efficiency with the magnetic saturation. Jinyeong Moon *et al* proposed a method based on the transfer window alignment (TWA), flux-shaping capacitor and active rectifier in [16]- [18]. The flux-shaping capacitor is connected in series with the core before the rectifying unit. The added capacitor will reform the flux developed across the core and lengthen the transfer window. The circuit model and simulated waveform of the flux-shaping method are shown in Fig. 5-8:

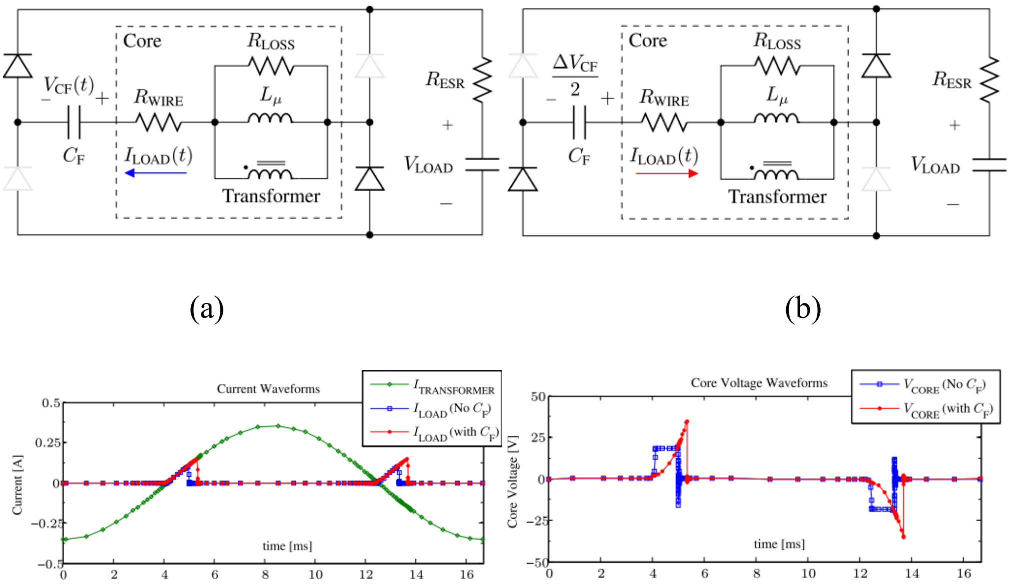

(a) (b)

(c) (d)

Fig. 5-8. Circuit model with a flux-shaping capacitor and simulated waveforms (a) before the current path reversal, (b) right after the current path reversal, (c) current waveforms, (d) core voltage waveforms [17].

The TWA method is to connect a purely resistive load to the magnetic core, then the middle of the transfer window is aligned with the peak of the power line current, enhancing the harvested power level. At the other time of the period, the load is disconnected from the core. The core is externally shorted to prevent itself from accumulating magnetic flux. The circuit model of TWA method and the simulated waveforms are shown in Fig. 5-9 and Fig. 5-10:

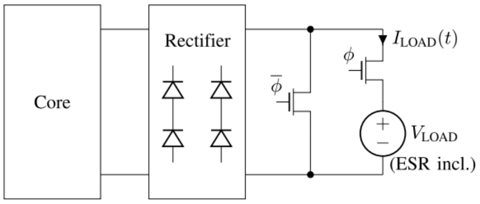

Fig. 5-9. TWA circuit model [17].

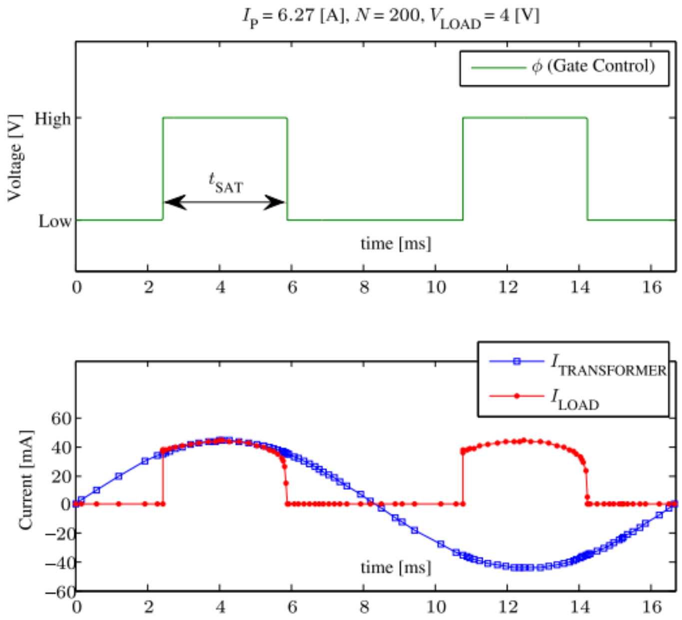

Fig. 5-10. Waveforms of the TWA circuit [17].

The actively controlled rectifier controls the current flowing directions. The switching devices used in rectification unit must be operated in accordance with the polarity of the power line current to ensure the current only flows into the load, which will enhance the harvesting efficiency. The active control circuit schematic is shown in Fig. 5-11 and Fig. 5-12:

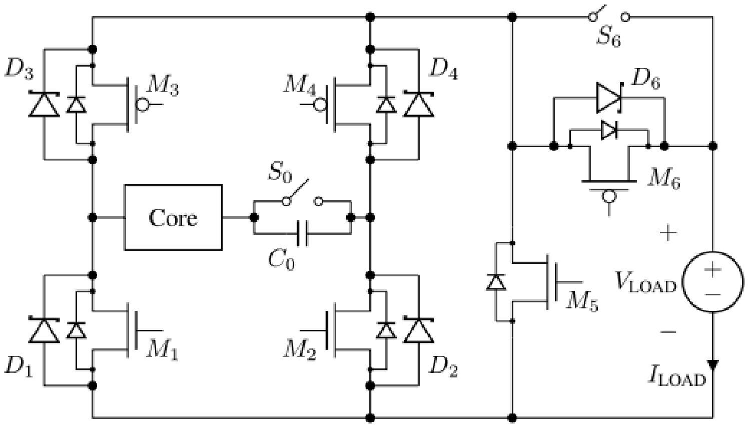

Fig. 5-11. Active rectifier circuit model [18].

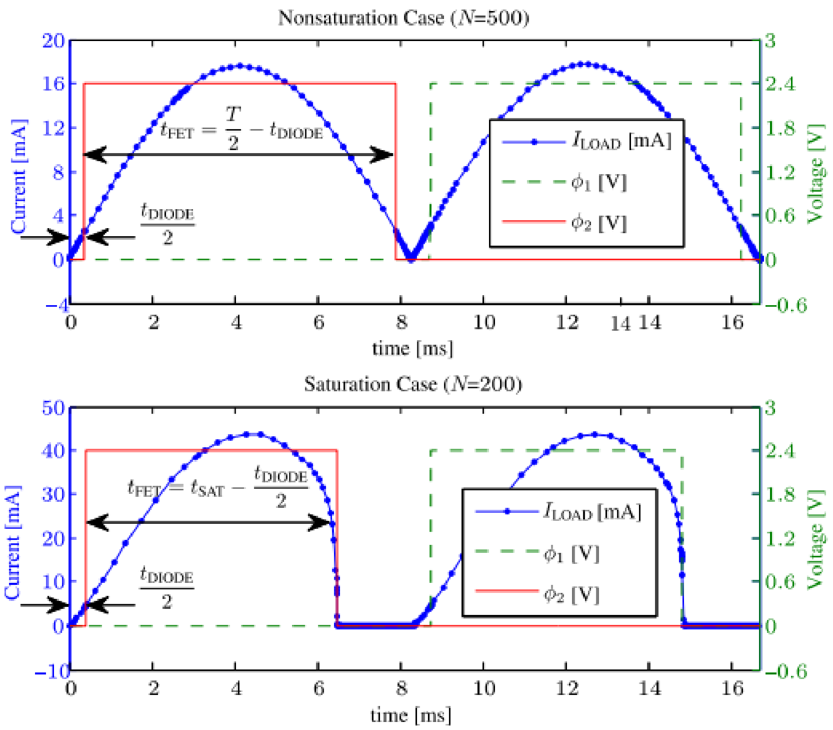

Fig. 5-12. The waveform of the active rectifier circuit [18].

In conclusion, the main methods of matching the impedance for maximum harvested power is to either prevent the magnetic flux saturation by introducing air gaps or reduce the core permeability or improve the harvesting efficiency when the core is saturated by applying flux-shaping capacitors, TWA method. Impedance matching problem in the circuits without the core saturation will be relatively easy as the non-linear behaviour of the core is mitigated, and the required impedance will be fixed. However, this will significantly limit the power harvested by the system as a higher permeability will lead to a high-power level. On the other hand, the methods of improving harvesting efficiency with saturation show a relatively high harvested power. Otherwise, active control schemes should be applied, leading to a complex circuity. Moreover, the control unit will also be power consuming which means extra power supplies are required, losing the meaning of self-sustainable sensor driving.

5.2 EH System Design Introduction

For smart grid applications, the real-time monitoring of device features and environmental parameters such as current, voltage, moisture and temperature of power infrastructures is very important. Wireless sensors can be used to monitor and report the status of power lines. They are affordable and require very low power. Energy harvesting (EH) technique is one of the most promising solutions for powering self-sustainable wireless sensing devices that have been widely demanded by the industry [21] – [31]. EH devices have been extensively researched for many different sources in the ambient environment such as solar [32], [33] wind [34], vibration [35] and kinetic [36]. However, solar and wind energy harvesters usually rely on the weather condition and require expensive energy storage devices for night or low wind operations [37], [38]. Based on the UK National Grid data, a typical substation has an average electric field strength of 10 kV/m and a magnetic field of 32 A/m, which can be a consistent and reliable energy source to drive sensors [39].

Electromagnetic EH techniques and topologies have been widely studied to harvest environmental energy. [40] – [42] reported electrical field energy harvesters which are in full enclosure on a conductor with a high voltage up to 100 kV. More than 200 mW can be extracted. The collected power will drop significantly when the conductor is in the power distribution mode where the voltage will be lower than 33 kV as the harvested power is proportional to the voltage squared [37]. Moreover, electric field harvesters are limited by the reactance of the coupling capacitor which only has a capacitance up to tens of pF typically, and a relatively large size (30cm width 55cm length in [37]). Thus, inductors with MH (Mega Hennery) inductance level are required to resonate at the power line frequency of 50/60 Hz. Such inductors are not commercially available. Compare to electrical field energy harvesters, magnetic field harvesters have several advantages. Firstly, a relatively smaller toroid core can be used to reduce the circuit size. Also, the inductance of a toroid coil is around mH to H, which will only need an nF to mF capacitor to resonate at 50/60 Hz. Such capacitors are commercially widely available. More importantly, by using a high permeability core, the magnetic flux passing through the coil will be improved. A magnetic field harvester can collect a large amount of energy even with a low primary side current [43], [44]. However, the saturation behaviour of magnetic cores is the main challenge in designing a magnetic field harvester on a high current power line. Many works have been reported to improve the efficiency of magnetic field harvesters [45] – [49] with the existence of magnetic flux density saturation. To the authors' best knowledge, there is still no suitable solution to harvest energy under the magnetic saturation condition.

This chapter presents a novel method for an electromagnetic EH that maximize the energy extraction from AC power lines, especially for magnetic saturation conditions. The proposed method employs a core that is clamped on the power line. The core usually has a high permeability so that it can harvest sufficient power even when the current on the power line is low. Owing to the high magnitude of the current flow of the power line, this core can be easily driven to its magnetically saturated region. An artificial magnetic field is introduced to the circuit which will manipulate the magnetic field induced by the power line so that the core is mainly working in the unsaturated region. With the aid of the presented novel method, the harvested power is significantly enhanced that would be large enough for many practical applications such as weather stations and data loggers etc. The chapter is organized as follow: Section 5.3 will discuss CT based EH devices and build the circuit model to analyze challenges of harvesting under the magnetic saturation condition. Section 5.4 will give details of the proposed method structure and numerical simulation results of the proposed prototype. Then the measured results and experimental validation will be shown in Section 5.5. Section 5.6 will conclude the chapter.

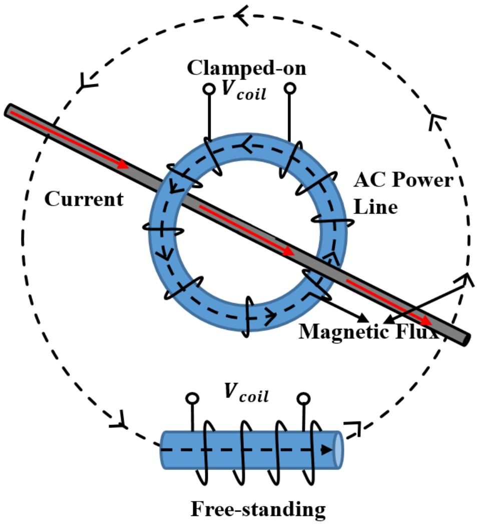

Fig. 5-13. Clamped-on and free-standing energy harvesters for AC power lines (physical sizes are not scaled, normally a clamped-on device is much smaller than a free-standing one).

5.3 Energy Extraction from AC Power Lines

5.3.1 Current Transformer-Based Energy Harvesters

Since the current on a power line is alternating, there exists a time-varying magnetic field whose magnitude is proportional to the magnitude of the current on the power line. Therefore, a current transformer (CT) consisting of a multi-turn coil wound on a magnetic core can be used to harvest energy by means of coupling the magnetic field around the power line.

Conventionally, there are two types of structures for such CT-based energy harvesters, namely, the clamped-on and the free-standing magnetic field energy harvesters which are depicted in Fig. 5-13. The free-standing harvester has advantages and conveniences in terms of installation and maintenance. But the harvested power level from them is relatively low. The magnetic flux will travel through the air into the core material by a distance. Therefore, the magnetic flux density in the core is relatively low which would limit the harvested power. Tahoura *et al.* reported an energy harvester with an average power of 160 μW at 50 A with a distance of 1.5 cm [24]. Yuan *et al.* achieved 360 μW at 500 A with a distance of 2 m [25]. These powers still cannot drive many high-power devices such as weather stations (e.g., input power > 1 W).

For a clamped-on harvester, the current conductor is fully enclosed by the harvesting coil. The dominant magnetic flux will travel within the same material. The magnetic flux density in the core can be significantly increased by using a high permeability material. Therefore, a relatively high power can be extracted from the power line. It has been reported in the literature that the clamped-on harvesters can provide an average output power up to 467 mW from a current of 50 A [49], which would be sufficient for many smart-grid sensing and monitoring applications. However, the power level of a clamped-on harvester usually suffers from magnetic saturation phenomenon of the core. Since the current amplitude in the power line is very high, the core could be driven into its saturation region which will significantly limit the extracted power. This chapter will focus on the method of improving the extracted power of the clamped-on energy harvester by using an artificial magnetic field to desaturate the magnetic core.

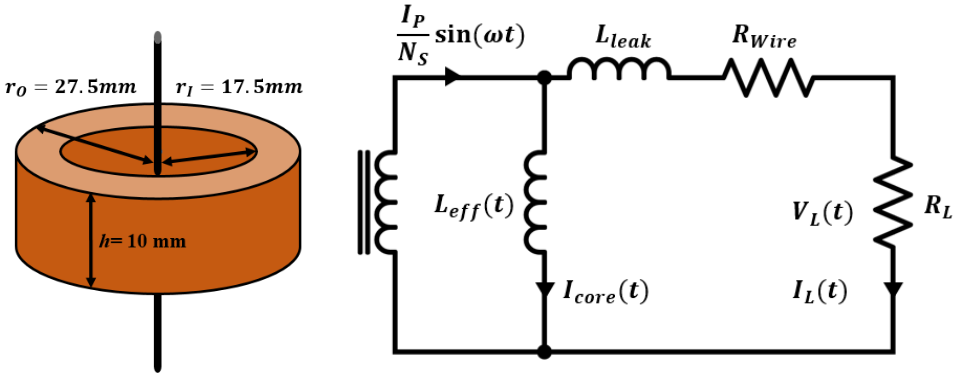

(a) **(b)**

Fig. 5-14. Circuit model (a) the magnetic core structure and dimensions used in the work, (b) secondary circuit model.

5.3.2 Circuit Modelling and Analysis

Fig. 5-14. (a) shows a magnetic core model as well as the dimensions of the core used in this work, where r_I, r_O and h are the inner, outer radius and the height of the core respectively. The magnetic flux path length of the core and the cross-section area of the core are denoted by l_{eff} and A_{core}. Due to that, the magnetic flux in the core will concentrate more where the path length is shorter, the effective length of the core should be modified from the average of the inner and the outer circumference of the core to:

$$l_{eff} = \frac{2\pi(r_0 - r_I)}{r_0 / r_I} \tag{5.4}$$

Fig. 5-14 (b) shows a circuit model of the secondary part of the magnetic core. The number of the secondary winding, primary side sinusoidal current, magnetizing inductance, magnetizing current, leakage inductance, load current, wire resistance are denoted by N_S, $I_P sin(\omega t)$, L_{eff}, $I_{CORE}(t)$, L_{Leak}, R_{Wire} $I_L(t)$ and R_L respectively. Since the core used in this work has very high permeability, the leakage inductance is negligible compared with the magnetizing inductance. In this work, we assume that the wire used in the analysis is lossless, hence $R_{Wire} = 0$.

When a primary current is applied, the equivalent circuit of the secondary side of the CT will have two branches of current. One branch flows into the load and the other one into the magnetizing inductor. The relationship between the primary side current, the load current and the magnetizing current can be described by Kirchhoff's Current Law as:

$$I_{core}(t) = I_P \sin(\omega t) / N_s - I_L(t) \tag{5.5}$$

The magnetic field *H(t)* can be expressed as:

$$H(t) = \frac{I_{\text{core}}(\omega t)}{l_{eff}} \tag{5.6}$$

The magnetic flux density *B(t)* is determined by the B-H curve of the core. A typical B-H curve of a magnetic core with saturation behaviour is shown in Fig. 5-15 (a). It can be observed that there are two boundaries which limit the maximum positive and negative magnetic flux density in the core regardless of the magnetic field strength. The boundary of the magnetic flux density B_{sat} is determined by the properties of the material [50].

For a core clamped on a power line, when the conducting current is zero, each crystal in the core has a magnetic domain randomly oriented initially. When the current in the power line increases, a magnetic field is applied to the material which will re-orient some of the magnetic domains in the direction of the external field. A higher H will align more domains. The core now is in the non-saturation region, and the magnetic flux density is proportional to the power line current. A large amount of energy can be extracted from this region. When the current in the power line keeps increasing, almost all domains will be aligned with the external H. The magnetic flux density will almost keep constant at B_{sat}. The ferromagnetic material is said to be saturated when the magnetic flux density reaches B_{sat}. In the saturation region, there is no more flux change in the core regardless of the magnitude of the current.

In this work, the target output power is about hundreds mW level, hence the hysteresis loss for the core is negligible. The nonlinear B-H behaviour can be idealized using the arctangent function as described in [45] as:

$$B(t) = B_{\text{sat}} \frac{2}{\pi} \arctan\left(\beta H(t)\right) \tag{5.7}$$

The constant β represents the sensitivity of the core in the non-saturation region as the permeability in traditional method [45]. The $B_{sat}*2/\pi$ is used to normalize the function to the maximum flux density B_{sat} when the core is saturated. The B-H curve is idealized into a saturation region and non-saturation as shown in Fig. 5-15. (b). Theoretically, the flux density will keep increasing even B_{sat} is achieved in the core due to that the vacuum permeability will still introduce a very small flux change. However, the vacuum flux variation is very small and can be ignored in the analysis. The core is considered saturated once the core magnetic flux density reaches B_{sat}.

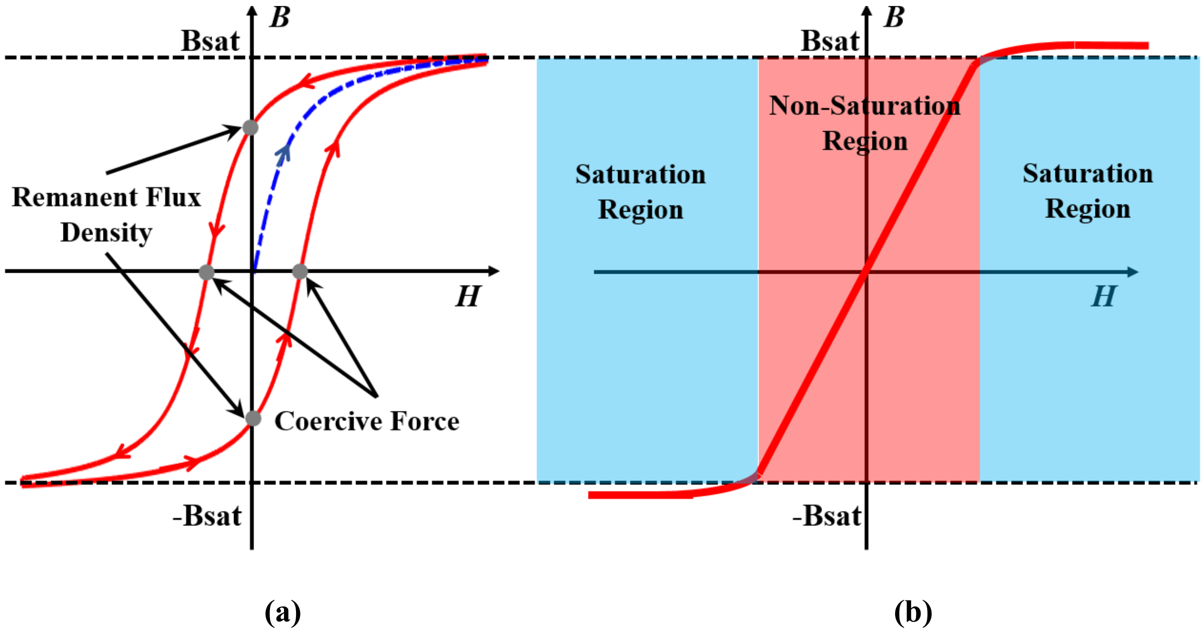

Fig. 5-15. B-H curves of the core with the saturation behaviour. (a) typical B-H curve, (b) idealized B-H curve.

5.3.3 Power Analysis

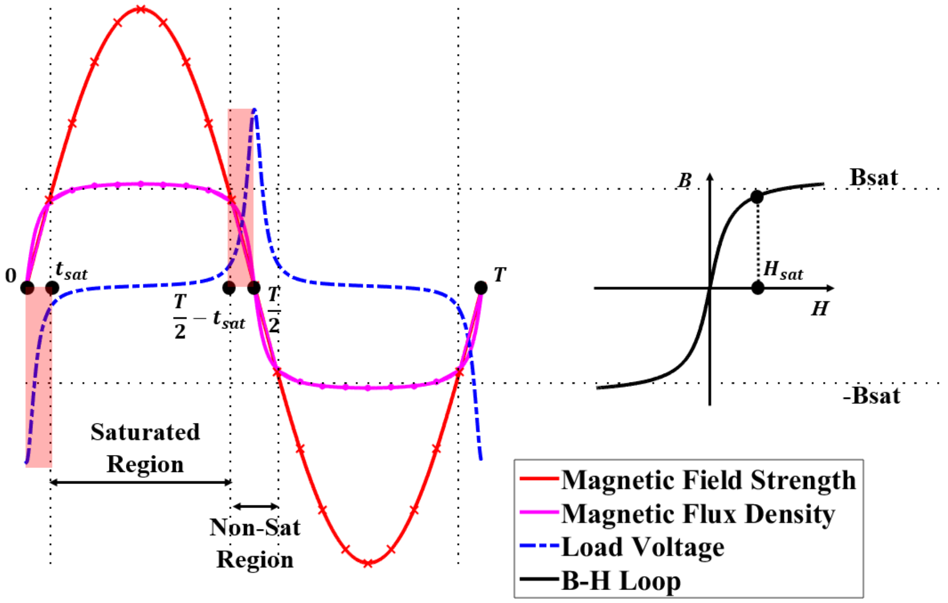

Fig. 5-16. Simulated core waveforms in the harvester and their relationship with the B-H curve.

If a current is applied to the primary side of the circuit, the voltage across R_L can be calculated by the derivative of the core magnetic flux:

$$V_L(t) = N_S \frac{d\Phi(t)}{dt} = A_{\text{core}} N_S \frac{dB(t)}{dt} \tag{5.8}$$

The relationship among the load voltage, magnetic field strength and magnetic flux density in the core is shown in Fig. 5-16. The voltage across the load is high for a small period when the core is in the non-saturation region. The magnetizing inductance can be treated as a parallel inductor of an ideal current. When the core is not saturated, the source impedance is very high and the current $I_{CORE}(t)$ flow into it will be near-zero. All current is consumed by the load. When the core is saturated, the magnetic flux density cannot increase anymore with the increase of the magnetic strength. The source impedance will perform like a short circuit to let the $I_{CORE}(t)$ flow through it to set up the magnetic flux [45]. Hence, only very little energy can be harvested when the core is saturated. The time that the core starts getting saturated is denoted by t_{sat}. The power harvested on the load for a half cycle $T/2$ of the primary side current is:

$$P_{\text{nonsat}} = 2 \times \frac{2}{T} \times \int_0^{t_{sat}} V_L^2(t) / R_L dt \tag{5.9}$$

The first coefficient "2" means that there are two non-saturation regions in half a cycle as illustrated by the shaded areas in Fig. 5-16. Before the core is saturated, all current from the ideal current source flows into the load. The time to drive the core into the saturation region t_{sat} can be calculated by taking the integral of (5.8):

$$\begin{aligned} A_{core} N_S B(t_{sat}) &= \int_0^{t_{sat}} V_L(t)\, dt \\ &= \int_0^{t_{sat}} R_L \frac{I_P}{N_S} \sin(\omega t)\, dt = \frac{I_P R_L}{N_S \omega}\left(1 - \cos(\omega t_{sat})\right) \end{aligned} \tag{5.10}$$

$$t_{sat} = \frac{1}{\omega} ar\cos\left(1 - \frac{\omega B_{sat} A_{\text{core}} N_S^2}{R_L I_P}\right) \tag{5.11}$$

By substituting (5.11) into (5.96), the power harvested at the non-saturation region can be represented as a function of R_L. The relationship between P_{nonsat} and R_L with different I_P can be plotted as shown in Fig. 5-17.

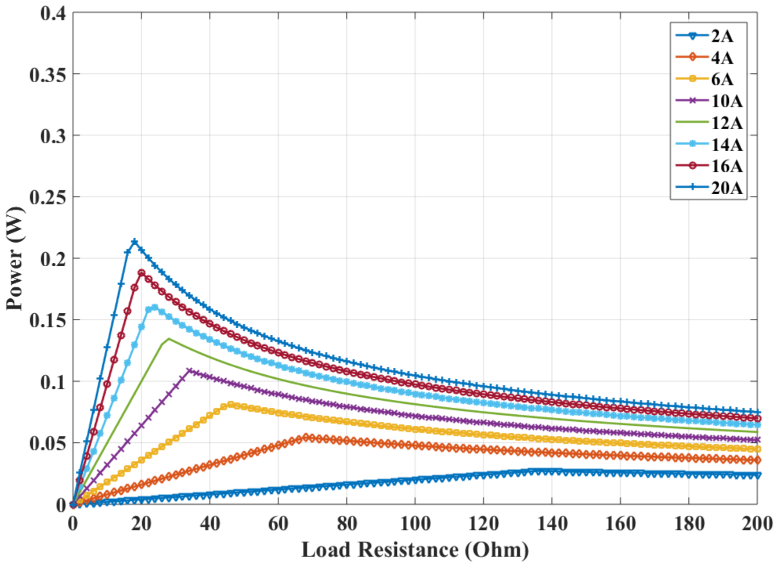

Fig. 5-17. Simulated harvested power versus load resistance under different primary currents.

5.4 Proposed Energy Harvesting Method

5.4.1 Proposed Desaturation Method

As discussed in section 5.3, the core of a magnetic field energy harvester can be easily saturated by a strong current in the power line. It is desired to maintain the core working in the non-saturation region for the whole period of the power line current. This can be achieved by applying a current in a direction opposite to that of the primary side. A controlled magnetic field H_C can be applied to the core artificially to manipulate the resultant magnetomotive force in order to prevent the core from being saturated.

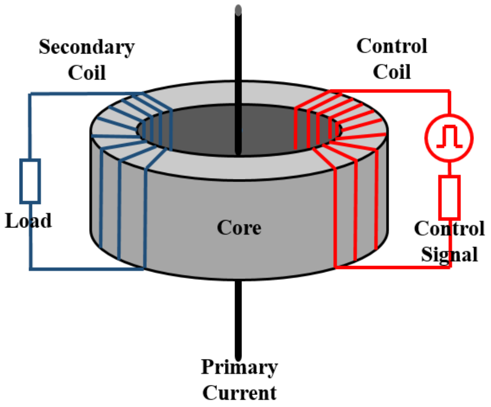

Fig. 5-18. The proposed EH structure by adding a control coil to apply the control current.

To introduce the controllable magnetic field to the core, a third winding is needed as aforementioned. The proposed energy harvester structure is illustrated in Fig. 5-18. The third coil (control coil) has a winding number of N_C, which can provide a current with a magnitude of I_C of the opposite direction of the power line current. The current will only be applied when the core is nearly saturated. In this case, based on the vector superposition, the equivalent magnetizing field strength in the core can be expressed as:

$$H_{eff}(t) = \frac{I_P \sin(\omega t) - I_C}{l_{eff}} \quad \textbf{(5.12)}$$

In order to ensure that the core will not be saturated during the whole period of the primary current, the magnitude of the control current should be high enough. On the other hand, applying the control current will consume energy. Hence to harvest energy efficiently, the control current should be as small as possible. Therefore, we should use a control current that will just pull I_P back to $I_P sin(\omega t_{sat})$ as:

$$I_C = I_P - I_P \sin\left(\omega t_{sat}\right) = I_P\left(1 - \sqrt{1 - \left(1 - \frac{\omega B_{sat} A_{eff} N_S^2}{R_L I_P}\right)^2}\right) \quad \textbf{(5.13)}$$

The control current should be only applied when the core is working in the saturation region. Therefore, the duration of I_P should be equal to the saturation time of each half cycle as:

$$t_C = \frac{T}{2} - 2t_{sat} = \frac{T}{2} - \frac{2}{\omega} ar\cos\left(1 - \frac{\omega B_{sat} A_{\mathrm{core}} N_S^2}{R_L I_P}\right) \quad \textbf{(5.14)}$$

Combining (5.12) – (5.14), the resultant magnetizing field that can prevent the core from being saturated can be calculated. The comparison of the primary side current, magnetic flux density, load voltage and added current waveforms on the circuit with and without the added current is illustrated in Fig. 5-19. With the added current, the magnetic flux density will not reach B_{sat}. There will be flux density change in the core most of the time in a period. Therefore, the amount of harvested energy can be significantly increased.

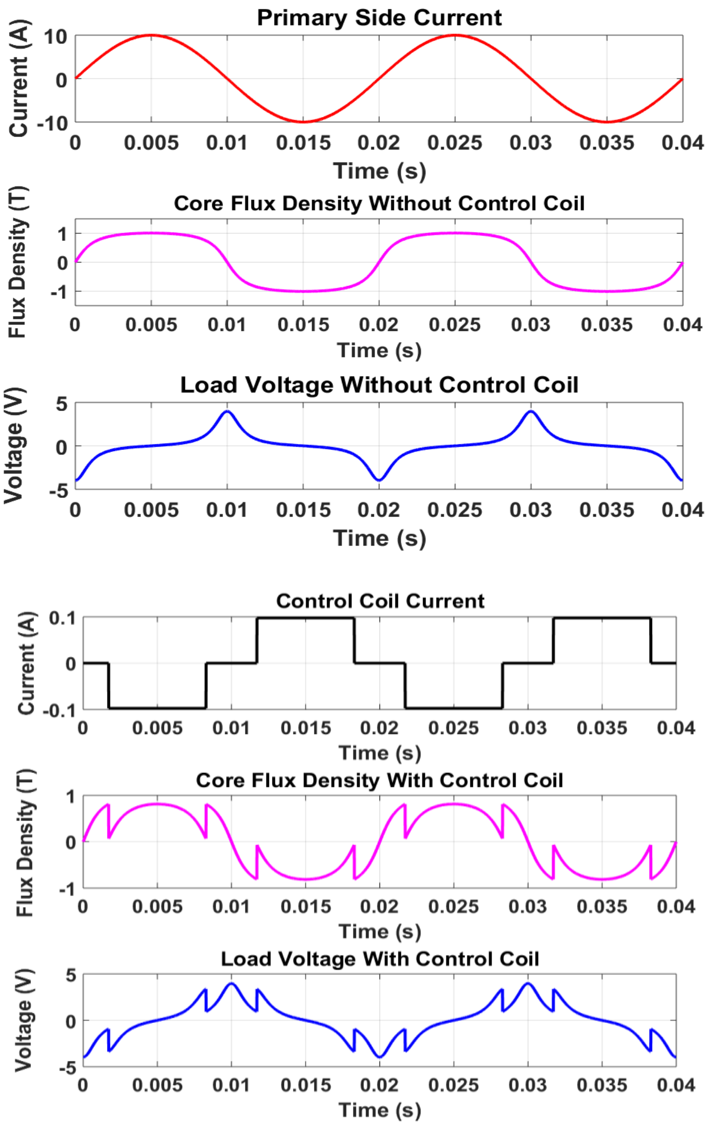

Fig. 5-19. Waveforms comparison with and without the proposed method.

5.4.2 Power Analysis and Numerical Simulation

Compared with the core waveforms shown in Fig. 5-16, the EH circuit with the proposed method will not only harvest energy during the non-saturation region but also in the saturation region as shown in Fig. 5-20. However the control coil does consume energy.

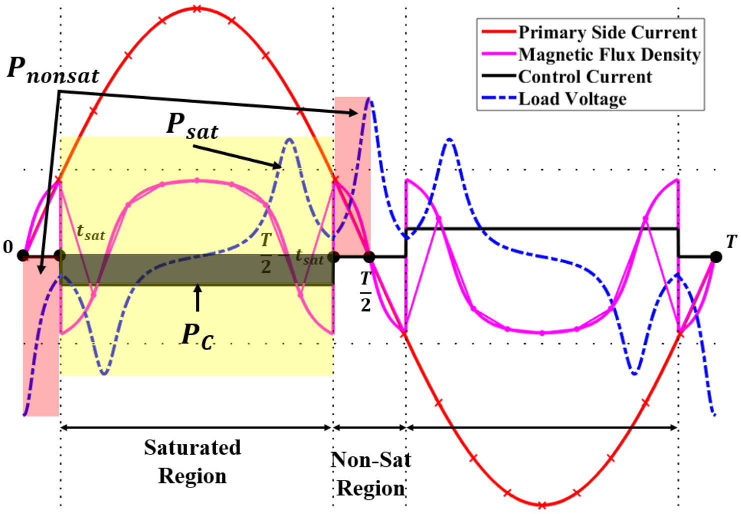

Fig. 5-20. Core waveforms simulation with the proposed method.

The power harvested during the non-saturation, saturation region and power consumed by the control coil are denoted by P_{nonsat}, P_{sat} and P_C respectively. The power harvested in the non-saturation region will not be affected by the control coil, hence it still can be calculated by (5.12). When the core is about to be driven into the saturation region, the control coil starts to feed current to manipulate the magnetic field. The source impedance in parallel will still be very high and $I_{core}(t)$ can be considered as zero. In this case, the current flowing into the load can be calculated by:

$$I_L(\mathrm{t}) = \left(I_P \sin(\omega t) - I_C\right) / N_S \tag{5.15}$$

The power harvested in the saturation region P_{sat} for a half cycle with the existence of the control current can be calculated by:

$$\begin{aligned}
P_{sat} &= \frac{2}{T}\int_{t_{sat}}^{(\frac{T}{2}-t_{sat})} I_L^{\,2}(t) R_L dt \\
&= \frac{2}{T}\int_{t_{sat}}^{(\frac{T}{2}-t_{sat})} \left((I_P \sin(\omega t) - I_C)/N_s\right)^2 R_L dt \\
&= \frac{2}{T}\Big(\frac{R_L}{4\omega N_S^{\,2}}(2\omega T I_C^2 - 8\omega I_C^2 t_{sat} + I_P^2 \sin(2\omega t_{sat}) \\
&\quad - I_P^2 \sin(\omega(T-2t_{sat})) + \omega T I_P^2 - 4\omega I_P^2 t_{sat} \\
&\quad - 8 I_c I_P \cos(\omega t_{sat}) + 8 I_C I_P \cos(\tfrac{1}{2}\omega(T-2t_{sat})))\Big)
\end{aligned} \tag{5.16}$$

The control current I_C is provided by a constant voltage source V_C and N_C number of windings on the core. The power dissipated by the control current for each half cycle can be calculated by:

$$P_C = \frac{2}{T}\frac{I_C}{N_C}V_C\left(\frac{T}{2}-2t_{sat}\right) = \frac{I_C V_C}{N_C}\left(1-\frac{ar\cos\left(1-\frac{\omega B_{sat}A_{eff}N_S^2}{R_L I_P}\right)}{\pi}\right) \tag{5.17}$$

Hence, the effective power P_{eff} harvested on the load for half a period of the primary current can be obtained by:

$$P_{eff} = P_{nonsat} + P_{sat} - P_C \tag{5.18}$$

It can be seen from (5.9) and (5.13) - (5.17) that for a given primary current, P_{nonsat}, P_{sat} and P_C are all dependent on the value of t_{sat}. From (5.11), t_{sat} is a function of load resistance R_L. Parametric simulation results of P_{nonsat}, P_{sat} and P_C against R_L with $I_P = 10$ A and $N_S = 100$ are shown in Fig. 5-21. P_{eff} is simulated against primary current as shown in Fig. 5-22.

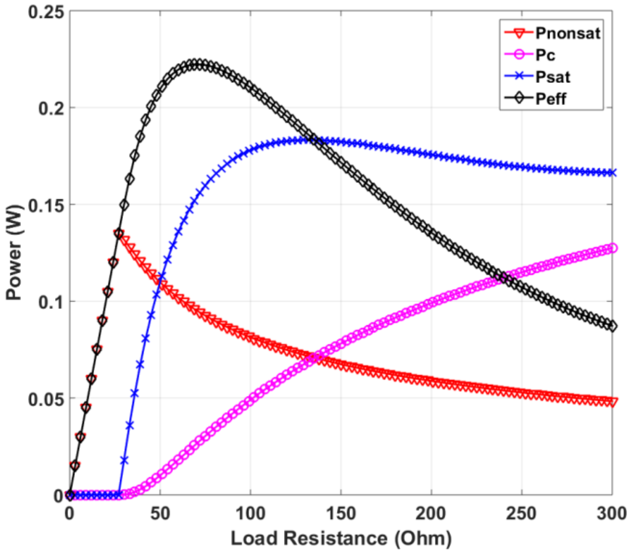

Fig. 5-21. Parametric simulation of P_{nonsat}, P_{sat}, P_C and P_{eff} against load resistance.

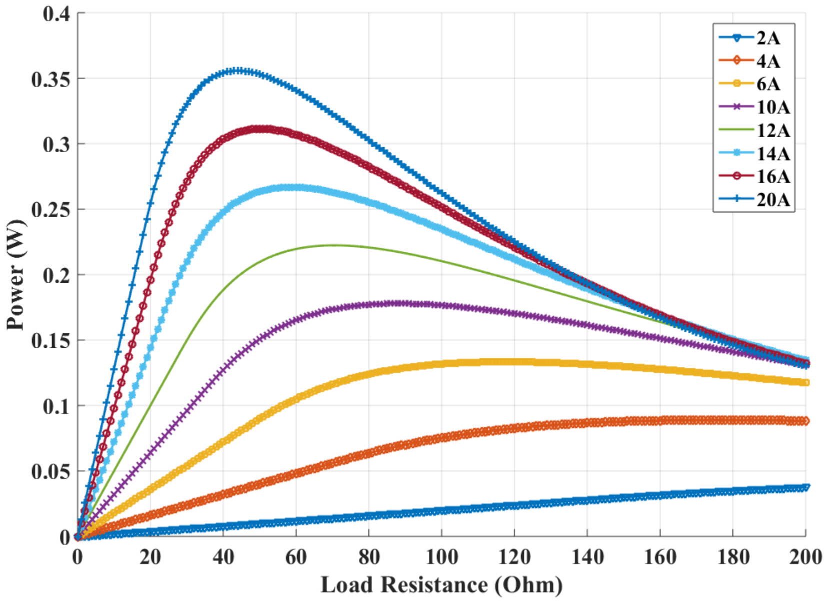

Fig. 5-22. Simulated harvested power versus load resistance with the proposed method under different primary side currents.

When the core is not saturated, the total harvested power with the proposed method is proportional to the load resistance. It equals to the power harvested in the non-saturation region as the control current is not applied. As the load resistance increases, the core starts to saturate. The power harvested will decrease. Then, a current will be applied to the control coil, to keep the core in the non-saturated region. According to (5.13) and (5.14), if the load resistance increases, the magnitude and duration of the control current will increase. Hence more power is needed for the control coil to manipulate the magnetic field. However, P_{sat} cannot increase forever with the increment of the load resistance. In this case, the power consumption of the control current will lower the effective harvested power once the R_L is greater than the optimal value. As aforementioned, the harvested power during the saturation period expressed in (5.16) is due to the introduction of the control current. Therefore, P_{sat} should be greater than P_C to ensure that the effective harvested power is increased by the proposed method. As shown in (5.9), (5.16) and (5.17), P_{nonsat}, P_{sat} and P_C are dependent on the value of load resistance R_L and the saturation time t_{sat}. Eq. (5.11) indicates that the saturation time is a function of R_L as well. The effective harvested power as expressed in (5.18) can be rewritten as a function of R_L. Then the value of R_L yielding the maximum effective harvested power can be calculated by solving the following equation:

$$\frac{dP_{eff}\left(R_L\right)}{dR_L}=0 \tag{5.19}$$

5.5 Measurement Results and Discussion

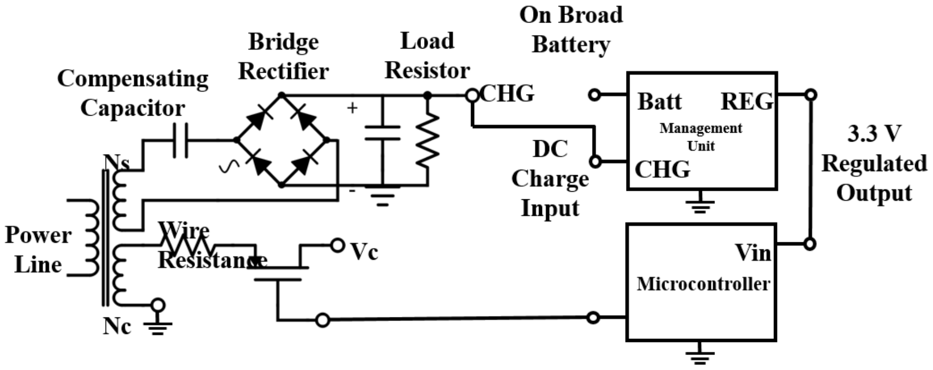

Fig. 5-23. A schematic circuit of the proposed energy harvester with a power management unit and a microcontroller.

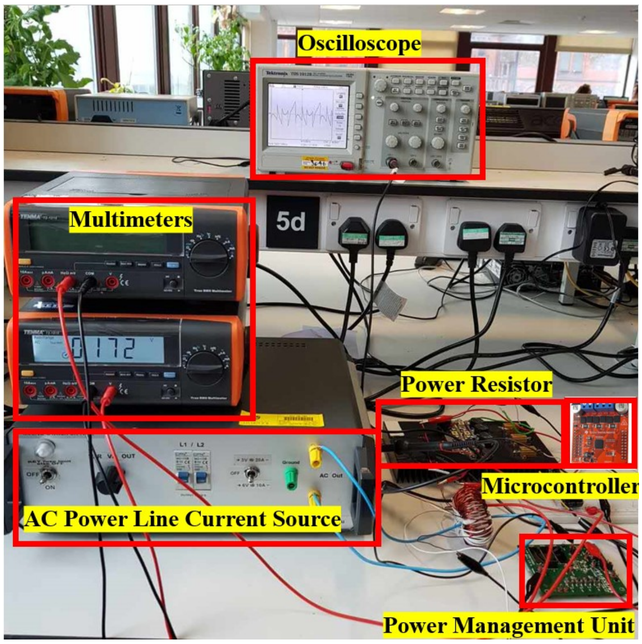

Fig. 5-24. A photo of the prototype and the measurement setup.

Measurement of the proposed energy harvester was carried out to validate the method. The schematic circuit of the proposed energy harvester and the measurement setup are shown in Fig. 5-23. and Fig. 5-24.

Table 5-I Core Parameters and Experimental Setup	
Core material:	Nano-crystalline
Number of secondary winding	$N_S = 100$
Number of the control winding	$N_C = 100$
Core height:	$H = 10$ mm

Outer radius:	$r_o = 27.5$ mm
Inner radius:	$r_i = 17.5$ mm
Effective length:	$l_{eff} = 27.2$ mm
Maximum flux density:	1.19 T
AC line current (rms):	10 A
Frequency:	50 Hz
Load resistor:	$R_L = 67\ \Omega$
Power management unit:	MAX17710
Micro-controller unit:	LAUNCHXL-F28377S BOOSTXL-DRV8305

The energy harvester prototype is constructed using a nano-crystalline magnetic core with the secondary winding of $N_S = 100$ and a control winding of $N_C = 100$. The core is clamped on a primary conductor. The conductor was a line connected to a current source to represent the AC power line. The secondary winding was connected to a series compensating capacitor for impedance matching purposes as shown in Fig. 5-23. Then a bridge rectifier was connected to convert the AC current into DC. A capacitor was placed after the rectifier in parallel with the load resistor to smooth the output voltage. The control winding was connected to a microcontroller which can switch on or off the control current to compensate the magnetic field as required. To make the system self-sustainable, a power management circuit MAX17710 from Maxim Integrated was applied to convert the energy harvested via the secondary winding and store it into an on-broad thin film rechargeable battery. The power management unit will also drive the microcontroller using a 3 V regulated output source. The core parameters and circuit components used in this system are listed in Table 5-I.

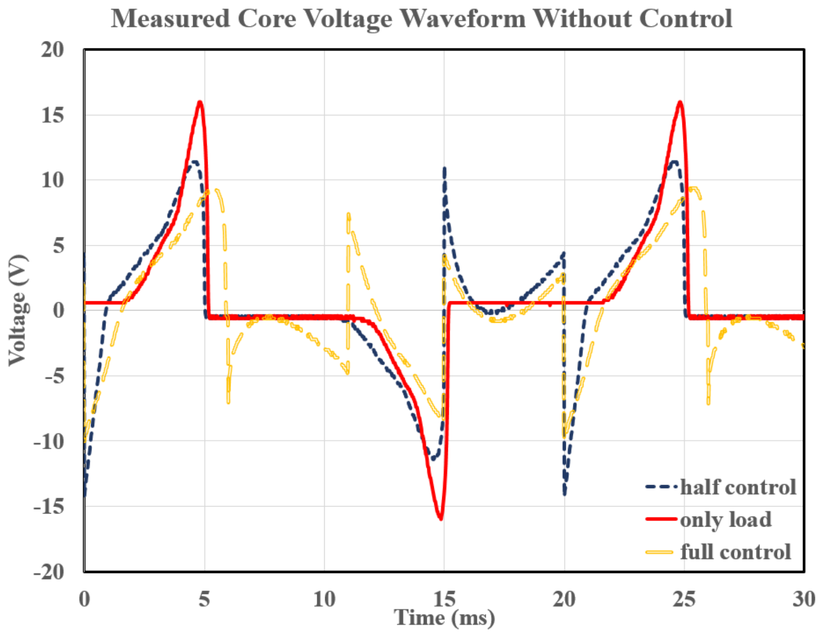

Fig. 5-25. Measured voltage waveforms with the proposed control coils (load only, half cycle control and full cycle control).

The waveforms on the energy harvester are measured by an oscilloscope. With a 10 A rms primary current, the results are shown in Fig. 5-25. When the current on the control winding is not activated, the core is working in the saturation region for the most duration of the primary current period, which limits the power harvested from the power line. Only 193 mW average power can be harvested without the proposed method. When the current on the proposed control winding is only activated in the negative half-cycle (the control current was applied only when the core would have been working in the saturation region), the average harvested power is increased to 230 mW. When the circuit with the control current is fully activated in both cycles, the average harvested power is increased to 283 mW, which is 45% higher compared to the circuit without the control winding.

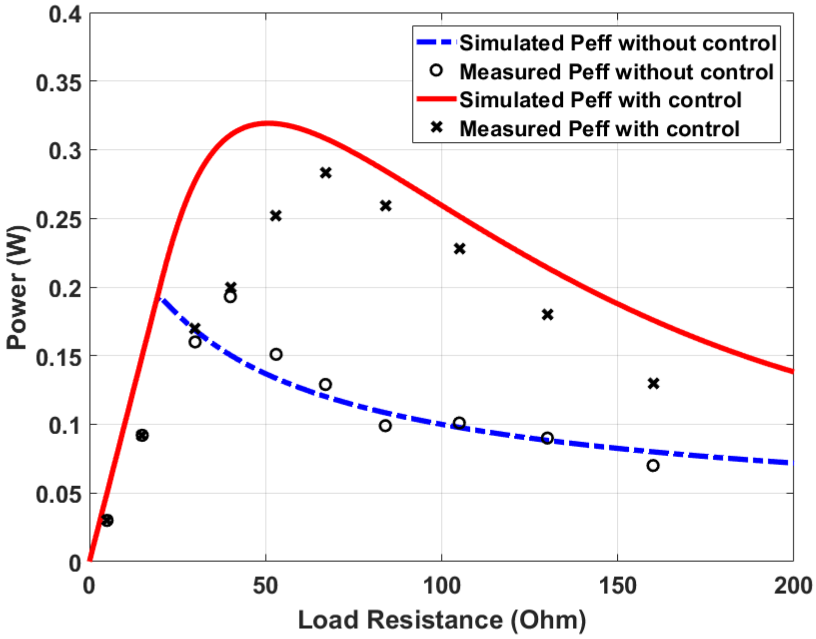

Fig. 5-26. Comparison of simulated and measured results of the circuit with and without the proposed method under a 10 A rms primary current.

As aforementioned, P_{eff} is dependent on the value of R_L. Power harvested by the energy harvester under a 10 A rms primary current was measured against the load resistance. Fig. 5-26. shows the comparison of the simulated and measured results of the energy harvesting system with and without the proposed method. The measured results of the circuit using the proposed method are very close to the simulation before the saturation occurs. The measured power is lower than the prediction in the saturation region. This is because the control coil has been activated and the microcontroller will consume several mW power. Both have not been considered in the simulation. The measured results have shown good agreement with the simulation which verifies the derived equations and the proposed method.

5.6 Summary

In this chapter, a novel method has been introduced to increase the level of power harvested from an AC power line. To capture the magnetic field energy around the power line, a nano-crystalline core with a high permeability has been used. Due to the high current in the power line, the core is easily driven into the saturated operation condition. Very little power can be harvested when the core is saturated. To keep the core in the non-saturation operation region, a control coil has been added to the harvester. The control coil can generate a magnetic field H_C to artificially mitigate the magnetic saturation of the core. Numerical simulation shows very good agreement with the measured results. The proposed energy harvester has achieved an average output power of 283 mW on a power line with a current of 10A rms, which indicates a 45% increase compared to a harvester without using the proposed method. The proposed harvesting method have shown excellent potential for smart-grid applications such as driving the power line monitoring sensors and weather stations.

5.7 References

[1] S. Ulukus, A. Yener, E. Erkip, O. Simeone, M. Zorzi, P. Grover and K. Huang, "Energy Harvesting Wireless Communications: A Review of Recent Advances", *IEEE Journal Selected Areas Communications*, vol. 33, no. 3, pp. 360-381, 2015.

[2] Z. Wan, Y. Tan and C. Yuen, "Review on energy harvesting and energy management for sustainable wireless sensor networks", *IEEE 13th International Conference on Communication Technology*, 2011

[3] S. Yuan, Y. Huang, J. Zhou, Q. Xu, C. Song and P. Thompson, "Magnetic Field Energy Harvesting Under Overhead Power Lines", *IEEE Transactions on Power Electronics*, vol. 30, no. 11, pp. 6191-6202, 2015.

[4] V. Raghunathan, A. Kansal, J. Hsu, J. Friedman, Mani Srivastava, “Design considerations for solar energy harvesting wireless embedded systems,” *Information Processing in Sensor Networks*, pp. 457-462, 2005.

[5] S. Bader, B. Oelmann, “Enabling Battery-Less Wireless Sensor Operation Using Solar Energy Harvesting at Locations with Limited Solar Radiation,” *4th Int. conf. on Sensor Technologies and Applications* (SENSORCOMM), pp. 602-608, 2010.

[6] F. Guo, H. Hayat and J. Wang, "Energy harvesting devices for high voltage transmission line monitoring", *IEEE Power and Energy Society General Meeting*, 2011.

[7] H. Zangl, T. Bretterklieber and G. Brasseur, "A Feasibility Study on Autonomous Online Condition Monitoring of High-Voltage Overhead Power Lines", *IEEE Trans. Instrum. Meas.*, vol. 58, no. 5, pp. 1789-1796, 2009.

[8] M. Moser, T. Bretterklieber, H. Zangl and G. Brasseur, "Strong and Weak Electric Field Interfering: Capacitive Icing Detection and Capacitive Energy Harvesting on a 220-kV High-Voltage Overhead Power Line", *IEEE Transaction on Industrial Electronics.*, vol. 58, no. 7, pp. 2597-2604, 2011.

[9] J. Zhang, P. Li, Y. Wen, F. Zhang and C. Yang, "A Management Circuit with Upconversion Oscillation Technology for Electric-Field Energy Harvesting", *IEEE Transactions on Power Electronics*, vol. 31, no. 8, pp. 5515-5523, 2016.

[10] R. Moghe, A. Iyer, F. Lambert and D. Divan, "A Low-Cost Electric Field Energy Harvester for an MV/HV Asset-Monitoring Smart Sensor", *IEEE Transactions on Industry Applications*, vol. 51, no. 2, pp. 1828-1836, 2015.

[11] M. Zhu, M. Judd and P. Moore, "Energy Harvesting in Substations for Powering Autonomous Sensors", *Third International Conference on Sensor Technologies and Applications*, 2009.

[12] J. Rodriguez, D. Holmes, B. McGrath and R. Wilkinson, "Maximum energy harvesting from medium voltage electric-field energy using power line insulators", *Australasian Universities Power Engineering Conference (AUPEC)*, 2014.

[13] M. Moser, T. Bretterklieber, H. Zangl and G. Brasseur, "Strong and Weak Electric Field Interfering: Capacitive Icing Detection and Capacitive Energy Harvesting on a 220-kV High-Voltage Overhead Power Line", *IEEE Transaction on Industrial Electronics*., vol. 58, no. 7, pp. 2597-2604, 2011.

[14] N. Roscoe, M. Judd and J. Fitch, "Development of magnetic Induction Energy Harvesting for Condition Monitoring", *44th International University Power Engineering Conference (UPEC)*, 2009.

[15] J. Moon and S. Leeb, "Analysis Model for Magnetic Energy Harvesters", *IEEE Transactions on Power Electronics*, vol. 30, no. 8, pp. 4302-4311, 2015.

[16] J. Moon, J. Donnal, J. Paris and S. Leeb, "VAMPIRE: A magnetically self-powered sensor node capable of wireless transmission", *Twenty-Eighth Annual IEEE Applied Power Electronics Conference and Exposition (APEC),* 2013.

[17] J. Moon and S. Leeb, "Power Electronic Circuits for Magnetic Energy Harvesters", *IEEE Transactions on Power Electronics*, vol. 31, no. 1, pp. 270-279, 2016.

[18] J. Moon and S. Leeb, "Power loss analysis with high primary current in magnetic energy harvesters", *IEEE 16th Workshop on Control and Modeling for Power Electronics (COMPEL)*, 2015.

[19] R. Bhuiyan, R. Dougal and M. Ali, "A Miniature Energy Harvesting Device for Wireless Sensors in Electric Power System", *IEEE Sensors Journal,* vol. 10, no. 7, pp. 1249-1258, 2010.

[20] Y. Zhuang, C. Xu, S. Yuan, C. He, J. Zhou, Y. Huang, A. Chen and W. W. Lee, “Design of an Energy Harvesting System on Power Transmission Lines,” *IEEE MTT-S Wireless Power Transfer Conference, Taipei*, Taiwan, May, 2017.

[21] S. Ulukus, A. Yener, E. Erkip, O. Simeone, M. Zorzi, P. Grover and K. Huang, “Energy harvesting wireless communications: a review of recent advances*”, IEEE Journal Selected Areas Communications,* vol. 33, no. 3, pp. 360-381, 2015.

[22] M. Magno, D. Boyle, D. Brunelli, B. O’Flynn, E. Popovici and L. Benini, “Extended Wireless monitoring through intelligent hybrid energy supply*”, IEEE Transactions on Industrial Electronics*, vol. 61, no. 4, pp. 1871-1881, 2013.

[23] P. Li, Y. Wen, Z. Zhang and S. Pan, “A high-efficiency management circuit using multi winding upconversion current transformer for power-line energy harvesting*”, IEEE Transactions on Industrial Electronics*, vol. 62, no. 10, pp. 6327-6335, 2015.

[24] T. Hosseinimehr and A. Tahesh, "Magnetic field energy harvesting from AC lines for power wireless sensor nodes in smart grids", *IEEE Transactions on Industrial Electronics*, vol. 63, no. 8, pp. 4947-4954, 2016.

[25] S, Yuan, Y. Huang, J. Zhou, Q. Xu, C. Song and P. Thompson, "Mangetic field energy harvesting under overhead power lines", *IEEE Transactions on Power Electronics*, vol. 30, no. 11, pp. 6169-6202, 2015.

[26] R. Bondade, Y. Zhang, B. Wei, T. Gu, H. Chen and D. B. Ma, "Integrated auto-reconfigurable power-supply network with multidirectional energy transfer for self-reliant energy-harvesting application", *IEEE Transactions on Industrial Electronics*, vol. 63, no. 5, pp. 2850-2861, 2016.

[27] N. Rezaei-Hosseinabadi, A. Tabesh, R. Dehghani and A. Aghili, "An efficient piezoelectric windmill topology for energy harvesting from low-speed air flows", *IEEE Transactions on Industrial Electronics*, vol. 62, no. 6, pp. 3576-3583, 2014.

[28] Smart Grid Infrastructure: Energy Harvesting – Block Diagram (SBD) | TI.com, 2016. Available: http://www.ti.com/solution/energy_harvesting. [Accessed: 03-Aug-2017]

[29] B. R. Flynn, and PE, "Key Smart Grid Applications", GE Energy, Available:http://www.gegridsolutions.com/multilin/journals/issues/spring09/smart_grid_applications.pdf. [Accessed: 03-Aug-2017]

[30] C. Li, G. Ma and B. Qi, "Condition monitoring and diagnosis of high-voltage equipment in China – recent progress", *IEEE Electrical Insulation Magazine,* vol. 29, no. 5, pp. 71-78, 2013.

[31] V. C. Gungor, B. Lu, G. P. Hancke, "Opportunities and challenges of wireless sensor network in smart grid", *IEEE Transaction on Industrial Electronics,* vol. 57, no. 10, pp. 3557-3564, 2010.

[32] V. Raghunathan, A. Kansal, J. Hsu, J. Friedman, and M. Srivastava, "Design considerations for solar energy harvesting wireless embedded system", *Information Processing in Sensor Network,* pp. 457-562, 2005.

[33] S. Bader, and B. Oelmann, "Enabling battery-less wireless sensor operation using solar energy harvesting at locations with limited solar radiation", *4th Int. conf. on Sensor Technologies and Applications (SENSORCOMM),* PP. 602-608, 2010.

[34] C. Tsai, C. Hsieh, and S. Huang, "Enhancement of damage-detection of wind turbine blades via CWT-based approaches", *IEEE Transactions on Energy Conversion,* vol. 21, no. 3, pp. 776-781, 2006.

[35] Y. Sang, X. Huang, H. Liu, and P. Jin, "A vibration-based hybrid energy harvester for wireless sensor systems," *IEEE Trans. Magn.*, vol. 48, no. 11, pp. 4495–4498, Nov. 2012.

[36] A. Khaligh, P. Zeng, and C. Zheng, "Kinetic energy harvesting using piezoelectric and electromagnetic technologies state of the art," *IEEE Trans. Ind. Electron.*, vol. 57, no. 3, pp. 850–860, Mar. 2010.

[37] H. Zangl, T. Bretterkileber and G. Brasseur, "A feasibility study on autonomous online condition monitoring of high-voltage overhead power lines," *IEEE Transactions on Instrumentation and Measurement*, vol. 50, no. 5, pp. 1789-1796, 2009.

[38] J. A. Paradiso and T. Starner, "Energy scavenging for mobile and wireless electronics", *IEEE Pervasive Computing*, vol. 4, pp. 18-27, 2005.

[39] "National Grid substations | EMFs.info", *EMFs.info*, 2013. [Online]. Available: http://www.emfs.info/sources/substations/substations-ng/. [Accessed: 05-10-2017].

[40] F. Guo, H. Hayat and J. Wang, "Energy harvesting devices for high voltage transmission line monitoring", *IEEE Power and Energy Society General Meeting*, 2011.

[41] J. Rodriguez, D. Holmes, B. McGrath and R. Wilkinson, "Maximum energy harvesting from medium voltage electric-field energy using power line insulators", Australasian Universities Power Engineering Conference, 2014.

[42] M. Moser, T. Bretterklieber, H. Zangl and G. Brasseur, "Strong and weak electric field interfering: Capacitive icing detection and capacitve energy harvesting on 220-kV high-voltage overhead power line", *IEEE Transactions on Industrial Electronics*, vol. 58, no. 7, pp. 2597-2604, 2011.

[43] R. Bhuiyan, R. Dougal and M. Ali, "A miniature energy harvesting device for wireless sensors in electric power system*", IEEE Sensor Journal*, vol. 10, no. 7, pp. 1249-1258, 2010.

[44] K. Tashiro, H. Wakiwaka, S. Inoue and Y. Uchiyama, "Harvesting energy of magnetic power-line noise*", IEEE Transactions on Magnetics*, vol. 47, no. 10, pp. 4441-4444, 2011.

[45] J. Moon and S. Leeb, "Analysis model for magnetic energy harvesters*", IEEE Transactions on Power Electronics*, vol. 30, no. 8, pp. 4302-4311, 2015.

[46] J. Moon and S. Leeb, "Power loss analysis with high primary current in magnetic field energy harvesters*", IEEE 16th Workshop on Control and Modelling for Power Electronics (COMPEL), 2015.*

[47] J. Moon and S. Leeb, "Power electronic circuits for magnetic energy harvesters*", IEEE Transactions on Power Electronics*, vol. 31, no. 1, pp. 270-279, 2016.

[48] N. Roscoe and M. Judd, "Harvesting energy from magnetic fields to power condition monitoring sensors*", IEEE Sensor Journal*, vol. 13, no. 6, pp. 2263-2270, 2013.

[49] N. Roscoe, M. Judd and J. Fitch, "Development of magnetic induction energy harvesting for condition monitoring*", 44th International University Power Engineering Conference (UPEC), 2009.*

[50] M. Santos, D, Vieira, Y. Rodriguez, C. Souza, T. Moraes and R. Freire, "Energy harvesting using magnetic induction considiering different core materials*", IEEE International Instrumentation and Measurement Technology Conference (12MTC) Proceedings, 2014.*

Chapter 6 **Range-Adaptive Wireless Power Transfer System Using Multi-Antiparallel Loops**

This chapter presents a range-adaptive wireless power transfer (WPT) system with high power transfer efficiency using a two-coil structure with multiple bidirectional loops. This work focusses on constraining the impedance variation caused by mutual inductance variation with respect to the changing of the transfer position. WPT systems using coupled magnetic resonances are susceptible to the transfer position. This is mainly due to that the coupling condition between the transmitting and receiving coils is highly position-dependent. Once the transfer position deviates from the optimum one, the coupling will be either excessive or weak which results in transfer efficiency degradation. Here we present a transmitter structure consisting of multiple sub-coils oriented in opposite directions to keep the coupling relatively constant over an extensive range of transfer positions. We were able to achieve a transmission coefficient of 70% - 88% with transfer distance varying from 0 mm to 70 mm and a coefficient of 60% - 85% with the misalignment changing from 0 mm – 80 mm at a 40 mm transfer distance. The diameters of the transmitter and receiver are 84.6 mm and 45.1 mm respectively. The measured transmission coefficient of the proposed design can be kept better than 70% with a transfer distance varying from 0 mm to 50 mm while the misalignment changing from 0 mm to 50 mm. The performance of the system much less sensitive to the transfer position shows that the design method has a great potential in wireless charging applications.

6.1 Range-Adaptive Wireless Power Transfer Review

Wireless power transfer (WPT) is the transmission of electrical energy without solid state media as a physical media between the source and receiver. In a typical WPT system, the transmitter (Tx) is usually driven by electric power source which generates a time-varying electromagnetic field. Then the receiver (Rx) captures the electromagnetic field propagating in the space and supplies the power to the load. WPT is a promising technique to power electrical devices where interconnecting wires are inconvenient, hazardous, or are not possible.

WPT based on the magnetic resonance was first reported by Tesla [1]. His main contributions in WPT research have been concluded in three aspects by an article in 1943 [2] as: i) the idea of inductive coupling between the driving and the working circuits; ii) the importance of tuning both circuits, that is, the idea of an 'oscillation transformer'; iii) the idea of a capacitance loaded open secondary circuit. It is no doubt that these aspects formed the operating principles for the WPT technologies. One of Tesla's WPT experimental diagrams is shown Fig. 6-1:

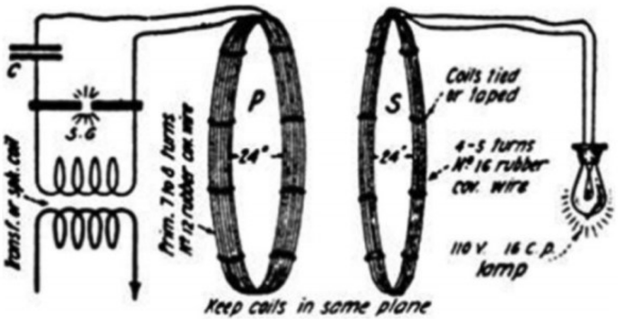

Fig. 6-1. A diagram of Tesla's WPT experiment [3].

Modern WPT techniques are mainly categorized into far-field or radiative and near-field or non-radiative. The most popular technologies in far-field WPT are microwave and lasers. The power can be radiated or emitted by an antenna and transmitted via air for a very long distance up to kilometres [4]. However, suffering from the unavoidable path, the power transfer efficiency (PTE) of far-field WPT is usually very low. On the other hand, the non-radiative near-field WPT such as magnetic coupling with inductive coils or electric coupling using capacitive conductors will provide a promising PTE [4].

WPT researches have been conducted in energy systems for medical implants since the 1960s [5] – [9] and induction heaters [10] since 1970s. For modern short-range applications, the inductive WPT (IPT) systems [11] – [15] for portable devices [16] – [18] have attracted much attention. WPT solutions for portable electronic devices have reached the commercialisation stage through the launch of the "Qi" Standard by the Wireless Power Consortium. It has been a common practice to adopt Tesla's principles of i) using near-field magnetic coupling; ii) resonance coupling between the Tx and Rx. The primary reason for using the near-field magnetic coupling and resonance techniques together is to compensate the inductance leakage in the power flow path for high PTE. For the IPT applications of several kilowatts such as charging an electric vehicle (EV), 90% efficiency is achievable. However, the PTE of WPT systems will depend on many parameters such as transfer distance, displacement and coil sizes.

Many applications demand a flexible transfer position. Once the transfer position of the device deviates from its optima, the impedance matching quality will be degraded. In this case, the PTE will be heavily reduced. Herein, designing a WPT system with high PTE that robust to the variation of transfer position becomes my research interest. The second part of the thesis will mainly focus on:

- To improve the PTE of MRC-WPT devices
- To extend the transfer position of WPT
- To propose a novel structure that can maintain high PTE and robust to the variation of transfer position for WPT devices.

6.1.1 Impedance Matching of WPT System

For a typical four-coil MRC-WPT system contains two magnetic coupling resonators as shown in Fig. 6-2 [19], [20]:

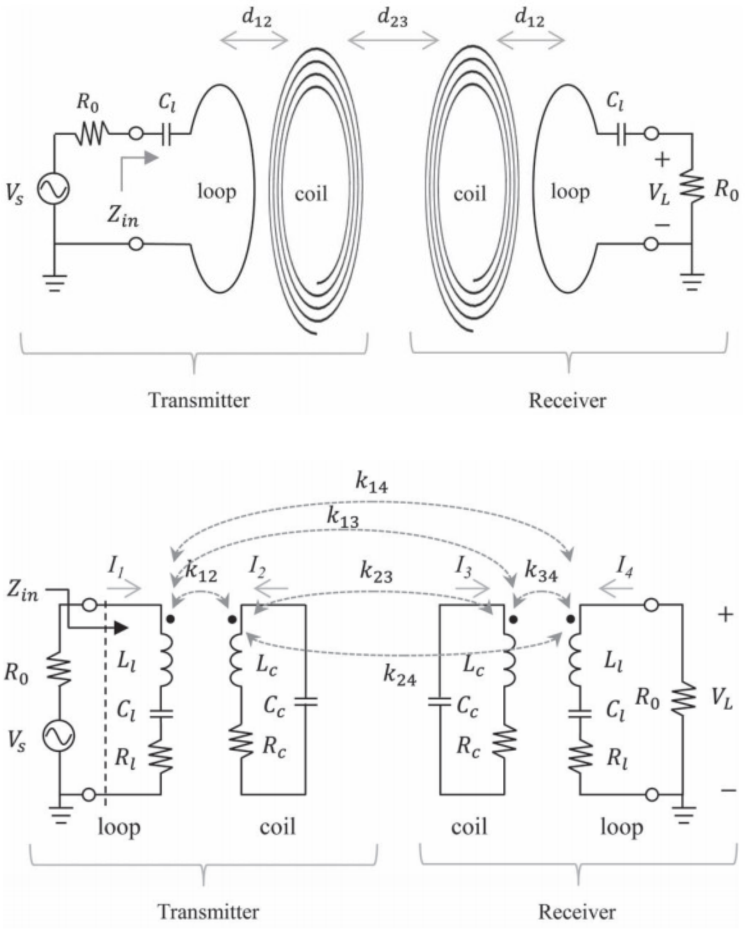

Fig. 6-2. Equivalent circuit model of a four-coil MRC-WPT system.

Following the analysis in [19], let denote the self-inductance, parasitic resistance and resonating capacitor by L_l, R_l and C_l in the feed/load loop respectively. Represent the self-inductance, parasitic resistance and resonating capacitor by L_C, R_C and C_C in the transmitting/receiving coil where the transmitter and receiver are set to be identical for simplicity. The coupling coefficients between coils and loops are represented by k_{ij}, where $k_{12} = k_{34}$ and $k_{13} = k_{24}$. The power source in Tx is represented by the voltage source V_s with internal resistance R_0. The load in Rx is represented by R_0. The node matrix of the system can be drawn at the resonant frequency ω_0:

$$\begin{bmatrix} R_0 & j\omega_0 M_{12} & j\omega_0 M_{13} & 0 \\ j\omega_0 M_{12} & R_C & j\omega_0 M_{23} & j\omega_0 M_{13} \\ j\omega_0 M_{13} & j\omega_0 M_{23} & R_C & j\omega_0 M_{12} \\ 0 & j\omega_0 M_{13} & j\omega_0 M_{12} & R_0 \end{bmatrix}^{-1} \begin{bmatrix} V_S \\ 0 \\ 0 \\ 0 \end{bmatrix} = \begin{bmatrix} I_1 \\ I_2 \\ I_3 \\ I_4 \end{bmatrix} \tag{6.1}$$

where M_{ij} is the mutual inductance. The PTE can be represented by the quality-factors of the coils and the coupling coefficients as [21]:

$$\eta = \frac{V_L^2 / R_0}{V_S^2 / 4R_0} = \frac{4Q_1^2 Q_2^2 \left(k_{12}^2 k_{23} Q_2 + 2jk_{12}k_{13} + k_{13}^2 k_{23} Q_2\right)^2}{\left(j\left(\left(1 + k_{12}^2 Q_1 Q_2\right)^2 + k_{23}^2 Q_2^2 + k_{13}^2 Q_1 Q_2 \left(k_{13}^2 Q_1 Q_2 - 2k_{12}^2 Q_1 Q_2 + 2\right)\right) + 4k_{12}k_{13}k_{23}Q_1 Q_2^2\right)^2} \tag{6.2}$$

It can be found from (6.2) that the PTE varies with k_{23}, [22], [23]. This can also be explained by that the input impedance of the WPT system depending on d_{23}. Therefore, the input impedance Z_{in} changes with k_{23} and it is matched to R_0 at only a single $k_{23,matched}$, for a fixed k_{12}. The $k_{23,matched}$, where WPT system can achieve the maximum efficiency can be calculated as:

$$k_{23,matched} = \sqrt{\left(k_{12}^2 - k_{13}^2\right)^2 Q_1^2 - Q_2^{-2}} \tag{6.3}$$

Similarly, the two-coil WPT system can be modelled by this method as well by deleting the feed/load loops. The PTE degrades as the k_{23} vary from its optima caused the impedance mismatch. However, the WPT system is desired to have a PTE over a large range of the transfer position. Therefore, matching the variable impedance is the key challenge in achieving high PTE range-adaptive WPT systems.

PTE and Transfer Distance

The analysis of mutual coupling between two resonant circuits has been well established [19] – [23]. For the two-coil MRC-WPT technology, the magnetic coupling coefficient k_{12} between two coils with radians of r_{Tx} and r_{Rx} can be described with the transfer distance d as [24]:

$$k_{12} = \frac{1}{\left[1 + 2^{\frac{2}{3}}\left(d / \sqrt{r_{Tx} r_{Rx}}\right)^2\right]^{\frac{3}{2}}} \tag{6.4}$$

In [23], a transmitter coil (with a diameter of 30 cm and a Q-factor of 1270) and a receiver coil (with a diameter of 20 cm and a Q-factor of 1100) are used to transfer a power of 105 W over 30 cm. A system PTE of 77% has been achieved in this case when the dimension of the transmitter coil and the transfer distance are the same. But if the transfer distance exceeds the transmitter coil dimension, the PTE will fall rapidly as predicted by (6.1) – (6.3).

The transfer coefficient S_{21} can be used as an indicator of PTE performance which can be described in a two-coil system as:

$$\begin{aligned} S_{21} &= 2\frac{V_L}{V_S}\sqrt{\frac{R_S}{R_L}} = 2\frac{I_L R_L}{V_S}\sqrt{\frac{R_S}{R_L}} \\ &= \frac{2j\omega M_{TR}\sqrt{R_S R_L}}{M_{TR}^2\omega^2 + \left(j\omega L_T + \frac{1}{j\omega C_T} + R_S\right)\cdot\left(j\omega L_R + \frac{1}{j\omega C_R} + R_L\right)} \end{aligned} \tag{6.5}$$

When the Tx and Rx coils are both designed to resonate at the same frequency, the transfer coefficient can be simplified to:

$$S_{21} = \frac{2j\omega_0 M_{TR}\sqrt{R_S R_L}}{M_{TR}^2\omega_0^{\ 2} + R_S R_L} \tag{6.6}$$

The optimal input impedance seen by the source should be:

$$R_{In,opt} = \frac{\omega_0^2 M_{TR}^2}{R_L} \tag{6.7}$$

Therefore, the impedance matching should rely on the value of the mutual inductance. The relationship between the mutual inductance and transfer distance, and the corresponding frequency response can be plotted as shown in Fig. 6-3 and Fig. 6-4:

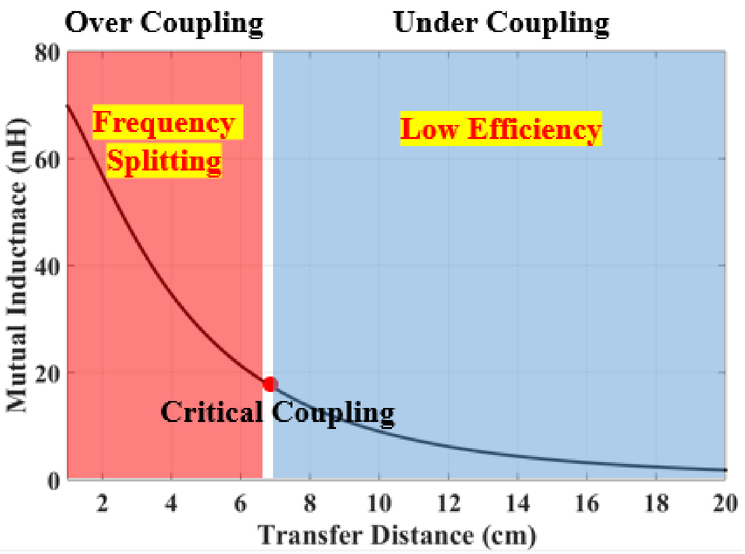

Fig. 6-3. The relationship between the transfer distance and mutual inductance.

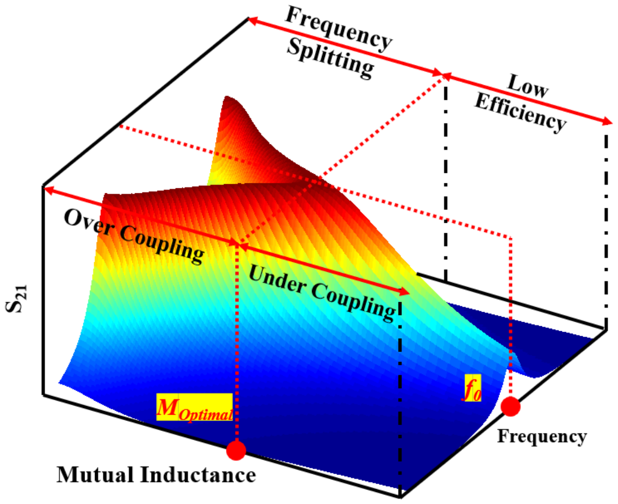

Fig. 6-4. Frequency response with the variation of the mutual inductance.

The frequency splitting phenomena can be observed when the transfer distance is small where the mutual inductance is strong. When the separation between the Tx and Rx increases to a certain value, the mutual inductance will be reduced to its optimal value where the maximum PTE of the system can be achieved. This coupling condition is known as critical coupling. Once the distance increases from critical coupling position, the mutual inductance degrades, and the PTE drops rapidly as described in (6.2).

Herein, the key to achieving range-adaptive WPT performance is getting a mutual inductance that inmate to the transfer position variation and the value of which can be kept at its optimal one in (6.3).

6.1.2 Range-Adaptive WPT Impedance Matching Techniques

Several techniques have been proposed in the literature. In [25], a multi-loads WPT system using relay resonators with intermediate coils has been reported. Different coils are optimized for different transfer distance and served as receiver and relays simultaneously. Frequency tuning method is adopted in [26] to make the use of frequency splitting phenomena as the system will alternate the operating frequency when the transfer position is changing to achieve the maximum PTE. The three-dimensional structure is used in [27] to transfer the power omnidirectional achieving a range-adaptive WPT. The beamforming loop array is reported in [28] by controlling the loop current and selecting the appropriate resonant capacitance for high PTE. Overall, there are two directions to solve the impedance matching problem in the range-adaptive WPT, namely, variation adaptive matching where the matching method will try to satisfy the different optimal impedance at different transfer positions to achieve outstanding performance, and variation compress matching where the technique will try to avoid the impedance variation with respect to the position change.

Adaptive Matching Methods of Variable Impedances

Jungsik Kim *et al* presented a range-adaptive WPT system using multi-loop and tunable matching circuit [21]. The multi-loop structure is applied to adapt the variation in the input impedance of the WPT system with regards the transfer distance, where one of the four loops with a different size is selected, depending on the transfer distance. It enables the design of a simple tunable matching circuit using a single variable capacitor. The proposed topology and fabricated circuit are shown in Fig. 6-5:

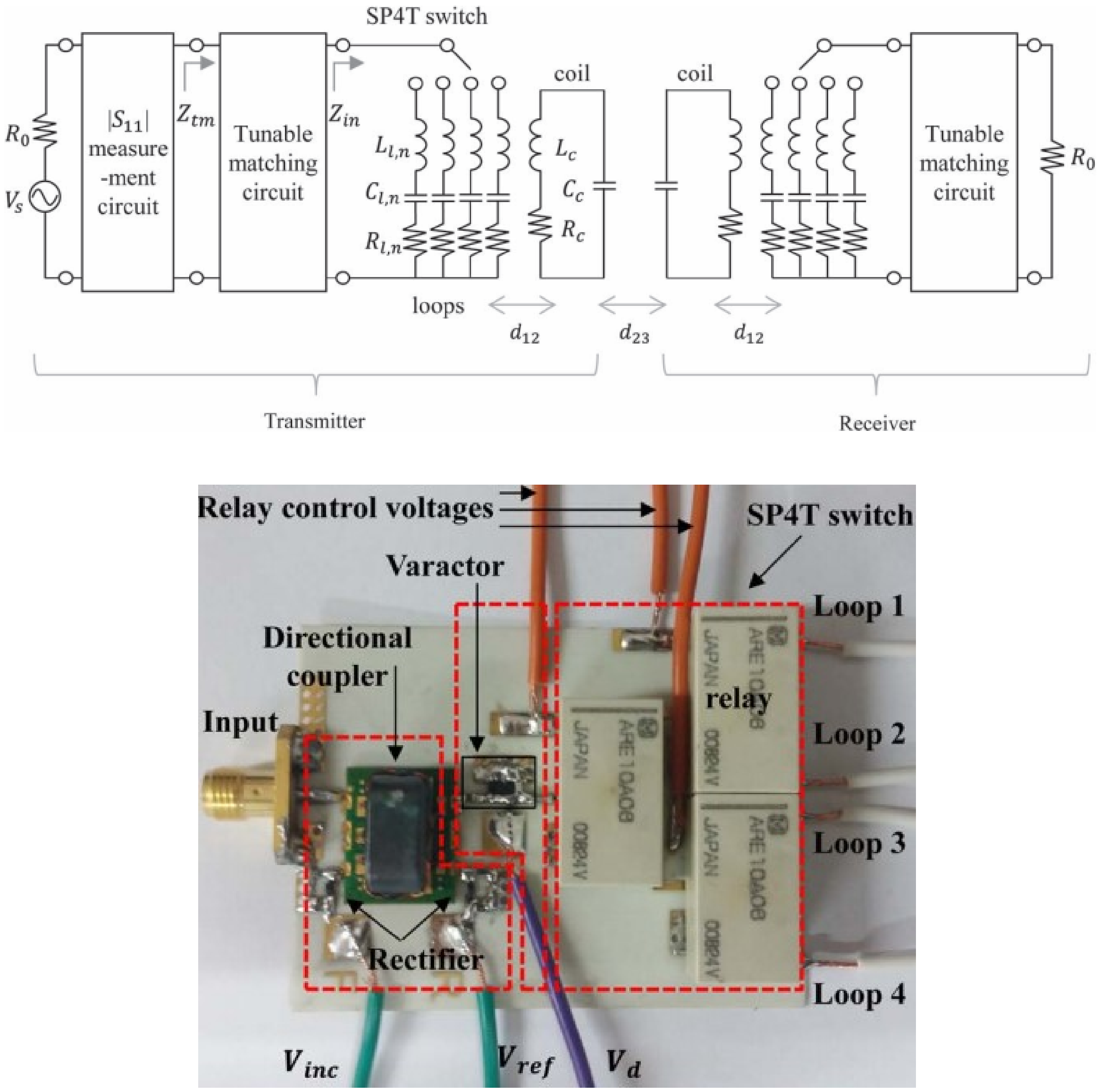

Fig. 6-5. The schematic of the multiloop structure and fabricated circuit [21].

This design used four different transmitting and receiving resonant coils optimized for four different transfer distances. When the transfer distance is varying, the system will automatically select a proper transmitter/receiver pair and tune the required resonant capacitor. The results are shown in Fig. 6-6:

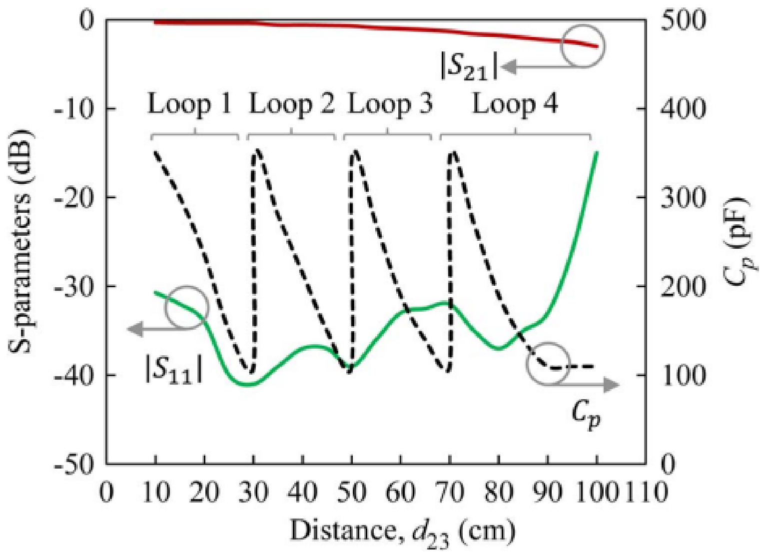

Fig. 6-6. Required capacitance for the impedance matching as a function of the distance including the S_{11} and S_{21} response [21].

This method used active tuning circuits and multi-loop structure to match the impedance adaptively. The performance of this work is promising, and the measured results show a range-adaptive operation with PTE better than 48% up to a transfer distance of 100 cm. However, it should be noticed that the system is complex as multiple resonant coils are required and the impedance tuning unit is necessary. In this case, the overall efficiency of the system will be relatively low as the impedance tuning unit is energy consuming. Moreover, the complexity as well as the cost of the system should be considered. Therefore, the impedance variation adaptive matching in WPT may not be a competitive candidate for the applications require high PTE.

Matching Methods based on Constraining the Variable Impedances

Yue-Long Lyu *et al* presented a WPT system using nonidentical resonant coils for frequency splitting elimination to achieve a range-adaptive power transfer [29]. In this work, two nonidentical resonant coils (NIRCs) are used as a wireless power transmitter and receiver, respectively. Based on the elliptic integral term in the analytical expression, the impedance variation with respect to the transfer distance can be limited by using the two NIRCs. Due to the size difference between the transmitter and receiver coil is comparable with the transfer distance, the mutual inductance change regards the transfer distance can be compressed significantly. The comparison of the NIRCs and conventional identical coil design has been displayed in Fig. 6-7:

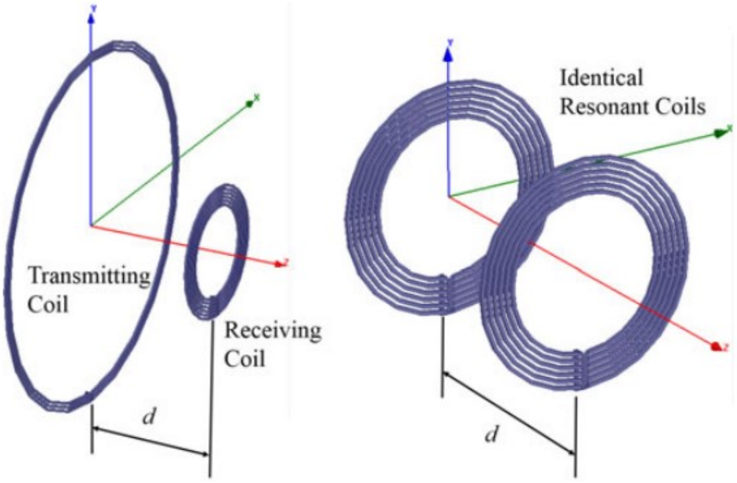

Fig. 6-7. Comparison between the NIRCs and identical resonant coils [29].

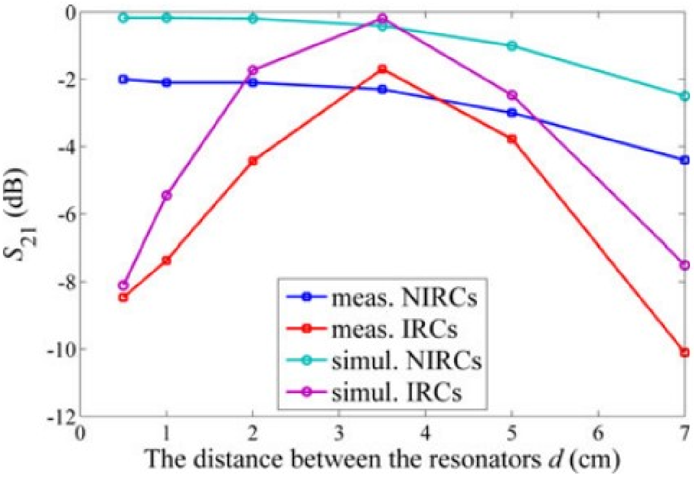

Fig. 6-8. Transfer coefficient S_{21} contrast between the NIRCs and identical resonant coils [29].

The Fig. 6-8 shows that the efficiency of the close transfer distance is improved significantly compared to the identical resonant coils structure. The measured results show a transfer efficiency of 39% - 62% with a transfer range from 0.5 cm to 7 cm. However, due to the requirement that the size difference between the transmitter and receiver coil should be comparable to the transfer distance. This method requires large coil size or small transfer distance range. Otherwise, the method may not be valid. Moreover, the achieved transfer efficiency is not promising which is limited by the small Q value as the receiver used in this method is very small leading to a small inductance.

Wang-Sang Lee *et al* proposed a contactless WPT system using antiparallel resonant loops to compress the frequency splitting and achieve the range-adaptive high-efficiency performance [30]. This structure employed a transmitter containing a set of forward and reverse loops forming an antiparallel resonant coil to stabilise the impedance variation caused by the changing of transfer distance. Due to the mutual inductance is very large when the transmitter and receiver are placed close to each other. This structure will degrade the excessive coupling at close distance, constraining the impedance variation. The realized mutual inductance between the transmitter and receiver against the transfer distance is shown in Fig. 6-9:

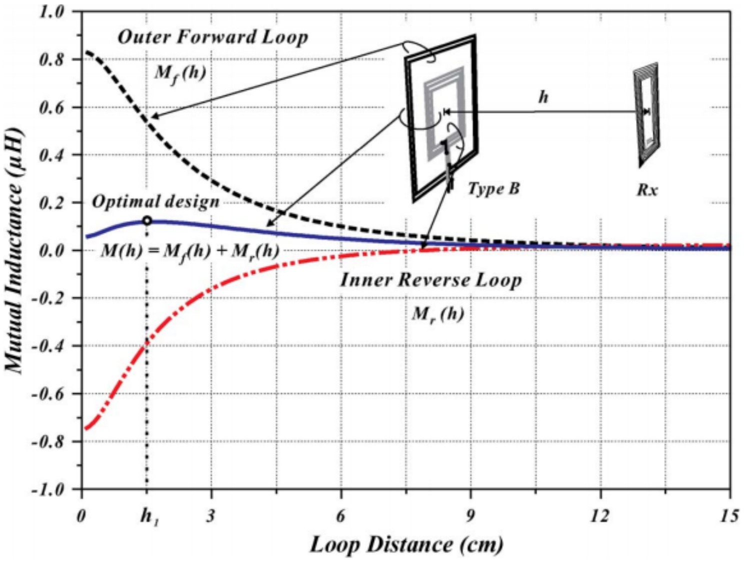

Fig. 6-9. Mutual inductance regards the loop distance of the antiparallel loops [30].

The realized mutual inductance is compressed significantly along the loop distance by using the mutual inductance difference between the forward and reverse loop. Therefore, the stable output power performance can be expected. The measured efficiency is shown as Fig. 6-10:

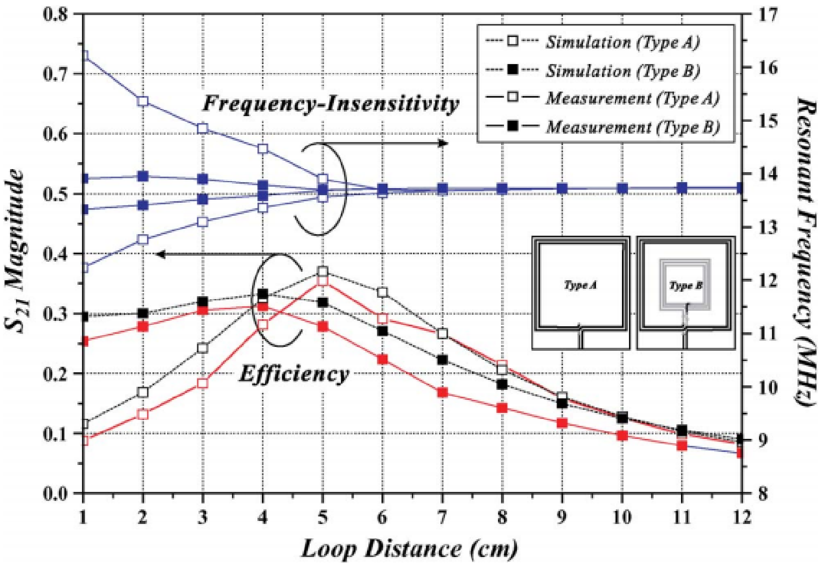

Fig. 6-10. Simulated and measured results of the antiparallel loops [30].

It is obvious that the frequency splitting has been compressed significantly by the antiparallel loop structure. However, the peak S_{21} achieved by the work is around 35% due to that the mutual inductance is only be compressed but the optimal matching criterion has not been met perfectly.

In conclusion, the section has introduced the basic theory of the WPT system and analysed the challenges in realising a high-efficiency range-adaptive WPT system. State-of-the-art WPT designs dealing with the position variation problem have been introduced in detail. The key point to achieving range-adaptive WPT performance is getting a mutual inductance that will not vary with the transfer position changes and the value of which can be kept almost constant at its optimal.

6.2 Introduction of Novel WPT System Design

WPT systems via strongly coupled magnetic resonances (CMR) have shown a breakthrough in high-efficiency WPT applications [31], [32]. However, the resonant condition is a critical requirement of achieving maximum power transfer efficiency (PTE) between the transmitter (Tx) and receiver (Rx). The resonant condition of a given CMR-WPT system is usually fixed. Once the transfer position of the system varies from the optimum one, the PTE of the system will decrease significantly. In this work, the "distance" is defined as the space between the two planes where the Tx and Rx are located. The "horizontal misalignment" refers to the displacement of the centre points of the Tx and Rx along the parallel planes. A shorter transfer distance (*h)* between Tx and Rx would cause over-coupling where the excessive coupling will split the resonant frequency. It weakens the PTE level at the original resonant frequency [33] – [35]. A larger transfer distance or a horizontal misalignment (*d*) would reduce the coupling, leading to the impedance mismatch and degrade the PTE too. Many applications such as the charging of biomedical bioelectronic device [36] – [42], electric vehicles [43], [44] and mobile electronics [45], [46] would require the flexibility of the transfer position and a high PTE simultaneously. Ideally, WPT systems should have a high PTE regardless of the transfer position variation [47], [48].

Recently, many methods have been presented to address this issue such as adaptive frequency tracking [31], [32], [49], [50] impedance control circuit [51], metamaterial [36], [37] and switching coils with different transfer distances [51], [52]. However, the added control or switching circuits will significantly increase the complexity of the system and reduce the overall system operating efficiency. Lee *et al* presented an antiparallel resonant loop structure to eliminate the frequency splitting by weakening the excessive coupling caused by the short transfer distance [53]. However, the maximum PTE will only be achieved at an optimal transfer distance, and the anti-misalignment ability was not discussed. Chen *et al* used the multiple-input and multiple-output concept with a multi-transmitter and array system [54]. Assawaworrarit *et al* applied a nonlinear parity-time-symmetric circuit to achieve robust WPT. Excellent range-adaptive performance has been achieved [55]. But active circuits are needed, and the resonant frequency was adaptively changed to maintain high PTE. It can be a great limitation for WPT applications. A reconfigurable system is used to further increase PTE in conforming to charging device positions [56], [57]. However, there is no optimal solution for a WPT system to achieve high PTE under both transfer distance variation and horizontal misalignment conditions simultaneously. Thus, how to design high-efficiency range-adaptive WPT systems without active control is still very challenging.

This work aims to investigate a method to solve this challenge. Here we present a planar Tx structure with multiple bi-directional sub-coils to maintain the resonant condition of the CMR-WPT system. We show theoretically and demonstrate experimentally that the proposed Tx structure can achieve a relatively constant mutual inductance between Tx and Rx over a broad range of transfer distance and misalignment variation without the need for any impedance tracking or active control circuits. The design concept will be described, and a robust mathematical model will be established for the optimisation of the structure.

This chapter is organized as follows. In section 6.3, the basics of a two-coil MRC-WPT operating principles are analysed in detail with the derivation of formulas. The challenges of high-efficiency position-free WPT are identified. In Section 6.4, the proposed multiple bi-directional resonant coils structure will be introduced with theoretical analysis and numerical simulation, A comparison with the conventional method is discussed. In Section 6.5, a prototype is fabricated. Measurement results are shown and analysed. Conclusions are drawn in Section 6.6 to summarize the chapter.

6.3 Theoretical Analysis

6.3.1 Two-Coil MRC-WPT Operating Principle

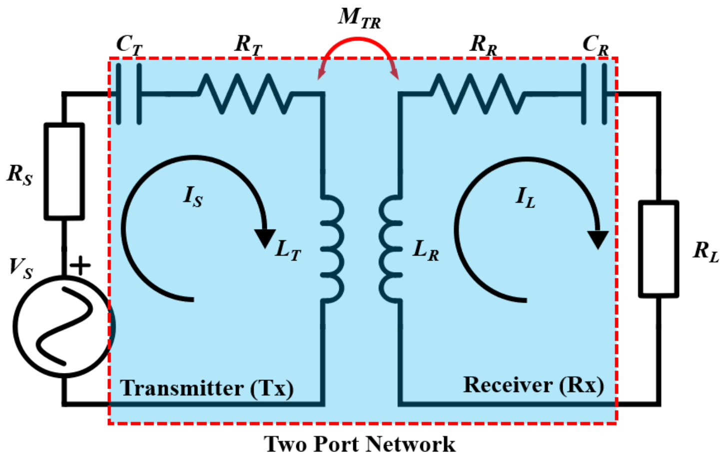

Fig. 6-11. Equivalent circuit of a typical two-coil MRC-WPT system.

An equivalent circuit of a typical two-coil CMR-WPT system is depicted in Fig. 6-11. R_S, R_L, L_T, L_R, R_T, R_R, C_T, C_R, and M_{TR} are the source resistance, load resistance, coils' self-inductance, coils' radiative and ohmic losses, resonating capacitor and mutual inductance of the Tx and Rx respectively. For simplicity, assuming a lossless case, $R_T = R_R = 0\ \Omega$, the ratio of the received power on the load P_L and the input power P_S, namely, PTE is [35]:

$$\eta = \frac{P_L}{P_S} = |S_{21}|^2 \times 100\% \tag{6.8}$$

The node equations of the circuit based on Kirchhoff's voltage law can be built as:

$$\left(R_S + j\omega L_T + \frac{1}{j\omega C_T}\right)I_S - j\omega M_{TR} I_L = V_S \tag{6.9}$$

$$\left(R_L + j\omega L_R + \frac{1}{j\omega C_R}\right)I_L - j\omega M_{TR} I_S = 0 \tag{6.10}$$

where ω represents the angular frequency of the system in radius. Combining (6.9) and (6.10), the current flow through the Rx loop can be obtained as:

$$I_L = \frac{j\omega M_{TR} V_S}{\omega^2 M_{TR}{}^2 + \left(j\omega L_T + \frac{1}{j\omega C_T} + R_S\right)\cdot\left(j\omega L_R + \frac{1}{j\omega C_R} + R_L\right)} \tag{6.11}$$

Then the transmitting coefficient can be calculated as:

$$\begin{aligned} S_{21} &= 2\frac{V_L}{V_S}\sqrt{\frac{R_S}{R_L}} = 2\frac{I_L R_L}{V_S}\sqrt{\frac{R_S}{R_L}} \\ &= \frac{2j\omega M_{TR}\sqrt{R_S R_L}}{M_{TR}^2\omega^2 + \left(j\omega L_T + \frac{1}{j\omega C_T} + R_S\right)\cdot\left(j\omega L_R + \frac{1}{j\omega C_R} + R_L\right)} \end{aligned} \tag{6.12}$$

If the circuit is operating at the resonant frequency ω_0 with the following requirement satisfied on both Tx and Rx side:

$$\omega_0 = \frac{1}{\sqrt{L_T C_T}} = \frac{1}{\sqrt{L_R C_R}} \tag{6.13}$$

Then, (6.5) can be simplified to:

$$S_{21} = \frac{2j\omega_0 M_{TR}\sqrt{R_S R_L}}{M_{TR}^2\omega_0{}^2 + R_S R_L} \tag{6.14}$$

It can be observed form (6.14) that the power transferred to the load is heavily dependent on the magnitude of the mutual inductance between the Tx and Rx. To yield the maximum PTE to the load, an optimal mutual inductance should be achieved critically as:

$$M_{Optimal} = \frac{\sqrt{R_S R_L}}{\omega_0} \tag{6.15}$$

For a given source/load termination value, the relationship between S_{21}, the mutual inductance and the frequency can be plotted as shown in Fig.6-12. It can be seen from the plot that the maximum PTE operation at the desired resonating frequency can only be achieved when the mutual inductance is $M_{Optimal}$. When the system is operating under over coupling conditions, the resonating frequency will be split into two. The PTE at the desired frequency will be degraded significantly due to the excessive coupling between Tx and Rx. On the other hand, when the system is working at under coupling conditions, the desired resonant frequency will be maintained but the PTE will drop dramatically due to the weak coupling. Hence, to transfer the power with the maximum PTE at the desired resonating frequency, the mutual inductance must be maintained at $M_{Optimal}$.

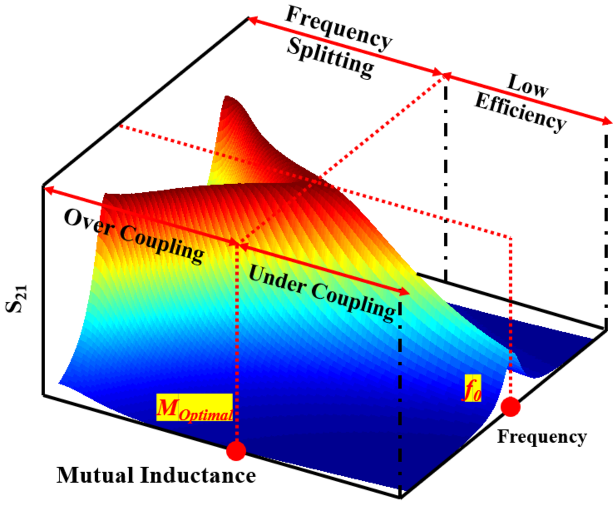

Fig. 6-12. Typical relationship between S_{21}, mutual inductance and resonant frequency.

6.3.2 Transfer Position and Mutual Inductance

The Tx and Rx of the MRC-WPT can be realized by using multi-loop circular coils connected in series with a capacitor to resonate. To calculate the mutual inductance between the Tx and Rx, a multi-loop coil can be simplified to a set of concentric single-loop coils. Each single loop can be further simplified to a filamentary coil as shown in Fig. 6-13. N_T, N_R, r_{Ti} and r_{Rj} denote the number of loops, and radius of each single-loop coil for the Tx and Rx, respectively. The mutual inductance M_{ij} between the i^{th} single Tx loop and j^{th} single Rx loop can be expressed as a function of the transfer distance *h,* horizontal misalignment *d,* by the equation [58]:

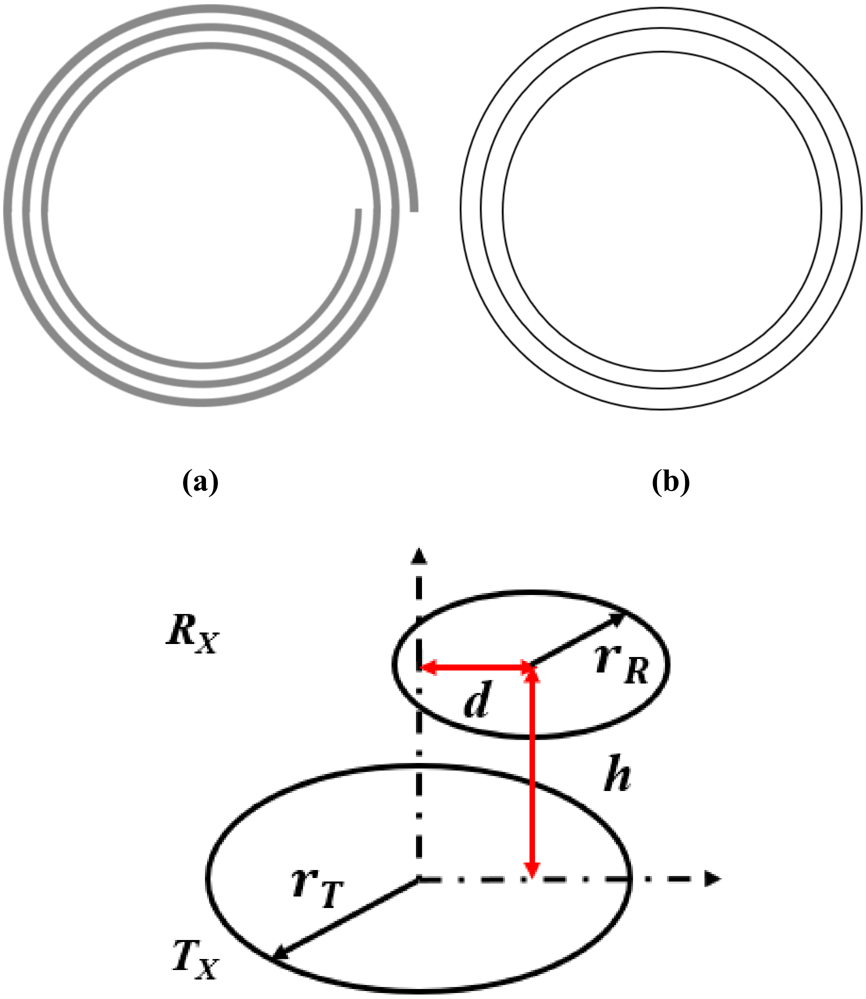

(a) **(b)**

(c)

Fig. 6-13. (a) A multi-loop circular coil, (b) a set of single-loop filament coils, (c) simplified single-loop filamentary Tx/Rx coil configuration.

N_T, N_R, r_{Ti} and r_{Rj} denote the number of loops, radius of each single-loop coil for the Tx and Rx. The mutual inductance M_{ij} between the i^{th} single Tx loop and j^{th} single Rx loop can be expressed as a function of the transfer distance *h,* horizontal misalignment *d,* by the equation [53]:

$$M_{ij}\left(r_{Ti}, r_{Rj}, h, d\right) = \frac{\mu_0\sqrt{r_{Ti}r_{Rj}}}{2\pi}\int_0^{2\pi}\frac{1-\frac{d}{r_{Rj}}\cos\left(\phi\right)}{C}\Lambda\left(k\right)d\phi \tag{6.16}$$

where the parameters in (6.16) can be expressed as:

$$C = \left(1+\frac{d^2}{r_{Rj}^2}-\frac{d}{r_{Rj}}\right)^{\frac{3}{4}} \tag{6.17}$$

$$\Lambda\left(k\right) = \left(\frac{2}{k}-k\right)K\left(k\right)-\frac{2}{k}E\left(k\right) \tag{6.18}$$

$$k = \sqrt{\frac{4\alpha C^{\frac{4}{3}}}{\left(1+\alpha C^{\frac{4}{3}}\right)^2+\beta^2}} \tag{6.19}$$

$$\alpha = \frac{r_{Rj}}{r_{Ti}}, \beta = \frac{h}{r_{Ti}} \tag{6.20}$$

where $\mu_0 = 4\pi\times10^{-7}$ H/m is the magnetic constant, *K(k)* and *E(k)* are the complete elliptic integrals of the first and second kind respectively [53]. Hence the total mutual inductance between Tx and Rx with the number of the turns are N_T and N_R can be calculated as:

$$M_{TR} = \sum_{j=1}^{N_R}\sum_{i=1}^{N_T}M_{ij}(r_{Ti}, r_{Rj}, h, d) \tag{6.21}$$

Herein, for a given two-coils MRC-WPT system, there only exists one optimal position regards *h* and *d* which can achieve the total mutual inductance M_{TR} between Tx and Rx equal to $M_{Optimal}$ yielding the maximum PTE at the desired resonating frequency. Both variation in transfer height and horizontal misalignment will introduce a degradation in efficiency as the mutual inductance is very sensitive to the transfer position as shown in (6.16). Therefore, a mutual inductance that robust to the transfer position is essential to realize a position-free high-efficiency WPT system.

6.4 Bidirectional Resonant Coils Design and Simulations

6.4.1 Smooth Mutual Inductance Against Transfer Position

By combining (6.14) and (6.21), the relationship between the transmission coefficient and the transfer position including both transfer distance and misalignment can be obtained as shown in Fig.6-14. It can be observed that for different Tx coil sizes coupled with the same Rx coil, the mutual inductance will generally decrease with the increase of either transfer distance or misalignment. For any Tx size, there exists one optimal transfer distance or horizontal misalignment where the maximum S_{21} can be achieved. It indicates that a given CMR-WPT system will have a fixed optimal transfer position.

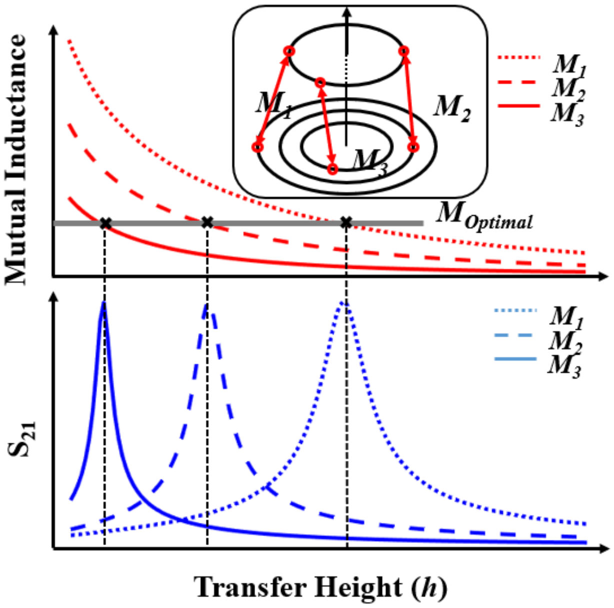

(a)

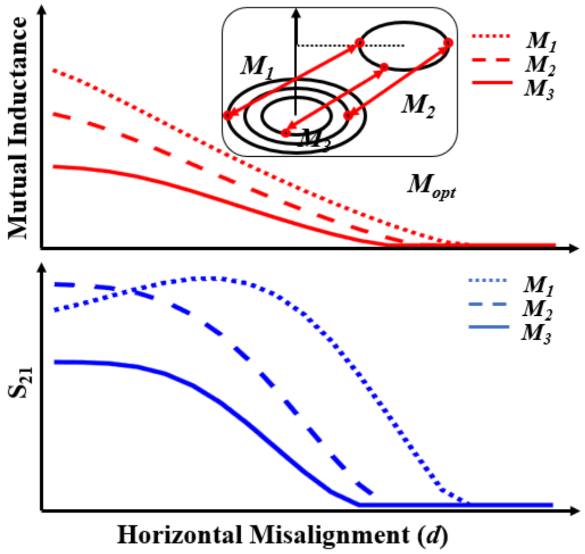

(b)

Fig. 6-14. Mutual inductance and S_{21} against the variation of (a) transfer height, (b) horizontal misalignment for different Tx coil sizes with the same Rx.

The maximum S_{21} can be only achieved when the $M_{Optimal}$ is obtained. Either excessive or weak coupling will decrease the PTE at the original resonating frequency. For different Tx size, there exists one optimal transfer height that can ensure the maximum S_{21} for the system. A larger Tx size will result in a longer optimal transfer height. With the misalignment condition, the efficiency of the medium and small size Tx with drop with *d* increase due to the $M_{Optimal}$ cannot be achieved even without the misalignment. However, the efficiency of the large Tx coil increases from a relatively low level when the misalignment is small and reaches a maximum then starts decreasing when the misalignment is getting larger. This because the mutual inductance is large when *d* is small which resulting in over coupling and with an increase of *d*, the $M_{Optimal}$ is obtained and then it drops from its optimal value.

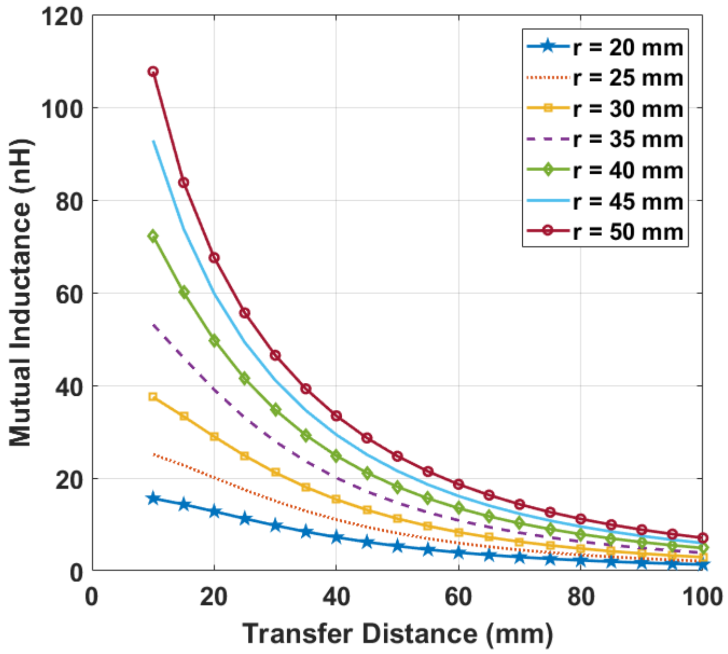

(a)

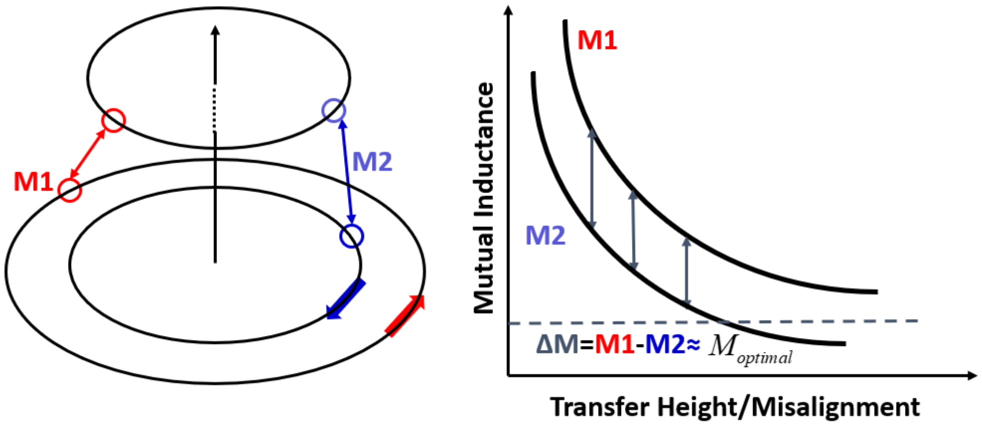

(b) (c)

Fig. 6-15. (a) Mutual inductance variation with the transfer distance of different Tx sizes with the same Rx (b) Tx and Rx configuration, (c) Ideal case of mutual inductance variation against the transfer position of coils with different sizes.

While the mutual inductance magnitudes of different Tx coil sizes are not identical, the degradation trends of which are similar for both transfer height and misalignment conditions as shown in Fig. 6-15. Therefore, it is not easy to smooth the mutual inductance magnitude against the transfer height and misalignment if only designing the coil size or the number of the loops.

6.4.2 Proposed Structure Analysis and Design

Noticed that the mutual inductance magnitude difference between different coil sizes is relatively robust to the transfer height and misalignment as shown in Fig. 6-15. Thus, if the currents fed into the different size coils are oriented in opposite direction, the total mutual inductance M_{total} between Tx and Rx can be represented by the difference of the mutual inductance of different size coils. Then just need to optimize the M_{total} to equal to $M_{Optimal}$, the position-free high-efficiency feature can be realized.

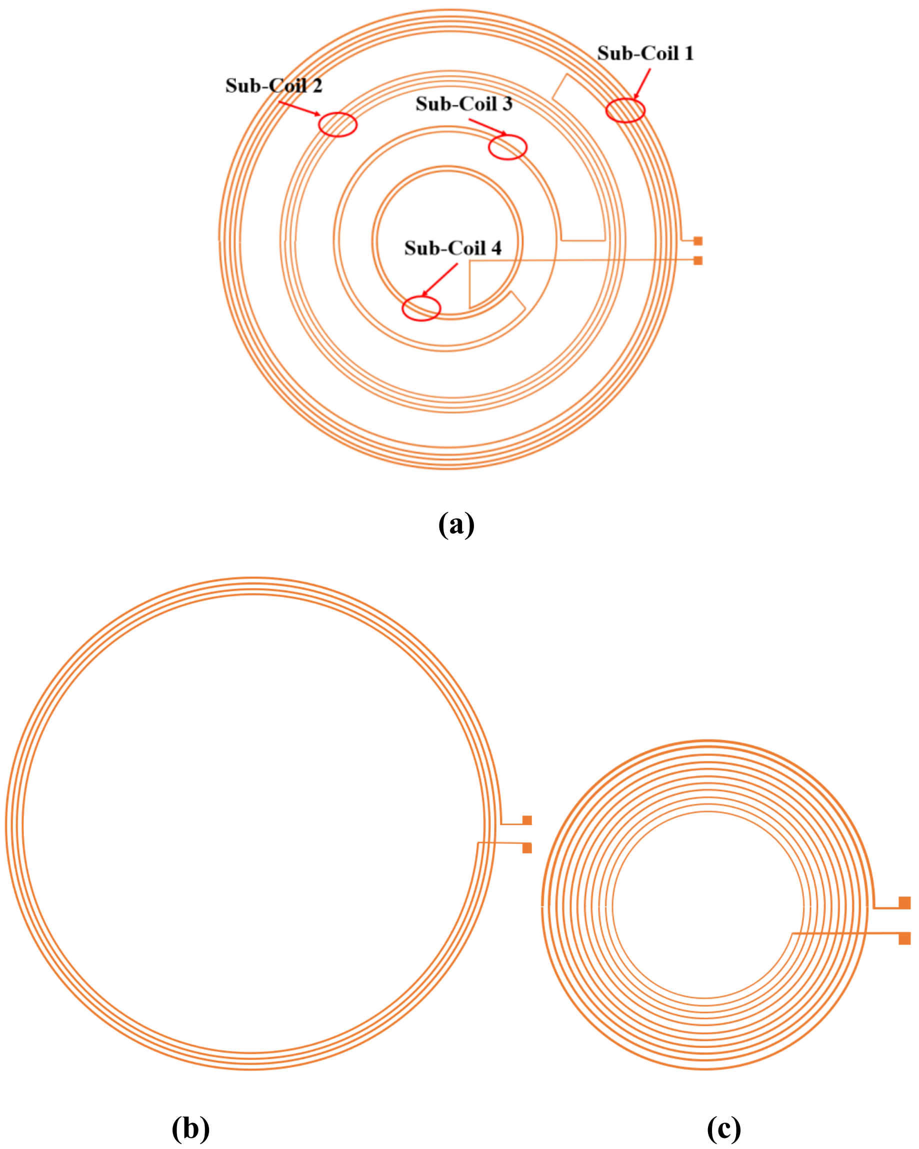

(a)

(b) (c)

Fig. 6-16. Tx and Rx structures (a) proposed bi-directional Tx, (b) conventional unidirectional Tx, (c) unidirectional Rx.

The mutual inductance between each sub-coil in the Tx and the Rx will decrease with the increase of the transfer distance or misalignment. The sub-coils in the Tx have two opposite directions. The mutual inductance between Tx sub-coils of one direction and the Rx has an overall mutual inductance M_{one}. The mutual inductance between Tx sub-coils of the other direction and the Rx has an overall mutual inductance M_{other}. The total mutual inductance M_{total} will be the difference of M_{one} and M_{other}. Although both M_{one} and M_{other} will decrease with the increase of the transfer distance or misalignment, by properly designing the sub-coils, M_{total} can be maintained relatively constant. For example, for Tx with different sizes, the simulated mutual inductance variation with the transfer distance via (6.16) is shown in Fig.6-15 (a). Although the magnitude of the mutual inductances of different Tx are not identical, they follow a similar degradation trend. If the currents fed into two coils of the different size are of opposite directions, the total mutual inductance M_{total} can be depicted by Fig.6-15 (b) and (c). An M_{total} that is robust to the transfer position can be realized. M_{total} can be optimized to approach $M_{Optimal}$. Once the optimal mutual inductance of the system is obtained by (6.15), the task resides in realising the desired mutual inductance by choosing a proper coil size, the number of sub-coils and the number of loops in each sub-coil for the Tx and current direction in each sub-coil, depending on the size and shape of the Rx. To ensure that current can flow in both directions, the Tx sub-coils are oriented in a bi-directional manner. The coils on the Rx are unidirectional. In the practical design, the Tx consists of X sub-coils. Each sub-coil has N_{Ti} loops with an average radius of r_{Ti}. The X sub-coils are connected in series with adjacent sub-coils wounded in opposite directions as shown in Fig.6-16 (a). Four sub-coils are used in this design. A capacitor is connected to the coil to form a resonator. Therefore, the total mutual inductance between Tx and Rx of the proposed structure can be calculated as:

$$M_{total} = \sum_{n=1}^{X} \sum_{j=1}^{N_R} \sum_{i=1}^{N_{Tn}} (-1)^{n-1} M_{ij}(r_{Ti}, r_{Rj}, h, d) \tag{6.22}$$

The total mutual inductance can be simplified by central approximation which uses the average coil size to represents each loop in the same coil. Herein, (6.22) can be approximated as:

$$M_{total} \approx \sum_{n=1}^{X} (-1)^{n-1} N_R N_{Tn} M_n(r_{Tn}, r_R, h, d) \tag{6.23}$$

Where M_n represents the mutual inductance between the n^{th} transmitter coil and receiver coil. The Rx coil loops number is designed to be fixed in this work. The design parameters of every coil are chosen empirically based on the desired transfer range and size requirement of the applications. The robustness of the mutual inductance against the transfer position can be obtained by optimizing the number of loops in every coil of Tx, and the differentiation-based method can be applied. Due to the mutual inductance slopes against the transfer height and misalignment are not identical, the optimization process regards the height and misalignment should be separated. Let assume the condition without the misalignment where $d = 0$ mm. If the total mutual inductance M_{total} (h) changes slowly against transfer height h, the differentiation of M_{total} (h) regards h should be close to zero. Assume that the desired transfer height range of the smooth mutual inductance is denoted by the interval [h_1, h_2], and Y samples are selected in the interval [h_1, h_2]. At the m^{th} sample h_m, it is desired to achieve:

$$\sum_{n=1}^{X}(-1)^{n-1}N_R N_{Tn}\frac{dM_n(h)}{dh}\bigg|_{h=h_m}=0 \tag{6.24}$$

On the other hand, let assume the transfer height h is constant and now the total mutual inductance M_{total} (d) changes slowly against misalignment d, the differentiation of regards d should be close to zero. Thus, the differentiation of the mutual inductance regards d at the q^{th} sample d_q in the desired misalignment range [d_1, d_2] should satisfy:

$$\sum_{n=1}^{X}(-1)^{n-1}N_R N_{Tn}\frac{dM_n(d)}{dd}\bigg|_{d=d_q}=0 \tag{6.25}$$

For Y samples in the interval [h_1, h_2], a matrix can be constructed based on (6.24), namely:

$$\overline{\overline{MH}}\,\overline{U}=\overline{0} \tag{6.26}$$

Where $\overline{U}$ is a vector consisting of the number of loops for every Tx coil and $\overline{\overline{MH}}$ is a matrix whose element in row m and column n can be represented by

$$M_{m,n}=(-1)^{n-1}N_R\frac{dM_n(h)}{dh}\bigg|_{h=h_m} \tag{6.27}$$

Similarly, a matrix $\overline{\overline{MD}}$ for misalignment condition whose element in row q and column n represented by

$$M_{m,n} = (-1)^{n-1} N_R \left.\frac{dM_n(d)}{dd}\right|_{d=d_q} \tag{6.28}$$

Now, the optimal loops number for each coil against the transfer height and misalignment can be found by solving the following equations:

$$\begin{bmatrix} N_R \left.\frac{dM_1(h)}{dh}\right|_{h=h_1} & \cdots & {}^{-1}N_R \left.\frac{dM_n(h)}{dd}\right|_{h=h_1} \\ \vdots & \ddots & \vdots \\ N_R \left.\frac{dM_1(h)}{dh}\right|_{h=h_m} & \cdots & {}^{-1}N_R \left.\frac{dM_n(h)}{dh}\right|_{h=h_m} \end{bmatrix} \begin{bmatrix} N_{T1} \\ \vdots \\ N_{Tn} \end{bmatrix} \begin{bmatrix} 0 \\ \vdots \\ 0 \end{bmatrix}$$

$$\begin{bmatrix} N_R \left.\frac{dM_1(d)}{dd}\right|_{d=d_1} & \cdots & {}^{-1}N_R \left.\frac{dM_n(d)}{dd}\right|_{d=d_1} \\ \vdots & \ddots & \vdots \\ N_R \left.\frac{dM_1(d)}{dd}\right|_{d=d_q} & \cdots & {}^{-1}N_R \left.\frac{dM_n(d)}{dd}\right|_{d=d_q} \end{bmatrix} \begin{bmatrix} N_{T1} \\ \vdots \\ N_{Tn} \end{bmatrix} \begin{bmatrix} 0 \\ \vdots \\ 0 \end{bmatrix} \tag{6.29}$$

$$\sum_{n=1}^{X} (-1)^{n-1} N_R N_{Tn} M_n(r_{Tn}, r_R, h, d) = M_{Optimal}$$

Finally, the optimal solution can be obtained to maintain the system achieve the desired mutual inductance regardless of the transfer position for the desired range [h_1, h_2] and [d_1, d_2].

6.4.3 Numerical Simulation

Finally, the optimal solution can be obtained so that a constant mutual inductance of the desired value can be achieved for the range of [h_1, h_2] and [d_1, d_2]. To evaluate the proposed structure, a numerical simulation has been performed. The desired optimal range for transfer distance and misalignment are set to $h_1 = 10$ mm, $h_2 = 50$ mm and $d_1 = 0$ mm, $d_2 = 50$ mm respectively. The number of samples used in (6.24) is 5 for both transfer distance and misalignment. The calculated parameters via (6.24) – (6.29) are listed in Table 1.

TABLE I: Design Parameters

Coil	Number of loops	Average radius (mm)	Direction
The proposed system			
N_{T1}	5.2	84.6	Clockwise
N_{T2}	4.2	67.7	Anti-clockwise
N_{T3}	1.8	45.1	Clockwise
N_{T4}	2.2	33.9	Anti-clockwise
N_R	14	45.1	Clockwise
Type I			
N_T	5	45.1	NA
N_R	5	45.1	NA
Type II			
N_T	5	84.6	NA
N_R	4	45.1	NA

The anti-misalignment feature of the proposed system is optimised at h = 50 mm. The mutual inductance between Rx and each sub-coil in Tx, and total mutual inductance of the system against the transfer distance and horizontal misalignment are calculated using (6.16) and shown in Fig. 6-17. For both the transfer distance and misalignment varying from 0 mm to 50 mm, the total mutual inductances are very smooth against the transfer position variation and close to the optimal value. Moreover, the numerical simulation of the misalignment performance against different transfer distances of the proposed system and two conventional designs are plotted in Fig.6-17 (c) – (d).

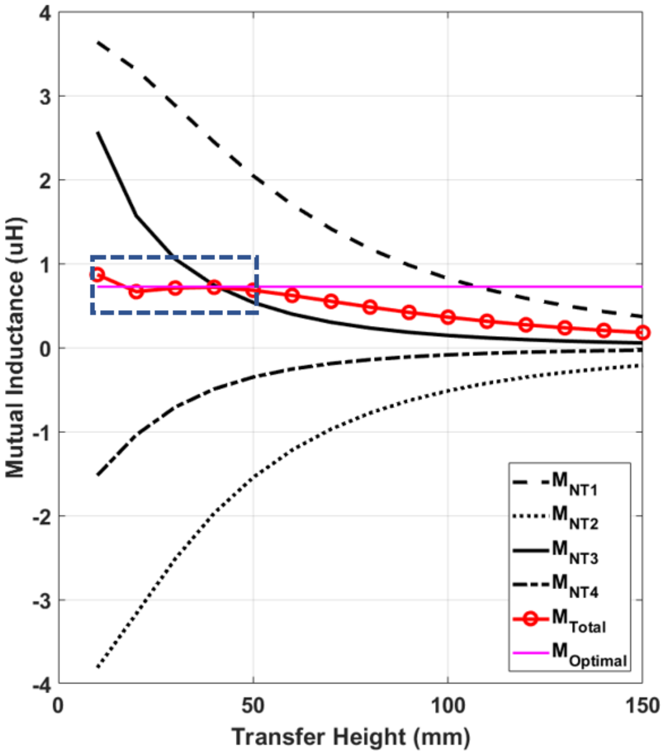
Mutual Inductance (uH)
Transfer Height (mm)
4
3
2
1
0
-1
-2
-3
-4
0
50
100
150
M_NT1
M_NT2
M_NT3
M_NT4
M_Total
M_Optimal

(a)

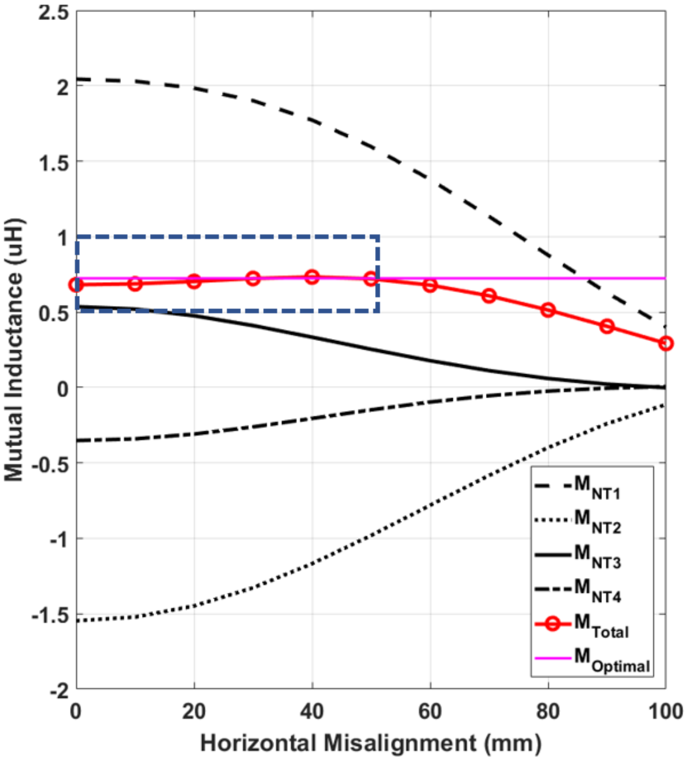
Mutual Inductance (uH)
Horizontal Misalignment (mm)
2.5
2
1.5
1
0.5
0
-0.5
-1
-1.5
-2
0
20
40
60
80
100
M_NT1
M_NT2
M_NT3
M_NT4
M_Total
M_Optimal

(b)

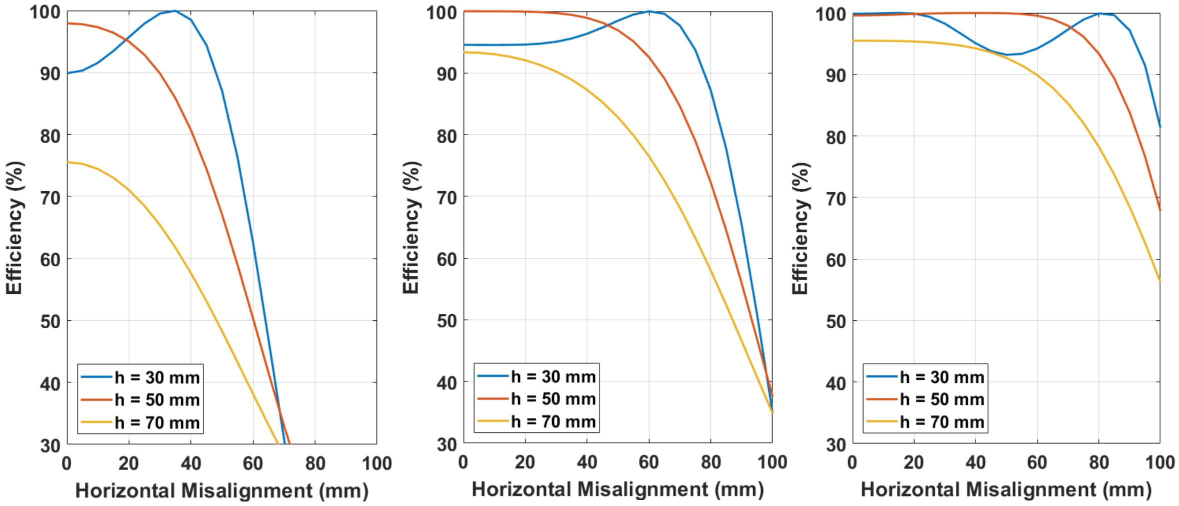

(c)(d)(e)

Fig. 6-17. Optimized flat mutual inductance against the position variation of (a) transfer distance, (b) horizontal misalignment of the proposed Tx structure, and numerical simulation of the misalignment performance with different transfer height (c) Type I, (d) Type II, (e) the proposed system.

The magnitude of the mutual inductance between each Tx coil and the Rx is decreasing with the height or misalignment increasing, and far away from the optimal value. However, for both transfer height and misalignment varying from 0 mm to 50 mm, the total mutual inductances are very smooth and close to the optimal value which validates the proposed design method. Herein, the relationship between S_{21}, transfer height and resonate frequency has been plotted in Fig. 6-18.

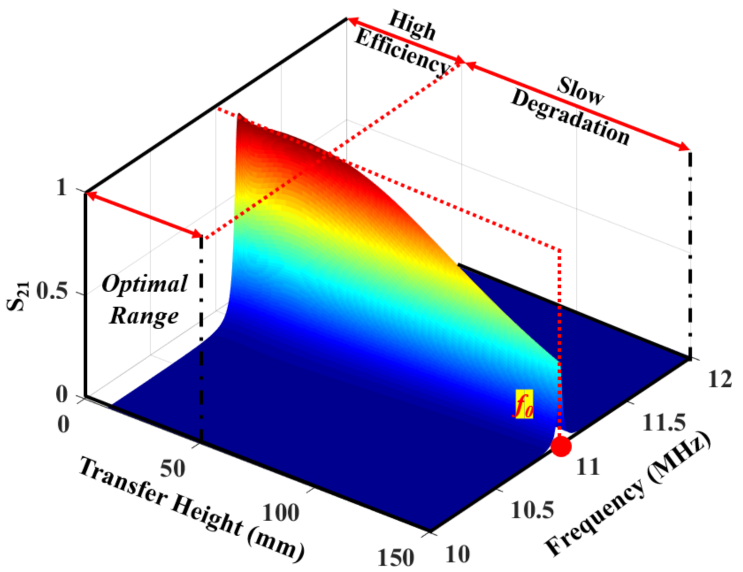

Fig. 6-18. Relationships between S_{21}, resonate frequency and transfer height of the proposed structure.

It can be compared to the performance of a conventional design in Fig. 6-13. that the frequency splitting phenomena have been mitigated and high-efficiency performance has been maintained at the desired resonant frequency for a wide range of transfer height variation. The transfer efficiency of the proposed system has been plotted against the transfer position in terms of height and misalignment as shown in Fig. 6-19.

Herein, the high-efficiency position-free WPT can be realized. It should be noticed that due to the anti-misalignment ability of the design was optimized with h = 50 mm, the optimal performance has been achieved at this height. When the transfer height is very small (< 30 mm), the transfer efficiency against the misalignment will be degraded significantly, though, still with relatively high efficiency better than 60% as shown in Fig. 6-19.

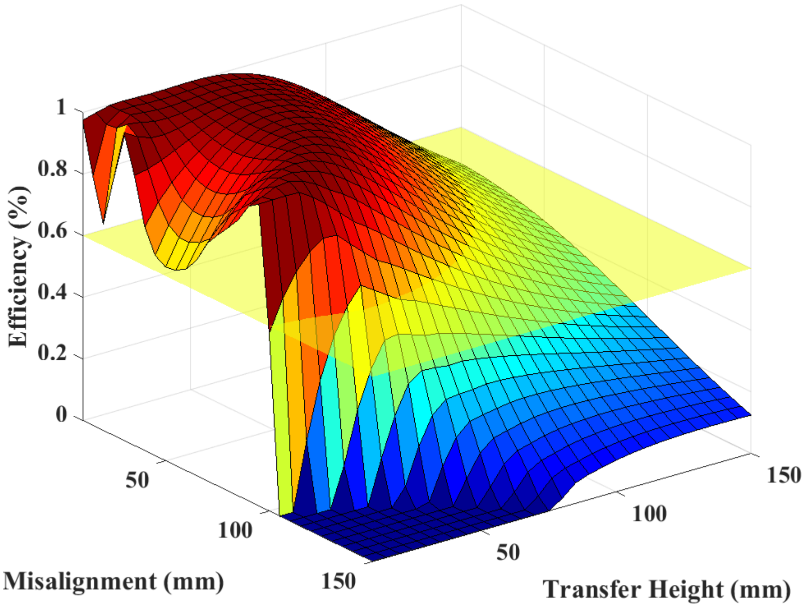

Fig. 6-19. Simulated transfer efficiency of the proposed structure against the transfer height and misalignment with a reference of 60% efficiency.

6.5 Implementation and Measurements

To validate the proposed MRC-WPT structure and design method, a prototype has been fabricated using PCB with the parameters listed in Table I. Also, two conventional unidirectional design have been fabricated with the same enclosed area of the proposed design and the receivers are identical for both conventional and proposed design for fair comparison. Due to this work focuses on achieving the stable transferred power level with high PTE by maintaining the smooth mutual inductance values regards the transfer position variation, the port terminations are selected to be 50 Ω for simplicity. Herein, the vector network analyser (VNA) and 50 Ω cables can be applied with perfect matching conditions. The S_{21} performance will be evaluated by the two-port 50 Ω VNA. A photo of the measurement set-up is shown Fig. 6-20.

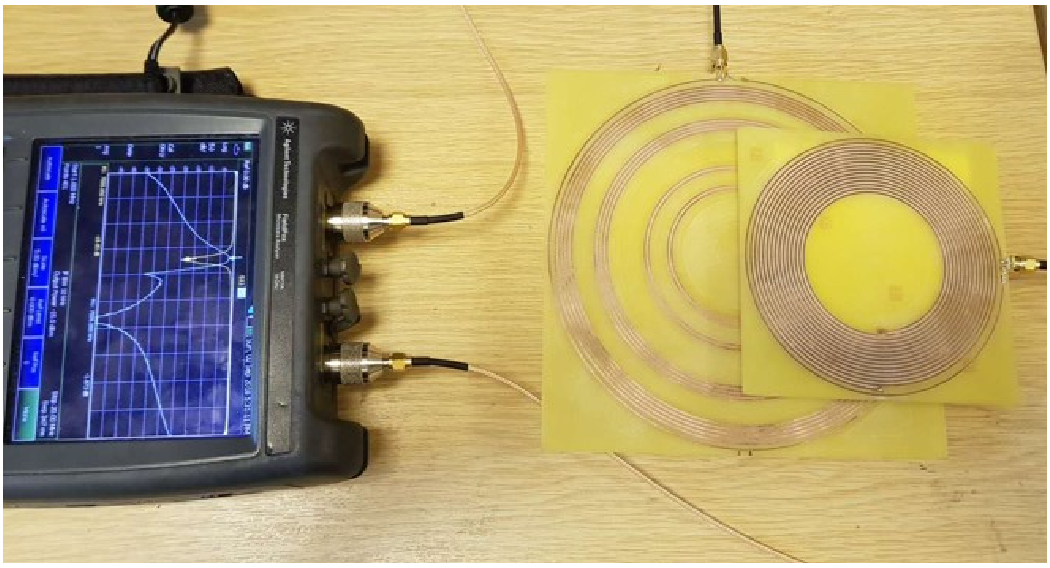

Fig. 6-20. A photo of the measurement setup.

To investigate if the proposed structure has the high-efficiency performance regards the transfer position, the fabricated prototype has been measured against the transfer height and horizontal misalignment respectively. As discussed in Section II, conventional design will have frequency splitting phenomena when the Tx and Rx are placed too close to each other, therefore, the frequency response of the proposed structure has been measured with the transfer height varying from 10 mm to 130 mm with the comparison of the conventional design as shown in Fig. 6-21.

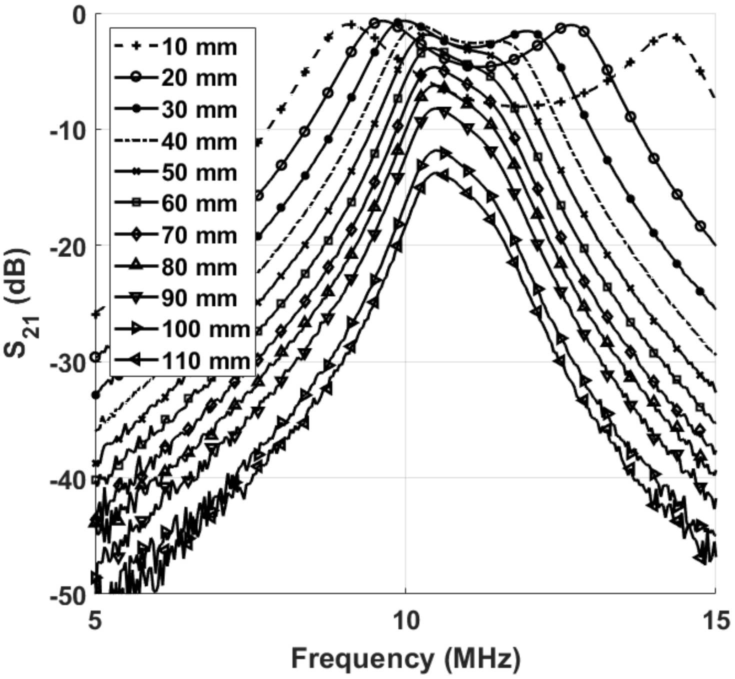

(a)

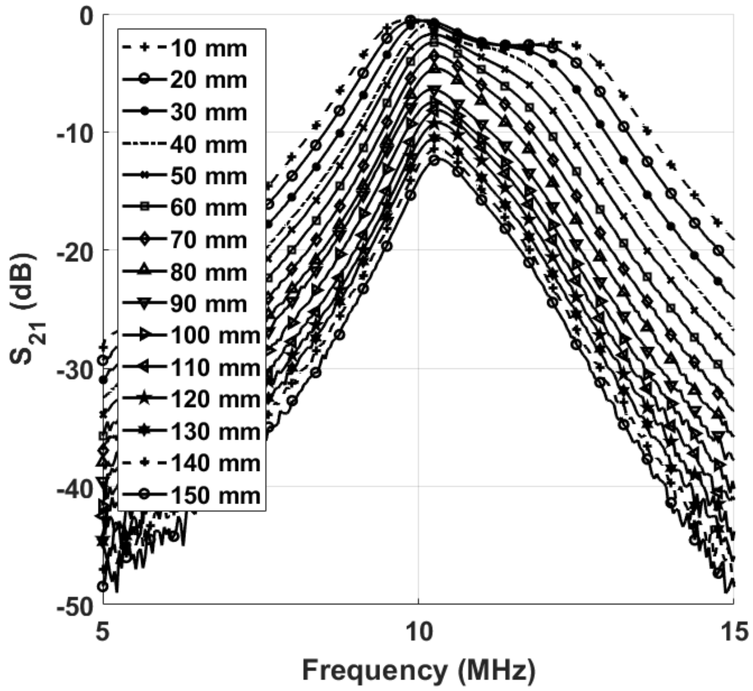

(b)

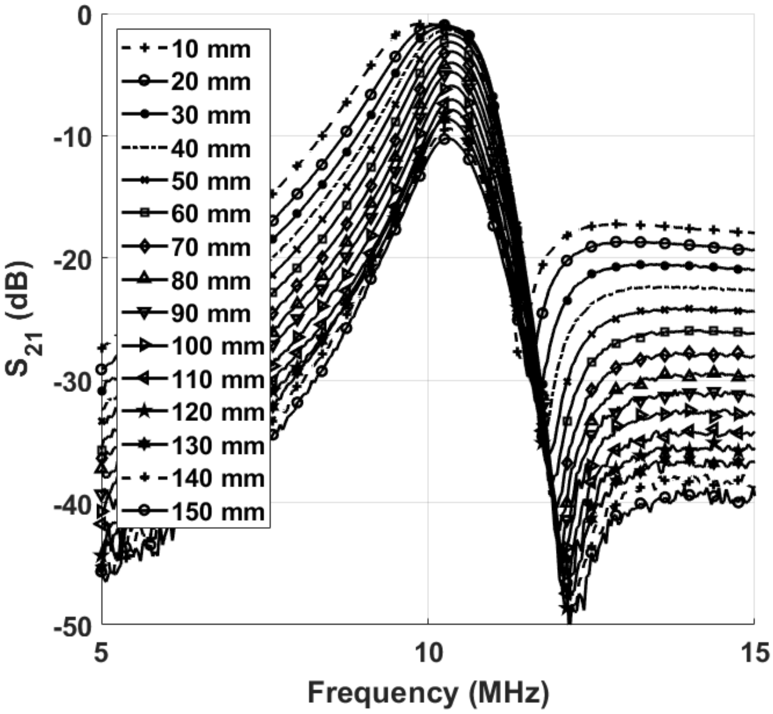

(c)

Fig. 6-21. Measured S21 against the variation of transfer distance h of (a) Type-I, (b) Type-II, (c) the proposed system.

When the transfer height changes from 10 mm to 50 mm, the PTE at the desired resonant frequency of the conventional design suffers from the frequency splitting due to the excessive coupling. A minor frequency splitting also occurred when the proposed Tx was placed 10 mm from the Rx, and when the transfer height is increasing, the desired frequency can be maintained with relatively high efficiency. The measured and simulated efficiency performances at the desired resonate frequency against the transfer height comparison of the proposed and conventional design have been plotted in Fig. 6-22.

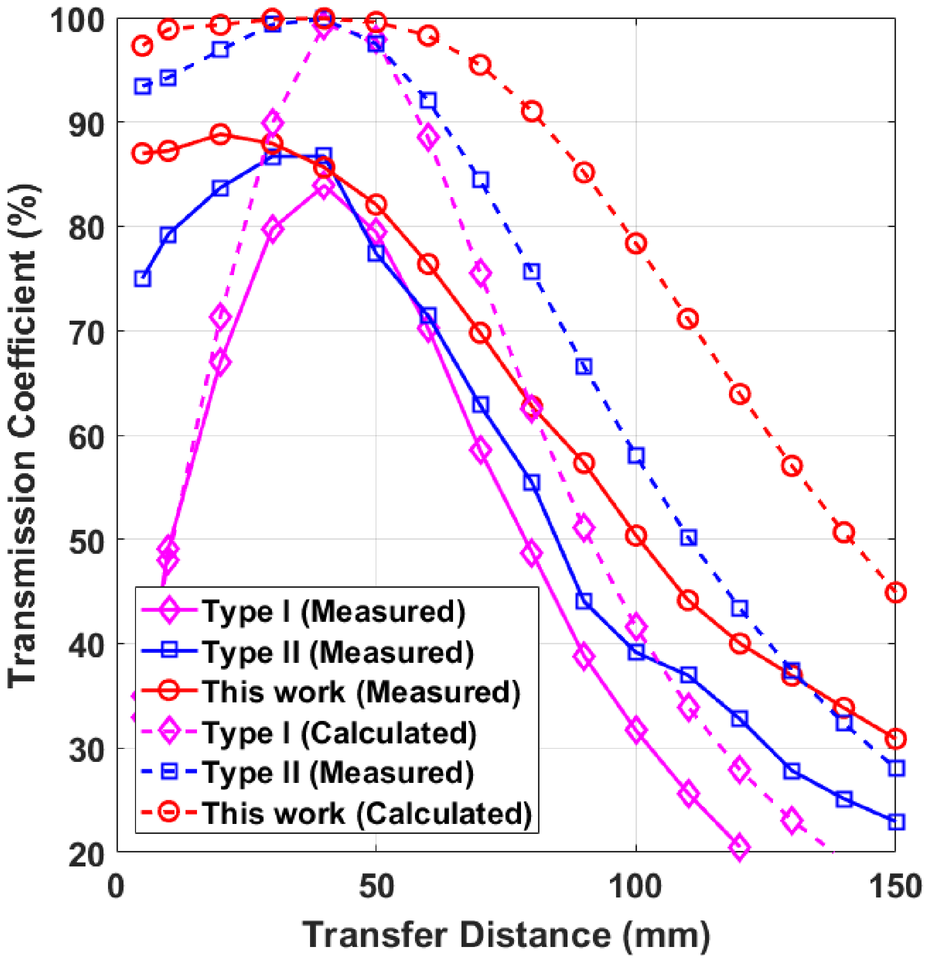

(a)

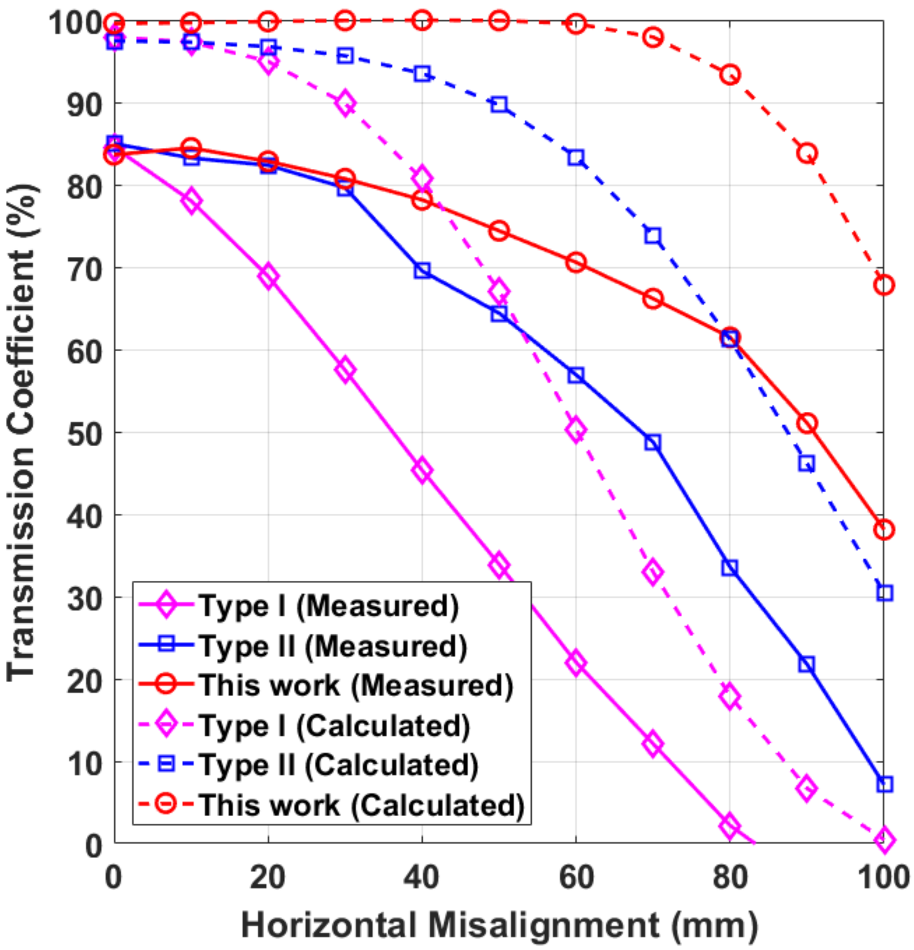

(b)

Fig. 6-22. Comparison of the measured PTE of the proposed system with conventional designs against (a) transfer distance (*d* = 0 mm), (b) horizontal misalignment (*h* = 40 mm).

The measured results for both conventional and proposed design follow the slope trend of the simulations with lower magnitude caused by the ohmic and radiation losses which were ignored in simulations. The maximum efficiency of the conventional design was only obtained at h = 50 mm and degraded very fast when the height deviated from the optimum. Although the efficiency of conventional design is higher than the proposed design at 40 mm to 50 mm by less than 10%, the proposed design has significant improved efficiency at the close range from 10 mm to 40 mm. Also, the efficiency of the proposed design has a slower degradation slope when the transfer height is larger than 70 mm which agrees with the numerical simulation results. The efficiency of the proposed design has been kept better than 70% with transfer height varied from 10 mm to 70 mm. On the other hand, the measured results show that the proposed design has achieved an efficiency better than 38% with transfer height change from

10 mm to 140 mm. This has validated the robustness of the proposed design against transfer height.

The anti-misalignment feature has been measured and the frequency response of the proposed structure has been measured with the misalignment varying from 0 mm to 100 mm with different transfer height as shown in Fig. 6-23.

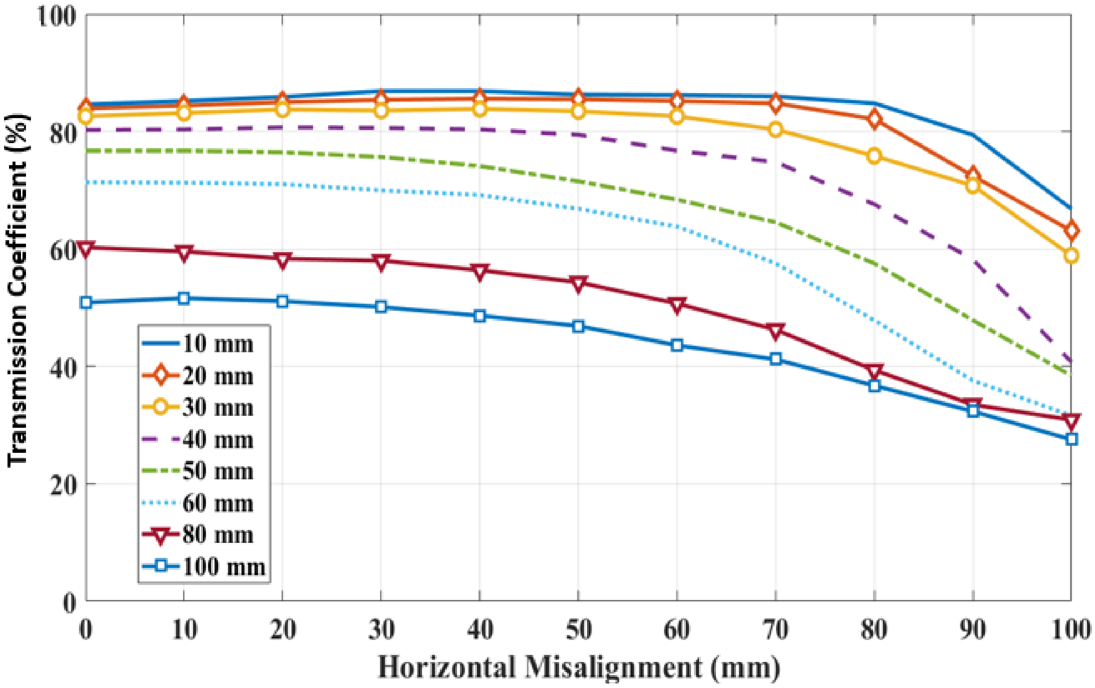

Fig. 6-23. Measured efficiency performance against the horizontal misalignment with different transfer height.

When the transfer height is lower than 40 mm, the efficiency can be maintained above 70% with the misalignment vary from 0 mm to 70 mm. Although, the anti-misalignment ability will decrease with the transfer height increase, the efficiency has been kept better than 30% with both transfer height and misalignment are 100 mm. The measured anti-misalignment performance at $h = 50$ mm of the proposed and conventional are compared with the simulations as shown in Fig.6-24. Although, the conventional design has a better efficiency when the misalignment is small, its efficiency drops much faster than the proposed design.

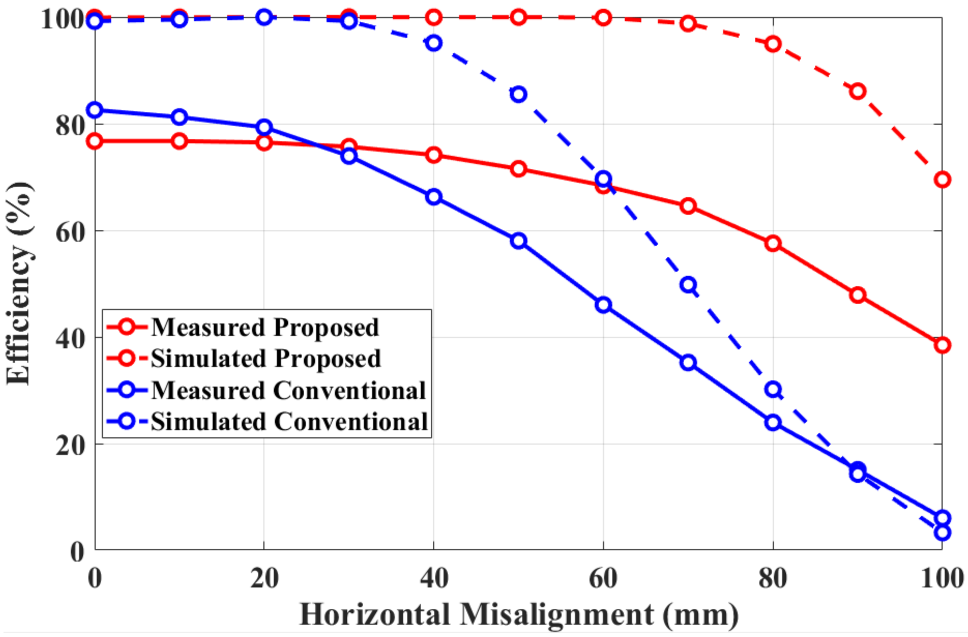

Fig. 6-24. Measured efficiency performance against the horizontal misalignment with different transfer height.

Finally, the measured PTE performances with the transfer position variation for both conventional and proposed design are shown in Fig. 6-25. The efficiency can be kept better than 70% with transfer height from 10 mm to 50 mm and misalignment from 0 mm to 50 mm. The results show that the proposed design is capable of maintaining a relatively high efficiency with the existence of the transfer height and misalignment simultaneously. The measured results show a good agreement with the theoretical analysis and numerical simulations, which validated the proposed structure and design method.

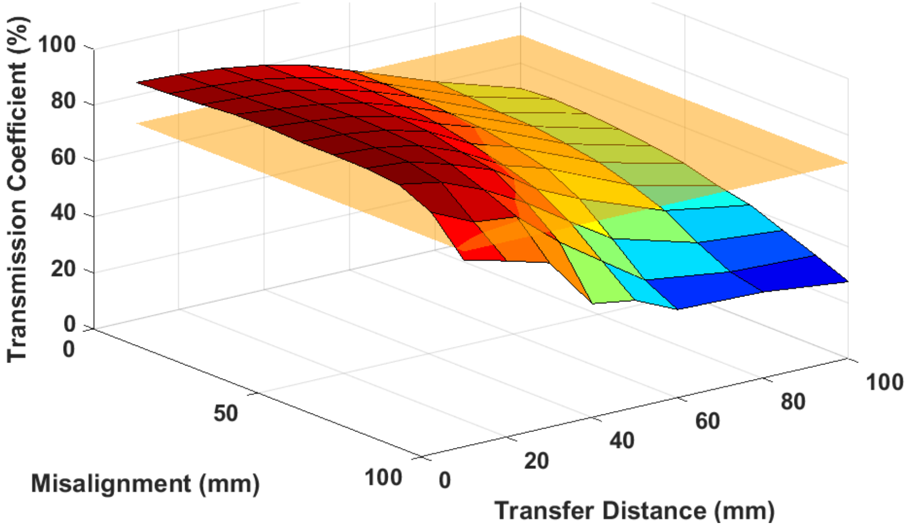

Fig. 6-25. Measured efficiency performance with the transfer position variation with a reference efficiency of 70%.

6.6 Summary

WPT systems using coupled magnetic resonances are susceptible to the transfer position due to that the coupling condition between the transmitting and receiving coils is highly position-dependent. Once the transfer position deviates from the optimum one, the coupling will be either excessive or weak which results in a transfer efficiency degradation. Here we present a transmitter structure consisting of multiple sub-coils oriented in opposite directions to keep the coupling relatively constant over an extensive range of transfer position. We were able to achieve a transfer efficiency of 70% - 88% with transfer distance varying from 5 mm to 70 mm and an efficiency of 60% - 85% with the displacement changing from 0 mm – 80 mm at a 40 mm transfer distance. The diameters of the transmitter and receiver are 84.6 mm and 45.1 mm respectively. The measured efficiency of the proposed design can be kept better than 70% with a transfer distance varying from 5 mm to 50 mm while the misalignment from 0 mm to 50 mm. The performance of the system regarding transfer efficiency much less sensitive to the transfer position shows a great potential in wireless charging applications.

6.7 References

[1] N. Tesla, “Apparatus for transmitting electrical energy,” U.S. Patent 1119732, Dec. 1, 1914.

[2] L. P. Wheeler, “Tesla’s contribution to high frequency,” *Elect. Eng*., vol. 62, pp. 355–357, Aug. 1943.

[3] [Online] Available: http://www.tfcbooks.com/articles/witricity.html

[4] S. Y. R. Hui, W. Zhong and C. K. Lee, “A critical review of recent progress in mid-range wireless power transfer,” *IEEE Trans. Power Electronics*., vol. 29, no. 9, pp. 4500–4511, Sep. 2014.

[5] J. C. Schuder, H. E. Stephenson, and J. F. Townsend, “High level electromagnetic energy transfer through a closed chest-wall,” *IRE Int. Conv. Rec*., vol. 9, pp. 119–126, 1961.

[6] W. H. Ko, S. P. Liang, and C. D. F. Fung, “Design of rf-powered coils for implant instruments,” *Med. Biol. Eng. Comput*., vol. 15, pp. 634–640, 1977.

[7] E. Hochmair, “System optimization for improved acuracy in transcutaneous signal and power transmission,” *IEEE Trans. Biomed. Eng*., vol. BME-31, no. 2, pp. 177–186, Feb. 1984.

[8] B. Choi, J. Nho, H. Cha, T. Ahn, and S. Choi, “Design and implementation of low-profile contactless battery charger using planar printed circuit board windings as energy transfer device,” *IEEE Trans. Ind. Electron*., vol. 51, no. 1, pp. 140–147, Feb. 2004.

[9] Y. Jang and M. M. Jovanovic, “A contactless electrical energy transmission system for portable-telephone battery chargers,” *IEEE Trans. Ind. Electron.*, vol. 50, no. 3, pp. 520–527, Jun. 2003.

[10] W. G. Hurley and J. Kassakian, “Induction heating of circular ferromagnetic plates,” *IEEE Trans. Magnetics*., vol. 15, no. 4, pp. 1174–1181, Jul. 1979.

[11] A. W. Green and J. T. Boys, “10 kHz inductively coupled power transferconcept and control,” *in Proc. ICPE-VSD*, 1994, pp. 694–699.

[12] J. T. Boys, G. A. Covic, and A. W. Green, “Stability and control of inductively coupled power transfer systems,” *Proc. Electric Power Appl.*, vol. 147, no. 1, pp. 37–43, 2000.

[13] J. T. Boys, A. P. Hu, and G. A. Covic, “Critical Q analysis of a current-fed resonant converter for ICPT applications,” *Electron. Letters*., vol. 36, no. 17, pp. 1440–1442, 2000.

[14] G. A. J. Elliott, G. A. Covic, D. Kacprzak, and J. T. Boys, “A new concept: Asymmetrical pick-ups for inductively coupled power transfer monorail systems,” *IEEE Trans. Magnetics*., vol. 42, no. 10, pp. 3389–3391, 2006.

[15] M. L. G. Kissin, J. T. Boys, and G. A. Covic, “Interphase mutual inductance in polyphase systems,” *IEEE Trans. Ind. Electronics*., vol. 56, no. 7, pp. 2393–2400, 2009.

[16] B. Choi, J. Nho, H. Cha, T. Ahn, and S. Choi, “Design and implementation of low-profile contactless battery charger using planar printed circuit board windings as energy transfer device,” *IEEE Trans. Ind. Electron*., vol. 51, no. 1, pp. 140–147, Feb. 2004.

[17] Y. Jang and M. M. Jovanovic, “A contactless electrical energy transmission system for portable-telephone battery chargers,” *IEEE Trans. Ind. Electron.,* vol. 50, no. 3, pp. 520–527, Jun. 2003.

[18] C.-G. Kim, D.-H. Seo, J.-S. You, J.-H. Park, and B. H. Cho, “Design of a contactless battery charger for cellular phone,” *IEEE Trans. Ind. Electron.,* vol. 48, no. 6, pp. 1238–1247, Dec. 2001.

[19] A. P. Sample, D. T. Meyer, and J. R. Smith, “Analysis, experimental results, and range adaptation of magnetically coupled resonators for wireless power transfer,” *IEEE Trans. Ind. Electron*., vol. 58, no. 2, pp. 544–554, Feb. 2011.

[20] A. Kurs *et al*., “Wireless power transfer via strongly coupled magnetic resonances,” *Science*, vol. 317, no. 5834, pp. 83–86, Jul. 2007.

[21] J. Kim and J. Jeong, “Range-adaptive wireless power transfer using multiloop and tunable matching techniques,” *IEEE Trans. Ind. Electron.,* vol. 62, no. 10, pp. 6233–6241, Oct. 2015.

[22] J. Kim, W. Choi, and J. Jeong, “Loop switching technique for wireless power transfer using magnetic resonance coupling,” *Progr. Electromagn. Res*., vol. 138, pp. 197–209, 2013.

[23] S. Raju, R. Wu, M. Chan, and C. P. Yue, “Modelling of mutual coupling between planar inductors in wireless power applications,” *IEEE Trans. Power Electron*., vol. 29, no. 1, pp. 481–490, Jan. 2014.

[24] L. Chen, S. Liu, Y. Zhou, and T. Cui, “An optimizable circuit structure for high-efficiency wireless power transfer,” *IEEE Trans. Ind. Electron*., vol. 60, no. 1, pp. 339–349, Jan. 2013.

[25] Y. Zhang, T. Lu, Z. Zhao, K. Chen, F. He and L. Yuan, "Wireless power transfer to multiple loads over various distance using relay resonators". *IEEE Trans. Microwave and Components Letters*. Vol, 25, no. 5, pp. 337–339, May. 2015.

[26] Dong-Wook. Seo and Jae-Ho Lee, "Frequency-tuning method using the reflection coefficient in a wireless power transfer system". *IEEE Trans. Microwave and Components Letters*. Vol, 27, no. 11, pp. 959–961, Nov. 2017.

[27] W. M. Ng, C. Zhang, D. Lin and S. Y. Hui, “Two- and three-dimensional omnidirectional wireless power transfer,” *IEEE Trans. Power Electron*., vol. 29, no. 9, pp. 4470–4474, Sep. 2014.

[28] Bo-Hee. Choi, B. C. Park and Jeong-Hae Lee, "Near-field beamforming loop array for selective wireless power transfer". *IEEE Trans. Microwave and Components Letters*. Vol, 25, no. 11, pp.748–750, Nov. 2015.

[29] Y. L Lyn, F. Y. Meng, G. Yang, B. Che, Q. Wu, L. Sun, D. Erni and Joshua Le-Wei Li, “A method of using nonidentical resonant coils for frequency splitting elimination in wireless power transfer,” *IEEE Trans. Power Electron*., vol. 30, no. 11, pp. 6097–6107, Nov. 2015.

[30] W. S. Lee, W. I. Son, K. S. Oh, and J. W. Yu, “Contactless energy transfer systems using antiparallel resonant loops,” *IEEE Trans. Ind. Electron*., vol. 60, no. 1, pp. 350–359, Jan. 2013.

[31] Kurs. A. et al. Wireless power transfer via strongly coupled magnetic resonances. Science 317, 83-86, 2007.

[32] A. P. Sample, D. T. Meyer, and J. R. Smith, “Analysis, experimental results, and range adaptation of magnetically coupled resonators for wireless power transfer,” IEEE Trans. Ind. Electron., vol. 58, no. 2, pp. 544–554, Feb. 2011.

[33] S. Jeong, D. H. Kim and et al , “Smartwatch strap wirless power trasnfer system with flexible PCB coil and shielding material,” IEEE Trans. Ind. Electron, Early Access, DOI 10.1109/TIE.2018.2860534, Aug. 2018.

[34] W. Q. Niu, J. X. Chu, W. Gu and A. D. Shen, “Exact analysis of frequency splitting pehonmena of contantless power transfer systems,” IEEE Transactions on Circuit and *System I: Regular Papers*, vol. 60, DOI 10.1109/TCSI.2012.2221172, no. 6, pp. 1670-1677, Jun. 2013.

[35] Y. Zhang and Z. Zhao, “Frequency splitting analysis of two-coils resonant wireless power transfer,” IEEE Antennas and Wireless Propagation Letters, vol. 13, DOI 10.1109/LAWP.2014.2307924, pp. 400-402, Feb. 2014.

[36] L. Li, H. Liu, H. Zhang and W. Xue, “Efficient wireless power transfer system integrating with metasurface for biological applications,” IEEE Trans. Ind. Electron., vol. 65, no. 4, pp. 3230–3239, Apr. 2018.

[37] Lipworth, G. et al. Magnetic Metamaterial superlens for increased range wireless power transfer. Scientific Reports. 4, 3642, 2014.

[38] Agrawal, D. R. et al. Conformal phased surfaces for wireless powering of bioelectronic microdevices. Nature Biomedical Engineering. 1, 0043, 2017.

[39] Abiri, P. et al. Inductively powered wireless pacing via a miniature pacemaker and remote stimulation control system. Scientific Reports. 7, 6180, 2017.

[40] Montgomery, K. L. et al. Wirelessly powered, fully internal optogenetics for brain, spinal and peripheral circuits in mice. Nature Methods. 12, 969-974, 2015.

[41] Mei, H. & Irazoqui, P. P. Miniaturizing wireless implants. Nature Biotechnology. 32, 1008-1010, 2014.

[42] Yamagishi, K. et al. Tissue-adhesive wirelessly powered optoelectronic device for metronomic photodynamic cancer therapy. Nature Biomedical Engineering. 2018.

[43] K. Aditya and S. S. Williamson, "Design guidelines to avoid bifurcation in a series-series compensated inductive power transfer system," IEEE Trans. Ind. Electron, Early Access, DOI 10.1109/TIE.2018.2851953, Jul. 2018.

[44] J. Liu, K. W. Chan, C. Y. Chung, N. H. L. Chan, M. Liu and W. Xu, "Single-stage wireless-power-trasnfer resonat converter with boost bridgeless power-factor-correction rectifier," *IEEE Trans. Ind. Electron.*, vol. 65, DOI 10.1109/TIE.2017.2745471 no. 3, pp. 2145–2155, Apr. 2018.

[45] C. Jiang, K. T.Chau, Y. Leung, C. H. T. Lee and W. Han, "Design and analysis of wireless ballastless fluorescent lighting," IEEE Trans. Ind. Electron, Early Access, DOI 10.1109/TIE.2017.2784345, Dec. 2017.

[46] Y. Zhang and Z. Zhao, "Frequency splitting analysis of four-coils resonant wireless power transfer," IEEE Transactions on Industry Applications, vol. 50, DOI 10.1109/TIA.2013.2295007, no. 4, pp. 2436-2445, Dec. 2013.

[47] H. Nguyen and J. Agbinya, "Splitting frequency diversity in wireless power transmission," IEEE Transactions on Power Electronics, vol. 30, DOI 10.1109/TPEL.2015.2424312, no. 11, pp. 6088-6096, Apr. 2015.

[48] R. Huang, B. Zhang, D. Qiu and Y. Zhang, "Frequency splitting phenomena of magnetic resonant coupling wireless power transfer," IEEE Transactions on Magnetics, vol. 50, DOI 10.1109/TMAG.2014.2331143, no. 11, Dec. 2014.

[49] W. Fu, B. Zhang, and D. Qiu, "Study on frequency-tracking wireless power transfer system by resonant coupling," in Proc. IEEE IPEMC, May 2009, pp. 2658–2663.

[50] Abid, A. et al. Wireless power transfer to millimeter-sized gastronitestinal electronics validated in a swine model. Scientific Reports. 7, 46746, 2017.

[51] T. C. Beh, T. Imura, M. Kato, and Y. Hori, "Basic study of improving efficiency of wireless power transfer via magnetic resonance coupling based on impedance matching," in Proc. IEEE ISIE, Jul. 2010, pp. 2011–2016.

[52] J. Kim and J. Jeong, "Range-adaptive wireless power transfer using multiloop and tunable matching techniques," IEEE Trans. Ind. Electron., vol. 62, no. 10, pp. 6233–6241, Oct. 2015.

[53] W. S. Lee, W. I. Son, K. S. Oh, and J. W. Yu, “Contactless energy transfer systems using antiparallel resonant loops,” IEEE Trans. Ind. Electron., vol. 60, no. 1, pp. 350–359, Jan. 2013.

[54] X. M. Chen, X. Wang and X. F. Chen, “Energy-efficient optimization for wireless information and power transfer in large-scale MIMO systems employing energy beamforming,” IEEE Wireless Communications Letters, vol. 2, DOI 10.1109/WCL.2013.092813.130514, pp. 667-670, Oct. 2013.

[55] Assawaworrarit, S., Yu, X. F. & F, S. H. Robust wireless power transfer using a nonlinear parity-time-symmetric circuit. Nature. 546, 387, 2017.

[56] X. Li, C. Y. Tsui and W. H. Ki, “A 13.56 MHz wireless power transfer system with reconfigurable resonant regulating rectifier and wireless power transfer control for implantable medical devices,” IEEE Journal of Solid-state Circuits, vol. 50, DOI 10.1109/JSSC.2014.2387832, no. 4, pp. 978-989, Feb. 2015.

[57] Z. Dang, Y. Cao and J. A. Abu Qahouq, “Reconfigurable magnetic resonace-coupled wireless power transfer system,” IEEE Transactions on Power Electronics, vol. 30, DOI 10.1109/TPEL.2015.2422776, no. 11, pp. 6057-6069, Nov. 2015.

[58] Akyel, C., Babic, S. I. & Mahomudi, M. M. Mutual inductance calculation for non-coxial circular air coils with parallel axes. Progress In Electromagnetic Research. 91,287–301,2009.

Chapter 7 **Conclusions and Future Work**

7.1 Summary

In this thesis, the techniques of efficient power transfer in wireless communication systems have been introduced in detail. The impedance matching techniques for devices with variable impedances have been studied, analysed and applied into three diffident device designs. The power transfer devices studied in this thesis are laid in three different field, from signal amplification stage, signal transmission stage and energy harvesting part. The fabricated devices including broadband efficient power amplifiers (PA), a range-adaptive wireless power transfer (WPT) system and a magnetic energy harvesting (EH) circuit have demonstrated the state-of-the-art performance, proving the validity of the proposed matching techniques. An Radio Frequency (RF) PA that can operate in a multi-octave bandwidth with high output power, stable power gain and high efficiency has been designed and introduced. This design improved the power transfer efficiency in power amplification stage of the wireless communication system. The input and output matching networks of the PA are be able to maintain vert good matching condition passively regardless the impedance variation caused by nonlinear effects of the transistor, in terms of frequency sweeping, output power level change, to keep the PA operating with a high-efficiency feature. A range-adaptive magnetic resonant coupling wireless power transfer system (MRC-WPT) that can transfer the desired power level with desired high efficiency in a large adaptive position range has been introduced. The transmitter and receiver of the system are be able to provide a relatively smooth mutual inductance passively regardless of the transfer position in terms of transfer height and horizontal misalignment. This design has improved the power transfer efficiency of the signal transmission in the wireless communication system. A magnetic energy harvester for AC power transmission lines which can deliver high power with the existence of the magnetic core saturation has been investigated to harvest the available energy in ambient environment. The matching network of the energy harvester is be able to manipulate the dominant magnetic field of an AC power line to an optimal level to mitigate the magnetic core saturation phenomenon, achieving a high output power. The presented designs have validated the proposed matching techniques can be categorised by adaptively matching the variable impedance and constrain the impedance variation.

In Chapter 2, an in-depth literature review has been presented introducing the variable impedance matching challenges in the broadband efficient PAs design. The pros and cons of the conventional impedance matching methods have been introduced, analysed and compared. The knowledge and previous work summited in this chapter will help readers to understand the state-of-the-art in variable impedance matching techniques. It should be valuable for researchers who are presently working on this topic and who are going to investigate this area in the future.

Chapter 3 presents the design, implementation and experimental results of a broadband high-efficiency GaN-HEMT PA with constrained optimal impedance contours. Due to that the optimal impedance for both input and output of a transistor varies with frequency, the impedance variation is constrained by establishing optimal impedance contours covering the required optimal impedance across the desired bandwidth. Source-pull and load-pull simulations were employed to determine the optimum input and output impedances to achieve high power added efficiency (PAE). A low-pass network based on a closed-form solution was applied to realize the optimal impedance. Then it was transferred to a band-pass network using Norton Transformation without sacrificing of bandwidth or matching quality. Finally, the PA has demonstrated an out-standing performance in terms PAE and shown a great potential in GNSS applications.

Chapter 4 presents a novel general design method of frequency varying impedance matching. Due to the optimal impedance required for a multi-octave PA vary in a large range, the variation constrain method cannot be applied. Therefore, the method introduced in this chapter will be focusing on adaptively matching the variable optimal impedance required by the PA over a wide bandwidth. The proposed method defines the optimal impedance regions of a PA at several frequency sections over the operational frequency band. These regions contain the impedances that can achieve a high output power and a high PAE simultaneously. A low-pass LC-ladder circuit is selected as the matching network (MN). The element values of the MN can be obtained using a synthesising method based on stochastic reduced order models and Voronoi partition. The MN provides a desired impedance in the predefined optimal impedance region at each frequency section. Thus, an optimal output power and PAE of the PA can be achieved. To validate the proposed method, two eighth-order low-pass LC-ladder networks are designed as the input and output matching network, respectively. The performance of the PA outperforms existing broadband high-efficiency PAs in many aspects which demonstrates the excellence of the proposed method.

Chapter 5 chapter presents a novel design method for EH from AC power lines by using a current transformer-based energy harvester under its magnetic saturation condition. The extracted power level of a conventional magnetic field energy harvester is limited by the maximum flux density of the magnetic core. When the magnetic core is clamped on AC power lines, the flux density of the core is proportional to the magnitude of the magnetic field strength around the power line. The flux density could reach its maximum value when the magnetic field increases. In this scenario, very little energy can be harvested since there are few flux density variations. Here we introduce a novel artificial magnetic field to manipulate the dominant magnetic field of power lines. The core will not be easily driven into the saturation region. Hence more energy can be harvested. An additional control coil is added to the harvester. As a result, the magnetic flux density in the core will not be saturated easliy. More energy can then be harvested. This design could be a promising solution for powering the smart grid monitoring and other industrial sensing applications.

Chapter 6 presents a range-adaptive WPT system with high efficiency using a two-coil structure with multiple bi-directional loops. This work focusses on constraining the impedance variation caused by mutual inductance fluctuation concerning the changing of the transfer position. Conventional magnetic resonance coupling WPT systems are very sensitive to the transfer position due to that the mutual inductance is highly position-dependent. Most designs rely on the optimal position between the transmitter and receiver to achieve the desired coupling condition. Once the transfer position deviates from the optimum one, the coupling will be either excessive or weak resulting in a transfer-power or efficiency degradation. The proposed structure adopts a transmitter consisting of multiple loops oriented in opposite directions to keep the coupling relatively constant over a large range of transfer position. Consequently, the transfer efficiency of the proposed system is much less sensitive to the transfer position which demonstrates a great potential in mobile devices charging applications.

7.2 Key Contributions

This work has provided a thorough study on variable impedance matching techniques in wireless communication systems. The most challenging research problems have been identified and analysed. Several cutting-edge techniques to solve the problems have been presented and validated by experiments. Some results of this thesis have been peer reviewed by many top scientists and researchers.

The key contributions to new knowledge are detailed as follows:

1. Chapters 1&2: Introduction and Literature Review

A comprehensive literature review has been presented to illustrate the recent development of variable impedance matching techniques for wireless communication systems. A clear evolution of the matching techniques for different device design has been presented.

2. Chapter 3: Broadband Efficient PA with constrained optimal impedance contours

The idea of optimal impedance contour is proposed to limit the variation of the impedance of PAs. The detailed design methodology, implementation procedure and measurement results of a broadband high-efficiency PA are presented. Source-pull and load-pull simulation were applied to find the optimal input and output impedance of the transistor. A low-pass network was designed first to match the optimum impedances and it was transferred to a band-pass network. Then a PI-type Norton transformation was applied to scale the load of the band-pass network to the 50 Ω. The designed PA achieved a PAE from 60%-86% across 0.9-1.5 GHz with a relatively flat gain around 11 dB and an output power of 10 to 22 W. The measured performance shows that the PA is a good candidate for satellite communications and GNSS applications.

3. Chapter 4: Adaptive Impedance Matching of Multi-Octave Efficient PA

This chapter reports state-of-the-art performance in terms of bandwidth and efficiency of PAs. The main contribution is the optimization procedure of the MNs over a multi-octave bandwidth by proper application of a statistical approach presented in 2009 by Grigoriu for reduced order modelling problems, as referred by the authors. This technique only needs to examine a reduced number of samples, and no initial guess or data training are required. The commercially available software provides useful tools for broadband matching, but the approach used in this work has shown to work well with complex problems involving multidimensional optimisation space and strict optimisation goals such as it is the case of the reported multi-octave high-efficiency PA. The experimental results have shown a PAE of 60-82%, a gain of 12-15 dB and an output power between 42-45 dBm (16-32 W) over a 160% fractional bandwidth from 0.2 GHz to 1.8 GHz. The performance is better than any previously reported work. The results have demonstrated the potential of the proposed method to design high-performance PAs for future communication systems.

4. Chapter 5: Harvested Energy Improvement by Magnetic Field Manipulation

In this chapter, a novel magnetic field EH method is presented which can significantly increase the level of energy harvested from AC power lines. The impedance variation in the time-domain caused by the magnetic core saturation is significantly reduced by the applied artificial magnetic field manipulation technique. To capture the magnetic field around the power line, a nano-crystalline core with a high permeability has been used. Due to the high current in the power line, the core is easily driven into saturation region. Very little power can be harvested when the core is saturated. To keep the core in the non-saturation region, a control coil has been added to the harvester. The control coil can generate a magnetic field H_C to mitigate the magnetic saturation of the core artificially. The numerical simulation shows excellent agreement with the measured results. The proposed energy harvester has achieved an average output power of 283 mW on a power line with a current of 10A rms, which indicates a 45% increment compared to a harvester without using the proposed method. The proposed harvesting method have shown excellent potential for industrial applications such as driving the power line monitoring sensors and weather stations.

5. Chapter 6: Range-Adaptive Structure for WPT system

A circular multiple bi-directional loop WPT system has been presented in this chapter. The proposed structure has been analysed in detail, and the design formulas have been derived accordingly. To validate the novel design structure and method, a prototype of the proposed structure has been fabricated and measured. With the proposed structure, the over-coupling region has been weakened by using bi-directional loops. The mutual inductance between the transmitter and receiver has been kept very uniform within the desired transfer distance. On the other hand, the proposed structure also provides a smoothed mutual inductance against the horizontal misalignment. The range-adaptive WPT characteristic is achieved by the proposed structure. Based on experimental results, the proposed system achieves a transfer efficiency of 70% - 88% with transfer distance varying from 0 mm to 70 mm and an efficiency of 60% - 85% with the displacement changing from 0 mm – 80 mm at a 40 mm transfer distance. The diameters of the transmitter and receiver are 84.6 mm and 45.1 mm respectively. The measured efficiency of the proposed design can be kept better than 70% with a transfer distance varying from 0 mm to 50 mm while the misalignment from 0 mm to 50 mm. The performance of the system regarding transfer efficiency much less sensitive to the transfer position shows great potential in wireless charging applications.

7.3 Future Work

Based on the conclusions above and considering the limitations of the work existed, future research could be carried out in the following areas.

- **In-band Mode Transfer PA**

  It has been shown in Fig. 4-11 of Chapter 4 that the voltage and current waveforms for different frequencies are not identical. As analysed in Chapter 2, the variation of the waveforms indicate that the PA is operating in different modes when the operating frequency varying. However, given that the operation mode of a PA will be only controlled by the bias voltage condition as discussed in Chapter 2. In this case, the PA operation mode variation with the operating frequency is worthy to be investigated for efficient wideband PA design. One possible design based on in-band mode transfer is using Class-F and inverse Class-F together, where PA can operate in Class-F mode for first half of the operational band and inverse Class-F mode for the second half band.

- **Broadband Efficient PA based RF Rectifier**

  Rectifiers are important devices in WPT and microwave energy harvesting. Conventionally, rectifiers are realized by diodes at microwave frequencies, GaN HEMTs provide advantages of broadband harvesting and high-power rectification. For certain load conditions, a GaN HEMT can achieve similar efficiencies as both a power amplifier and a rectifier due to its time-reversal duality property. Assume a PA operating in some high-efficiency mode such as Class-E or Class-F that has an RF output power P_{OUT} at a supply voltage of V_D and appropriate gate drive and bias. If now the drain supply is disconnected and an RF power $P_{IN} = P_{OUT}$ input into the RF drain port, the PA will behave as a rectifier with a conversion efficiency equal to the power-added efficiency of the PA, η=PAE. Furthermore, the output DC voltage $V_{DC}=V_D$ across some optimal DC load RD, assuming the gate bias and input drive conditions are kept the same. With a highly reflective termination, Z_{gate}, the coupled power can be reflected into the gate to turn on the transistor without a second RF source. Therefore, based on the broadband matching technique introduced in Chapter 4, the PA structure can be reformed to a broadband efficient RF rectifier which is able to recover the RF signal propagated in the ambient environment to usable DC power.

- **Current independent EH system**

The magnitude of the magnetic field strength near the high-power equipment will change with the real-time demand from the grid. However, the winding of the transformer and load resistance of the harvester are designed based on the primary current magnitude. Once the primary current varies from the optimal value, the harvested power density will decrease dramatically. Therefore, the magnetic EH system should be further optimised to capture the magnetic field with different current level of the power transmission system. One promising solution for future work is to add a current monitoring unit at the primary current power line to sense the primary current magnitude and then control the load resistance to maintain the maximum harvested power density for the system. This current independent EH system will have a great potential in practical power grid energy harvesting applications.

- **Hybrid Current Sensing and Energy Harvesting Circuit**

The magnetic energy harvesting system presented in Chapter 5 improved the harvested power density by using the compensating unit to prevent the magnetic core from being driven into saturation region. In this case, the harvested power will be proportional to the primary current magnitude where the harvested power density can be used to indicate the primary side current magnitude. This method will significantly improve the current sensing accuracy compared to conventional current measuring method especially for high amplitude current measurement. If the current sensing function can be added to the proposed energy harvesting circuit, the primary side current can be monitored in real-time, furtherly improving the magnetic field compensating unit to recover the unsaturation operation mode of the magnetic core.

- **Anti-Rotation and Range-Adaptive WPT System**

The bi-directional coils presented in Chapter 6, although, provide a range-adaptive WPT system with high power transfer efficiency, the transmitter and receiver are required to be placed in two parallel planes. However, in practical applications such as mobile devices charging, the end user devices will not be maintaining in a plane that is parallel to the transmitter where the high transfer efficiency cannot be achieved. In this case, the angle between the transmitter and receiver planes should be taken into consideration. For practical applications, the anti-rotation and range adaptive features are desired to achieved simultaneously. The proposed design method in Chapter 6 has shown the ability of high-efficiency range-adaptive power transfer. The main idea of this method is to keep the mutual inductance between transmitter and receiver to be smooth with the variation of the charging position. At the moment, the mutual inductance is only investigated with transfer distance and misalignment variations. For further research, the receiver rotation in vertical axis and horizontal axis should be examined.

END